Endogenous Huntingtin aggregates are a huge organized scaffold and mold for Golgi apparatus impaired by mutant Huntingtin protein

Lixiang Ma[1*#], Xinyu Chen[1*], Yang Liu[1*], Lijun Dai[2*], Weiqi Yang[1*], Hada Buhe[1], Jixin Ma[1], Chenyun Song[1], Li Li[3], Dandan Fan[2], Jianzhong Su[2#], Hexige Saiyin[4#]

1. Department of Anatomy, Histology & Embryology, School of Basic Medical Science, Fudan University, Shanghai 200032, People's Republic of China

2. Oujiang Laboratory (Zhejiang Lab for Regenerative Medicine, Vision and Brain Health), Wenzhou Medical University, Zhejiang 325001, China

3. Department of Anesthesiology, Huashan Hospital, Fudan University, Shanghai, China.

4. School of Life Sciences, Fudan University, Shanghai, 200438, People's Republic of China

[#]Correspondence to: School of Life Sciences, Fudan University, Shanghai, 200438, People's Republic of China

saiyin@fudan.edu.cn

Department of Anatomy, Histology & Embryology, School of Basic Medical Science, Fudan University, Shanghai 200032, People's Republic of China

lxma@fudan.edu.cn,

Oujiang Laboratory (Zhejiang Lab for Regenerative Medicine, Vision and Brain Health), Wenzhou Medical University, Zhejiang 325001, China

sujz@wmu.edu.cn

*, The authors equally contributed to this work.

Running title: Huntingtin aggregate is a Golgi scaffold

Key words: Huntington's disease, Endogeneous Huntingtin aggregate, Golgi, scaffold, ARF1

Abstract

Huntington's disease (HD), an incurable neurodegenerative disease, is caused by polyglutamine (polyQ) expansion in Huntingtin (HTT) protein. Despite HTTs naturally aggregating, huge variations of HTTs in visualizing methods make it unpredictable. Using 64 nm resolution scanning in the fibroblasts, induced neurons, organoids from an HD family, and human brain tissues, we revealed massive/long polyQ aggregates of HTTs formed by paralleled and interfused spindles that preferentially include flat Golgi stacks/ribbons/vesicles and disassembled in the mitotic and stressed cells with fragmented Golgi, brefeldin A (BFA) treatment and postfixation, and fragmented Golgi in the mitotic and stressed cells but not in BFA-treated cells binds to small HTTs. The disassembling of HTTs aggregates degraded HTTs. PolyQ aggregates with mutant HTT (mHTT)include a flat Golgi stack with a deformed surface, fragment easier in starvation, attach fewer Golgi/clathrin^{+} vesicles and ARF1 than polyQ assemblies without mHTT in fibroblasts or striatal/cortical neurons, and cause intranuclear inclusion bodies in striatal neurons. ScRNA data of striatal GABAergic neurons reveal impaired Golgi- or vesicle-related activities. Collectively, polyQ aggregates of HTTs are a stable form and highly organized scaffold and mold for flat Golgi stacks/ribbons/vesicles, and the existence of mHTT in polyQ assemblies reduced ARF-related activities and impaired Golgi in striatal/cortical neurons.

Introduction

Huntington's disease (HD) is a polyglutamine (polyQ) disease that causes severe striatal neuronal loss at an early stage, leading to devastating uncontrolled body movements[1-3]. HTT can easily form aggregates *in vivo* and *in vitro*[4-6]. HTT is highly expressed in nearly all human cells, whereas a limited number of cells in human brain paraffin tissues were detected by HTT antibodies[7,8]. HTT in fresh surgical brains was abundant, whereas time-dependent diminishing of HTT in preserved frozen or postmortem tissues was observed[9]. The inconsistency of cellular localization, morphometry, and levels across different tissues and cells suggest that the location and structure of HTTs might be prone to change after routine fixation[7,10-12]. The shortage of fresh human brain samples is a hurdle to understanding the nature of HTT aggregates, which are unstable in fixation and preservation. The emergence of iPSCs-induced neurons and brain organoids provides an alternative fresh source of brain samples to reveal the real nature of HTTs.

Aggregate formation and intranuclear inclusion bodies are the pathological hallmarks of HD[13,14]. However, aggregates of HTTs increase the survival of a single neuron[15], do not exert a toxic effect on cells, and even have a protective role in HD neurons[16,17]. Monomeric HTT forms soluble oligomers that precede the formation of fibrils and nuclear inclusions[18-20] and are toxic to cells[21-24]. HTT is a stiff protein composed of multiple α-helices and PolyQ[3,25-28]. All polyQ form a rigid fibril[28-31]. Fibrils with expanded polyQ were reported to poke the membrane of cellular organelles such as the endoplasmic reticulum (ER), and the poking of polyQ fibrils deforms ER membrane structure and alters the ER membrane dynamics[30]. TEM immunostaining images with HTTs antibodies revealed that HTTs distributed along Golgi cisternae[32] and formed organized and parallel fibrils[13]. In addition, multiple antibodies immunostaining, such as MV2, 3, 4, 5, 6, and 1F8, showed HTTs displayed Golgi-like patterns[33], suggesting HTTs might provide structural support for cellular activities.

Functionally, HTT involves almost all cellular activities, including vesicular transport, endocytosis, autophagy scaffolding, axonal trafficking, gene transcription, cell survival, polarity, and cilia function[3]. HTTs is an essential protein in embryonic development[34-36]. Reports indicate that embryos with truncation of the first exon are viable[37]. mHTT causes early transcriptional dysregulation[38], synaptic dysfunction[39], altered post-Golgi trafficking[40], aggregate pathology[13], mitochondrial dysfunction[41,42], and oxidative damage[3], and impairs the proteostasis network [43] and nuclear pore complex[44]. Pathophysiologically, mHTT induces extrasynaptic excitotoxicity[45], higher levels of brain inflammation[46,47], abnormal fetal brain development[12], and aging[48]. HAP40 stabilizes HTT[26,49]. HTT interacts with and activates dynamin, a protein that catalyzes membrane fission[50-52], microtubule motors, and actin-associated adaptors to support cellular vesicle transport, including autophagy, endosomes, and lysosomes[50,53]. The diversified roles of HTT in multiple organelles and the aggregate nature of HTT suggest that HTTs govern a central organelle in the cell.

Using novel HD family cells and 64 nm 3D resolution scanning, we revealed *a de novo* knitted fabric-like assemblies formed by polyQ of HTTs, which was previously described as aggregate, a fragile structure in postfixation and external stress, including flat Golgi stacks/cisternae and coupling mitotic and stress-related Golgi fragmentation. Pathogenic polyQ incorporation destabilizes polyQ assemblies and impairs Golgi activity. Our findings revealed a novel cytoplasmic scaffold/mold formed by polyQ of HTTs, *de novo* spatial relationships of Golgi architecture with HTTs assemblies, and a novel pathogenic phenotype of Golgi structure in HD patients.

Materials and methods

Ethics

The ethics of this HD work was approved (No. 28) by the Ethics Committee of the Institutes of Biomedical Sciences at Fudan University. All family members who attended this study signed a written consent translated into Mongolian. Dr. Li Li collected the human brain samples. The ethics approval number by Huashan Hospital Ethics Committee (KY2018-310.01).

Human fibroblast and blood sample collection

After getting consent, a surgeon collected the skin samples from the upper arm with a Skin Punch (diameter, 0.3x0.3cm). After collecting samples, a nurse and doctor visited the patients daily for 7 days to prevent inflammation. The tissues were harvested into a tube with culturing medium supplied with antibiotics. After being transported to a lab, tissues were moved to a Biosafety Cabinet, sliced into smaller fragments by surgical knives, and then attached to dishes by forceps and cultured in a dish with a small amount of medium. After completely attaching to dishes, the tissues were added to enough medium and continuously cultured for several weeks to get enough fibroblasts.

Immunostaining

Cells and tissues or organoids were fixed by fresh ice-cold 4% PFA for 15-30 minutes and overnight, respectively. After fixation, immunostaining was done by following our previously described protocol[54]. Primary antibodies were used as follows: anti-Tuj-1 antibodies (mouse, Sigma, T8860 , 1:5000; rabbit, Covance Research Products, PRB-435P, 1:5000), 3BH10 antibody (Mouse，Sigma, P1874，1:10000), EM48 (1:1000, MAB5374, Sigma-Aldrich), anti-Bassoon antibody (mouse, Abcam, AB82958,1:1000), anti GABA antibodies (rabbit, Sigma, A2052, 1:5000; mouse; Sigma, A0310，1:500), Clathrin antibody (Rabbit, Abcam, ab21679, 1:1000), GM130 antibody (Rabbit, Abcam, ab52649, 1:1000), ATXN-3 antibody (Merk, MAB5360, 1:500), HTT antibody (3E10, sc-47757, 1:400), IHC-plus™ Polyclonal Rabbit anti-Human

HTT / Huntingtin Antibody (C-Terminus, LS-B11011, 1:200), ARF1 antibodies (10790-1-AP and 68069-1-Ig, Proteintech, 1：500). Secondary antibodies used were as follows: Alexa Fluro 488 Donkey anti-mouse IgG (Invitrogen, Molecular Probe, A21202, 1:1000), Alexa Fluro 594 Donkey anti-mouse IgG (Invitrogen, Molecular Probe, A21203,1:1000), Alexa Fluro 594 Donkey anti-rabbit IgG(Chemicon, A21207,1:1000), Alexa Fluro 488 Donkey anti-rabbit IgG (Invitrogen, Molecular Probe, A21206,1:1000), Alexa Fluro 594 Donkey anti-goat IgG (Invitrogen, Molecular Probe, A11058,1:1000) Cy5 AffiniPure Donkey Anti-Goat IgG (H+L) (Jackson, 705-175-147,1:300), Cy5 AffiniPure Donkey Anti-Rabbit IgG (H+L) (Jackson, 711-175-152,1:300), Alexa Fluo 633 Phalloidin (Invitrogen, A22284,1:200), Mito-Tracker™ Green (Invitrogen, M7514), ER-Tracker™ Green (Invitrogen, E34251), DAPI (Sigma, D9542), Phalloidin Alexa-633 or 488 (ThermoFisher, A12379 or A22284, 1:1000), GOLGI ID® Green assay kit (ENZO, ENZ-51028-K100).

Image scanning and processing

The immunostaining slides were scanned by Zeiss 710/880 or Leica SP8 Confocal Microscopy with Z-stack. Ultra-high resolutions images were scanned by Structured Illumination microscopy (SIM) (Nikon, Japan). All image calibrations were performed by Fiji imageJ (Fiji, NIH, Bethesda, MD, USA) or IMARIS software (Bitplane AG, Zürich, Switzerland). 3D renderings were done by IMARIS surface.

Statistical analyses

All statistical analyses were done in GraphPad Prism.

Vector and Vector transfection

Fibroblasts were cultured in 12-well dishes and transfected each well with 2 μg the vector containing EGFP-Q19, 23, and 74 that have the first exon of *HTT* or *mHTT* gene that contain 19, 23 and 74 CAG repeats by applying

Lipofectamine 2000 according to the manufacturer's protocol and maintained the cells for another 3h before treatment. 48 h after transfection, the cells were fixed and immunostained.

More material and methods are included in supplementary information.

Results

Identification of a novel family with HD

We identified an inherited disease family in Inner Mongolia, China. The patients show an adult-onset, inheritable disease characterized by an abnormal gait, uncontrolled arm, leg, and head movements, and psychiatric abnormalities; some patients with severe syndromes show mania and pica; early symptoms include uncontrolled eye blinks, unintentional loss of objects in hands or uncontrolled temper, and accidental injuries. A total of 24 people had identifiable syndromes **(Fig. 1A; Table S1, and video-S1)).** The reported symptoms appeared at ages 24 to 50; patients died from 35 to 56 **(Fig. 1B, Table S1, and video-S1)**. Genomic sequencing of blood samples revealed that the patients in this family harbor typical CAG expansion in *HTT* **(Fig. 1C),** ranging from 44 to 59 repeats, compared to 19 (20/21) or 18 (1/21) CAG repeats in healthy alleles. Consistent with polyQ pathogenesis, CAG lengths correlated with disease onset age, symptom severity, and death age **(Fig. 1D; Table S1).** Our data showed that we identified a novel family with HD in the Mongolian population.

Large polyQ assembly of HTTs is present in all fibroblasts of the HD family

We collected skin samples from 14 family members, including 9 patients with HD and 5 healthy siblings, and cultured and enriched their fibroblasts. To determine the polyQ status in the cells of the *de novo* HD family, we stained fibroblasts with 3B5H10 antibody, an antibody against polyQ that recognizes both polyQ of both HTT and mHTT[55]. By using high-resolution scanning, we observed that the polyQ of fibroblasts, including patients and healthy siblings,

exhibited well-organized assemblies that resembled knitted fabrics formed by two parallel and interfused spindles (**Fig. 1E),** indicating that HTTs aggregates are well-organized assemblies but not a disorganized structure. Contrary to other observations[56], phalloidin counterstaining showed that polyQ assembly did not regularly parallel actin filaments and randomly crossed and knitted actin filaments **(Fig. 1E)**. Multiple α-helices and PolyQ form a stiff and rigid protein[26-28]. Strikingly, 3D rendered tomography showed that polyQ assembly in fibroblasts twisted with or deformed the nuclear membrane **(Fig. 1E).** Notably, the size of polyQ assemblies with mHTT was larger than that of polyQ assemblies without mHTT in fibroblasts **(Fig. 1F);** the polyQ assemblies with mHTT in fibroblasts from late- and moderate-stage HD patients were smaller than those in early-stage and nonsyndrome HD fibroblasts **(Fig. 1G)**. Large well organized polyQ assemblies are common characteristics of the fibroblasts of HD patients and healthy siblings.

PolyQ assemblies include flat Golgi stacks/ cisternae and dissemble in the mitotic fibroblasts with fragmented Golgi

mHTT dismantles mitochondria and rough endoplasmic reticulum (rER)[30,57,58]. Thus, we costained the mitochondria (Mito) or rER of the fibroblasts from the family with Mito or ER Tracker and the polyQ assemblies with 3B5H10 antibody and observed that the mitochondria in HD fibroblasts were morphologically similar to those in their healthy siblings and evenly distributed in polyQ assemblies and no polyQ assemblies region **(Fig. S1A).** The polyQ assemblies with mHTT or without mHTT rarely contacted the rER **(Fig. S1B).** The calibration of distance showed that the mitochondria also did not have a preference for polyQ assembly with mHTT **(Fig.S1C).** The polyQ assemblies with mHTT or without mHTT heavily fragmented in mitotic and apoptotic cells **(Fig. S1D-E)**. The size of polyQ assemblies in apoptotic and mitotic cells are far smaller than in non-mitotic cells **(Fig. S1F).**

Ultrastructural evidence has shown that HTT is localized on the surface of the flat Golgi, and that mHTT also impairs Golgi trafficking[32,40,59]. To our

knowledge, the polyQ assemblies morphologically resemble Golgi ribbons. Thus, we immunostained the Golgi with GM130 antibody, polyQ assemblies with 3B5H10 antibody, and F-actin with phalloidin to visualize the spatial relationship of polyQ assemblies with the Golgi. Using structural illumination microscopy (SIM) scanning with near 64 nm resolution and rendering tomography, we observed that the polyQ assemblies include flat Golgi stacks; the Golgi stack that stood between the internal space of two parallel spindles of polyQ assemblies was flat, and an isthmus in Golgi cisternae appeared where polyQ rings completely circled Golgi cisternae **(Fig. 2A, B)**. The overlapping volume of polyQ assemblies with the Golgi is far larger than that of F-actin **(Fig. 2C).** Notably, flat Golgi stacks are partially and asymmetrically covered by polyQ assemblies with mHTT compared to the Golgi cisternae seized by polyQ assemblies without mHTT **(Fig. 2A, B and 2D).**

ARFIP2, an ADP-ribosylation factor (ARF1) and ARF6 binding protein, conjugates to HTTs[60]. The GDP of ARF1 were converted into GTP by guanine nucleotide-exchange factors (GEFs), then conjugated to the Golgi[61,62]. The Golgi binding AFR-GTPs regulate Golgi vesicle formation and Golgi structure[61,62]. The 3D high-resolution images of immunostaining with ARF1 and 3B5H10 antibodies revealed that ARF1 attached to the inner domain of two paralleled polyQ spindles **(Fig. 2E).** The polyQ assemblies with mHTT attached fewer ARF1 than polyQ assemblies without mHTT in the fibroblasts **(Fig. 2F)**. The 3D high-resolution images of immunostaining with ARF1 and GM130 antibodies showed that the Golgi in HD fibroblasts were attached fewer ARF1 than the Golgi in healthy fibroblasts **(Fig. 2G, H).**

Clathrin vesicles are sorted on the Golgi[63]. To see if the lower levels of ARF1 on the Golgi of HD fibroblasts reduced the Golgi sorting, we have Golgi sorting activities by clathrin antibody immunostaining. Consistent with other observations[64], clathrin+ vesicles preferentially distributed along or conjugated with polyQ assemblies with or without mHTT **(Fig. 2I).** Notably, clathrin^{+} vesicles were also distributed along or conjugated to the segments of

the polyQ assemblies that closely attached or partially poked the nucleus of the fibroblasts **(Fig. 2I)**. Clathrin+ vesicles sort on the trans-Golgi network (TGN)[63]. We noticed that the clathrin$^+$ vesicles of polyQ assemblies were mainly present on the opposite side of the actin filament in the dishes **(Fig. 2J).** PolyQ assemblies without mHTT scaffolded/attached more clathrin$^+$ vesicles than polyQ assemblies with mHTT **(Fig. 2K, L).** Of note, the thicker GM130$^+$ Golgi in the fibroblasts were short of polyQ attachments **(Fig. S2A-C).** PFA fixed polyQ assemblies severely fragmented when the cells were stored in PBS or 30% sucrose buffer over 48 h postfixation **(Fig. S2D)**.

The Golgi fragments during cell mitosis and reassembles at the end of mitosis[65,66]. Both polyQ assemblies and GM130 stained Golgi stacks/ribbon fragmented together during prometaphase (28 cells from 6 samples) and anaphase (23 cells from 6 samples) and reassembled at late telophase (22 cells from 6 samples), and small Golgi and polyQ attached each other in mitotic cells **(Fig. 3A).** Brefeldin A (BFA) blocks the attaching of ARF to Golgi via inhibiting GEFs[67]. To see if the conjugation of HTT assemblies to Golgi mainly depends on ARF, we inhibited the conversion of ARF-GDP to ARF-GTP by BFA in the fibroblasts. Compared to the mitotic cells, BFA-treated fibroblasts liberated small GM130$^+$ Golgi from the polyQ assemblies **(Fig.3B, C).** The liberation of small Golgi from polyQ assemblies caused the fragmentation and degradation of polyQ and Golgi in HD and healthy fibroblasts **(Fig. S3A-E).** Most fragmented polyQ but not Golgi in BFA-treated fibroblasts were conjugated by ARF1 **(Fig. 3D, E)**, consistent with our observation in the neuronal tube[68].

To determine whether the polyQ assemblies stained by 3B5H10 include a large number of HTTs, we selected two HTT antibodies, including an EM48 antibody that binds the first 256 amino acids that excludes the polyQ stretch of HTT and huntingtin antibody (3E10) that corresponds to the HDA region (amino acids 1171-1177) of HTT, to determine the relationship of HTTs with the Golgi apparatus. The 3E10 and EM48 staining patterns were nearly

identical to 3B5H10 antibody immunostaining patterns in the fibroblasts **(Fig. 3F, G).** These data indicate that polyQ assemblies in fibroblasts are mainly composed of HTTs. Eight proteins in human cells, including Atrophin, Androgen receptor, Ataxin-1, 2, 3, and 7, and Calcium channel, also contain polyQ, and expansion of polyQ in the eight proteins causes neurodegenerative disease[69]. Based on the cellular localization, we also selected ATXN-3 antibody and coimmunostained the family fibroblasts with GM130 and the ATXN3 antibodies and found that ATXN3 rarely overlapped with the Golgi apparatus **(Fig. S4A, B)**. The HTT fragment of the first exon is pathogenic and widely used for constructing HD models[37,70]. To determine whether the transfected exogenous HTT fragment of the first exon can be recruited into polyQ assemblies, we transfected fibroblasts with three vectors of the *HTT* first exon containing 19, 23, and 74 CAGs, respectively. The exogenous HTT fragments of the first exon rarely recruited into endogenous polyQ assemblies of fibroblasts **(Fig. S4C, D).** Huntingtin-associated protein 40 (HAP40), a protein coevolved with HTT, binds to all three domains of HTT and stabilizes HTT[26,49]. To determine the spatial position of HAP40 in polyQ assemblies, we stained HD and healthy fibroblasts with HAP40 and 3B5H10 antibodies and found that the same amount of HAP40 binds polyQ assemblies with mHTT or without mHTT and mostly resides on the corner of rings in polyQ assemblies **(Fig. 3D, E)**. The polyQ fragments are also conjugated with HAP40 in the cell cycle **(Fig. S4E).** Together, polyQ assemblies of HTTs are the cytoskeleton-like framework that relates to the flat tomography of Golgi or scaffolds small Golgi stacks, and might coordinate the formation of large Golgi ribbons.

PolyQ assemblies with mHTT are fragile under glucose deprivation.

ARF-GTP mediates the binding of poyQ of HTTs to Golgi, and PolyQ assemblies with mHTTs attached fewer ARF1 than polyQ assemblies without mHTT. Thus, polyQ assemblies with mHTTs might be prone to disassembly due to energy deprivation. To compare the polyQ assemblies with mHTT with

the assambly without mHTT in energy-deprived conditions, we cultured fibroblasts from 4 patients with HD (CAG, 48, 49, 55, and 59) and 2 healthy siblings in low-glucose medium. We fixed cells at 24, 48, and 72 h and stained the polyQ assemblies with 3B5H10 antibody and actin with phalloidin. Compared to the stable F-actin filaments, the polyQ assemblies with mHTT are disassembled under glucose starvation **(Fig. 4A-C).** Interestingly, large polyQ assemblies without mHTT exhibit nearly unchanged, and the smaller polyQ fragments that surround large polyQ assemblies without mHTT are observably decreased under glucose starvation **(Fig. 4A)**. After culturing in low-glucose medium for 72 h, we switched low-glucose medium to high-glucose medium. After culturing for another 48 h, we stained the fibroblasts with the 3B5H10 antibody and observed that the polyQ assemblies with mHTT in fibroblasts were almost restored **(Fig. 4A-C)**.

To see the changes in Golgi of HD fibroblasts in glucose starvation, we also stained HD and healthy fibroblasts starved for 48h with 3B5H10 and GM130 antibodies. Paralleling the disassembly of polyQ assemblies with mHTT under glucose starvation, the Golgi ribbon of HD fibroblasts was disassembled, and most polyQ fragments/patches were attached to Golgi fragments **(Fig. 4D, E).** However, the structure of the Golgi ribbon was stable and the small Golgi fragments reduced in healthy fibroblasts after culturing in a low glucose medium for 48 h **(Fig. 4D, E),** which is consistent in the changes of polyQ assemblies without mHTT under stress **(Fig. 4A-C).** In addition, HD patient cells with more CAG repeats (55) had more fragmented Golgi than HD patient cells with less CAG repeat expansion (49) after 48 h of glucose deprivation **(Fig. 4F)**. Strikingly, the total size of the Golgi in HD cells was smaller than that in healthy sibling cells, and the size of the Golgi in HD fibroblasts decreased faster than that in healthy siblings after 48 h of glucose starvation **(Fig. 4G).** To see *in vivo* Golgi dynamics in a living cell under energy deprivation, we continuously monitored fibroblasts (CAG 49, 55, 19 and 19) stained by Golgi apparatus-selective dye after glucose starvation or

H_20_2 stimulation. The Golgi apparatus in HD patient fibroblasts was easier to fragment under glucose starvation than that in healthy fibroblasts **(Fig. 4H, I),** whereas the Golgi in the fibroblasts with and without mHTT uniformly fragment under H_20_2 stimulation **(Fig. S4F, G).** Our data revealed that the polyQ assembly parallels the formation of large and flat Golgi stacks/ribbons, and the incorporation of mHTT into polyQ assemblies impaired Golgi scaffolding by reducing ARF recruiting and creating vulnerable polyQ assemblies prone to disassembly on energy deprivation.

Free HTTs are enriched in ruffling membranes and endocytic vacuoles.

HTT activates dynamin which catalyzes membrane fission[50-52]. HTTs regulate intracellular vesicular transport by activating microtubule motors, and actin-associated adaptors[50,53]. Different parts of HTT show different roles[37]. To determine if the polyQ assemblies of HTT include a C-terminus, we stained polyQ with a 3B5H10 antibody and the C-terminus with a C-terminal specific antibody (LSB11011) and found that discontinuous C-terminal antibody signals colocalized with the polyQ assemblies **(Fig. 5A; two right panels).** Ruffling membrane, which is an actin-rich membrane protrusion, appears in cellular regions where plasma membrane reorganization happens dramatically[71]. Molecular scaffolds recruit to the ruffling membrane tips and couple the coordinated organization of actin filaments[72]. During analysis of the HTT C-terminal antibody 3B5H10 antibody, and phalloidin coimmunostaining images, we noticed that a significant amount of HTTs were located on the ruffling membrane and membrane curvature/endocytic vacuoles that originated from the ruffling border, resembling a queue **(Fig. 5A-C).** Contrary to kitted fabric-like polyQ assemblies of HTTs in the cytoplasm, the C-terminal signals of HTTs are stronger than the polyQ signal in ruffling membrane/membrane curvature/endocytic vacuoles; the actin bundle conjugated to the N-terminus of HTT (polyQ) **(Fig. 5A-D).** HTT^+ membrane curvature and vacuoles tightly attached to enriched actin bundles by N-terminal of HTT **(Fig. 5B-D)**, indicating the motility of these vacuoles.

HTT$^+$ vacuoles approximate the trans-Golgi network (TGN) and merge with polyQ assemblies with or without mHTT **(Fig. 5E)**. 3E10 and GM130 antibody immunostaining results in mitotic or apoptotic fibroblasts are consistent with C-terminus /3B5H10 and GM130 antibody immunostaining results **(Fig. S5A, B; Fig. S1D, E)**. Telophase cells were enriched in HTT$^+$ positive vesicles **(Fig. S5B)**. In addition, we noticed that large cellular fragments partially detached or fully departed from the cell contained higher levels of HTTs on the membrane **(Fig. S5C)**. The binding of HTTs to ruffling membrane/membrane curvature/endocytic vacuoles was also mediated by ARF1 **(Fig. S4D)**. These findings indicate that oligomeric HTT involves membrane vesicle trafficking and cellular membrane cycling **(Fig. 5F)**.

The characteristics of polyQ assemblies in striatal GABAergic neurons of HD patients

Patients with HD lose 50% of striatal GABAergic projection neurons at the late stage[6,73]. We constructed iPSCs of this family and differentiated iPSCs into GABAergic projection neurons by applying our previously reported protocol to compare the polyQ assemblies with mHTT in developing and mature striatal projection neurons with healthy polyQ assemblies[54]. We stained iPSC-derived neurons with the 3B5H10 antibody and antibodies against neuronal markers, including Tuj-1 or GABA, on different differentiation days to observe the time-dependent dynamics of polyQ assemblies. PolyQ in induced HD neurons was assembled into a medium-sized knitted fabric approximately 40 days, earlier than polyQ assemblies in healthy neurons **(Fig. 6A).** PolyQ assemblies in the neurons expanded in a time-dependent manner, the expansion of polyQ assemblies with mHTT was quicker than that of polyQ without mHTT, and the larger the polyQ assembly in the neurons, the more poking or twisting the nucleus was observed **(Fig. 6B, C).** Strikingly, on Day 90, heavily fragmented polyQ assemblies were substantially deposited in the neuronal nucleus of an HD patient with 59 CAG **(Fig. 6B; CAG: 59, 55, and 49).** Contrary to healthy neurons, fragmented polyQ in the nucleus of

GABAergic neurons (49, 55, and 59 CAGs) almost completely occupied the nucleus cultured from 90-178 days **(Fig. 6B and 6D);** time-dependent increases in nuclear twisting, accumulation, and poking of polyQ assemblies were noticed in the GABAergic neurons **(Fig. 6A, B).** The polyQ assemblies in the induced GABAergic neurons are reminiscent of large and long polyQ assemblies in freshly surged and fixed human brains **(Fig. 6E)** and other observations in murine brain[32,33]**.** Consistent with the high rigidity of HTTs that contain α-helices and homopolypeptide chains (HPPs) [27,28], DIC images revealed an observable deeply invaginated gorge where polyQ assemblies residing or traversing appeared in neurons, and 3D rendered tomography showed that polyQ spindles also created a gorge on the nuclear surface **(Fig. 6F**). The immunostaining results of EM48 antibody confirm that the polyQ assemblies in neurons contain large amounts of HTT **(Fig. S6A)**. Some mitochondria were randomly located in the polyQ assembly space or were twisted with the polyQ assembly **(Fig. S6B)**. F-actin did not parallel polyQ assembly in induced neurons **(Fig. S6C).**

Long-term cultured neurons with polyQ nuclear accumulation showed apoptotic signatures and nuclear membrane poking by short polyQ assemblies **(Fig. S6D-F).** Cytoplasmic polyQ assemblies sliced the nuclei of GABAergic neurons into several fragments **(Fig. S6F, G),** revealing the strong rigidity of polyQ assemblies. We also differentiated HD and healthy sibling hiPSCs into astrocytes by another protocol[74]. GFAP and EM48 antibodies immunostaining at 120 days showed that the HTT/mHTT assemblies in astrocytes from patients with HD are nearly identical to HTT/HTT assembly in healthy fibroblasts and rarely pokes or deposits into the nucleus **(Fig. S7A)**. Moreover, HTT/mHTT assembly also dented the nuclear surface of astrocytes **(Fig. S7B, right panel),** and HTT/mHTT assembly was larger than HTT/HTT assembly in induced astrocytes **(Fig. S7C)**. The microglia in ventricle zone (VZ) and cortical plate (CP) of developing human brain contain a small amount of polyQ assemblies and all processes of microglia did not have

3B5H10 antibody signals **(Fig.S7D, E).** Consistent with pathological findings[13,14], polyQ assemblies of HTTs are signatures of developing neuronal cells, including glial cells, and polyQ nuclear accumulation is a unique characteristic of neurons with mHTT.

PolyQ assemblies with mHTT in striatal neurons scaffolded fewer Golgi and clathrin+ vesicles than polyQ assemblies

HTT distributed in soma, dendrites, and axons, which match Golgi distribution patterns in the neurons, displayed a vesicle-associated protein characteristic[32,33]. We further characterized the relationship of polyQ assemblies with the Golgi in the neurons of striatal and cortical organoids (hStrO and hCO) **(Fig. 7A, B),** which we previously reported [68,75]. GM130 and 3B5H10 antibodies immunostaining in the striatal neurons of hStrOs showed that small Golgi scaffolds the extended polyQ assemblies **(Fig. 7C)**. Contrary to the observation in the fibroblasts mentioned above, a significant amount of GM130 stained Golgi did not conjugate with or close to polyQ assemblies **(Fig. 7C);** Multiple Golgi also resided in the polyQ assemblies, which traversed through the nuclear surface where a gorge formed in hStrO **(Fig. 7C).** PolyQ assemblies with mHTT in striatal neurons have a smaller overlapping volume with GM130-stained Golgi than polyQ assemblies without mHTT in the hStrO **(Fig. 7D, E)**. We also stained HD patients and healthy human hCO with 3B5H10 and GM130 antibodies. PolyQ assemblies included large flat Golgi stacks of cortical neurons in hCOs**,** and the tomography of flat Golgi in HD patient neurons that were included in polyQ assemblies was observably irregular compared to the neuronal flat Golgi in healthy siblings **(Fig. 7E)**. The immunostaining results of 3B5H10 and clathrin antibodies showed that clathrin^{+} vesicles preferentially distributed along or conjugated to polyQ assemblies with or without mHTT in cortical or striatal neurons of hStrO or hCO **(Fig. 7F).** Consistent with the results of fibroblasts, the overlapping volume of clathrin^{+} vesicles with polyQ assemblies with mHTT and the count of clathrin^{+} vesicles attached or approximated to polyQ assemblies with

mHTT were lower than those of polyQ assemblies without mHTT in hCO **(Fig. 7G)**.

Striatal projection neurons have extremely long dendrites and axon[76]. We observed that the longest polyQ assembly exceeded 60 μm in the projection neurons in 2D culture, resembling polyQ assemblies in the long projection of the human brain **(Fig. 7H, I; the left panel is a 3D image with 140 nm resolution)** and continuous polyQ assemblies formed by numerous rings with 60-120 nm (inner diameters) in the projections of striatal neurons 2D cultured for over 90 days, recapitulating the polyQ assemblies in human brain tissues **(Fig. 7J; a 3D image with near 64 nm resolution).** Extended polyQ assemblies with mHTT in neuronal projections included fewer fragmented/small Golgi than polyQ assemblies without mHTT **(Fig. 7K-M);** small Golgi resided in the hole of rings and scaffolded the outer spines of long polyQ assemblies in hStrO neurons **(Fig. 7N);** Clathrin^{+} vesicles also scaffolded polyQ assemblies and mainly resided on the two sides of the assemblies in the neurons of hStrO **(Fig. 7O).** Comparing with the continuous and intact polyQ assemblies in brain organoids **(Fig. S8A; Fig. 5H, I)**, most polyQ assemblies in surgical human brain samples were partially or heavily fragmented, and the extended polyQ assemblies were discontinuous **(Fig. S8A, B).** Furthermore, polyQ assemblies and Golgi heavily fragmented in the cells surrounding the necrotic cells in hStrO or hCO (**Fig. S8C)**. The more necrotic cells in hStrO/HCO, the heavier fragmentations of polyQ assemblies or Golgi **(Fig. S8C, D).** Most fragmented polyQ and Golgi in necrotic sites were attached by ARF1 in hStrO **(Fig. S9A)**. Compared to the extended and continuous polyQ assemblies in the neuroepithelial cells of VZ regions in hStrOs[68], the polyQ assemblies were fragmented and discontinuous in the VZ region of 9.5 gestational week (GW) fetal brain **(Fig. S9B, C),** reflecting the fragility of polyQ assemblies in postfixation. Consistent with our observation in Golgi-rich neural tube[68], incorporation of mHTT into polyQ assemblies impaired Golgi structure and sorting in striatal and cortical neurons of brain

organoids.

scRNA-seq data revealed that GABAergic neurons with mHTT reduced Golgi- or vesicle-related activities

To determine the biological effects of polyQ assemblies with mHTT and exclusive nuclear deposition in striatal GABAergic neurons, especially on Golgi-related and nuclear activities, we performed single-cell RNA sequencing (scRNA-seq) analyses of human striatal organoids (hStrOs) derived from hESC-H9 and hiPSC-8-12 (CAG 19) and HD hiPSC-7-2 (CAG 59) after culturing for 110 days. Transcriptomic data of 38,716 single cells were obtained after quality control and filtering **(Fig. 8A)**. Uniform manifold approximation and projection (UMAP) clustering identified four clusters in hStrOs that expressed cell-type-specific markers, including progenitors (VIM, NES, HES1), neurons (SYT1, DCX, STMN2), astrocytes (S100β, GFAP), and oligodendrocytes (OLIG2, SOX10) **(Fig. 8B, C and S10A, B)**. We further plotted the expression of brain region-specific markers in these clusters and found that both control and HD hStrOs are mainly composed of LGE progenitors and GABAergic neurons rather than cortical progenitors and glutaminergic neurons **(Fig. S10C,D)**, consistent with our protocols to generate hStrOs[75]. Based on the structural changes in the Golgi related to polyQ assemblies with mHTT**,** we compared the transcriptome of mature GABAergic neurons in the control group with that in the HD group after sorting the GABAergic neuron population by *GAD1* and *GAD2 genes,* a specific marker for mature GABAergic neurons **(Fig. 10D-F)**. In GABAergic neurons, the DEGs of HD hStrO extensively overlapped with those of hiPSC-derived hStrO (CAG 19) and hESC-derived hStrO, both for upregulated (321 genes) and downregulated genes (550 genes) **(Fig. 8D)**. Upregulated genes in GO terms are associated with nuclear activities, including ribonucleoprotein complex assembly, translational initiation, and regulation of translation, which might be related to the nuclear poking of polyQ assemblies or deposition of polyQ into the nucleus. Interestingly, the downregulated genes in GABAergic

neurons of HD hStrOs were notably enriched for GO terms associated with Golgi or Golgi-related functions, including Golgi vesicle transport, endoplasmic reticulum to Golgi vesicle−mediated transport, vesicle organization, endomembrane system organization, intracellular protein transport, and protein localization to membrane translation **(Fig. 8E)**. The downregulated genes in HD hStrOs belong to Golgi matrix proteins, including *GOLGA8A*, a structurally similar protein of GM130 enriched in neurons, *GOLGA4*, and Golgi matrix-associated GTPs that include *RAB6, ARL1/4C*, and *ARF1/3/4.* PolyQ assemblies with mHTT and HD Golgi attached fewer ARF1 than polyQ assemblies without mHTT and healthy Golgi in hStrOs, and the volume ratio of ARF1/polyQ or Golgi in HD patient striatal neurons are lower than the healthy neurons in hStrOs **(Fig. 8F-J)**. Lower ARF1 binding to HD Golgi in the cortical neurons of hCOs also existed **(Fig .S11A).** In addition, the bulk RNAseq data in hStrOs showed that *ARF1, ARF4, ARF-GEF2, ARF-GAP2, and IQSEC* downregulated in HD hStrOs. These data indicated that polyQ assemblies with mHTT decreased the functions of Golgi stacks/ribbons by reducing ARF-related activities.

Discussion

In this study, we revealed that polyQ aggregates of HTTs, including mHTT, are a large and well-organized scaffold formed by two or more long paralleled and interfused spindles which includes flat Golgi stacks/ribbons/vesicles, scaffolds clathrin vesicles and binds ARF1. The existence of mHTT in the polyQ assemblies impaired Golgi structure and stability, and reduced clathrin-coated vesicles and small Golgi vesicle scaffolding by reducing ARF-related activities. The existence of mHTT causes neuronal nuclear precipitations, especially in striatal GABAergic neurons. PolyQ assemblies, including polyQ assemblies with mHTT, in human cells are prone to fragment in postfixation and necrotic regions and are histologically unsuitable for storage. Our findings demonstrated that the polyQ aggregate of HTTs is a stable form in cells and a well-organized cytoplasmic scaffold for Golgi.

Here, our high-resolution images with near 64 nm resolution and 3D rendering tomography displayed the spatial and structural identities of polyQ assemblies of HTTs in fresh tissues and cells[77]. Our data also argue that the spatial structure of mHTT translated by exon-1 might does not participate in the highly organized polyQ assembly of HTT or mHTT[30,78,79]. Despite inconsistent data throughout existing publications[7,10-12], we noticed that multiple HTT antibody results are consistent with our data[33,32,64,80]. Others also observed the instability of HTTs in storage[9]. The nature of polyQ assemblies in postfixation and stresses might contribute to the inconsistency of HTT antibody staining throughout tissues and cells. A fresh fixation and immediate staining makes it possible to observe an entire huge polyQ assembly. We noticed that polyQ assemblies in most neurons were partially or completely fragmented in surgical brain samples, and freshly fixed fetal brain samples completely disappeared in some human brain samples stored in the fixative for a long time.

Golgi stacks are dynamic structures composed of 4-11 stapled cisternae in which newly synthesized soluble cargo proteins and lipids are processed

and sorted[63,81]. The Golgi ribbon comprises up to 100 flat stacks linked by tubular bridges in mammalian cells[63,81]. The Golgi matrix, a ribosome-free protein network surrounding the cisternae, supports the stack structure[82]. The inclusion of Golgi by polyQ assemblies indicated that rigid polyQ assemblies might support the Golgi matrix. Large Golgi stacks/ribbons in a cell are fragmented/disassembled in mitosis and stresses[83,84]. Fragmented Golgi in mitotic and stressed cells but not BFA-treated cells were attached by polyQ, indicating the structure of polyQ coupled with the dynamic Golgi. PolyQs naturally form a rigid aggregate. Thus, to what extent the aggregating nature of polyQ assists the formation of Golgi stacks/ribbons is worth exploring.

Despite no evidence indicating that HTT directly binds to ARF family protein or Guanine exchange factors (GEF), ARF regulates Golgi sorting[61]. ARFIP2, an ARF1 and ARF6 interacting protein, and Duo, a HAP1 conjugating protein and GEF[85], directly conjugate with HTTs[60]. Thus, polyQ assemblies might create a specific platform with multiple catalytic enzymes for Golgi activities where Golgi shaping, assembling, and sorting occur. Consistent with immunostaining, ScRNA data further revealed that Golgi functions are deregulated in HD striatal neurons. Golgi abnormalities, including structure and function, are common in neurodegenerative diseases[63,81]: The correct Golgi positioning is critical for cellular polarization and differentiation[86]; The precise localization of the Golgi apparatus mediates the simple spindle-like cells to form the dentate granule cells (DGCs)[87]; GM130 deletion causes neurodegeneration and ataxia[88]. Thus, the impaired Golgi related to mHTT might drive the pathogenesis of HD in developing and adult brains.

Our findings demonstrated that the aggregate of HTTs is a well-organized cytoplasmic assembly that forms a structural scaffold for Golgi, including Golgi stack/ribbon/ vesicles, and is prone to disassemble in BFA treatments, stresses, and postfixation. The existence of mHTT destabilizes the polyQ assemblies of HTTs by reducing ARF scaffolding and impairs Golgi structure and function in HD patient striatal/cortical neurons and fibroblasts.

Author contributions

HS and LM set this study. HS and LM performed most of the experiments; HS analyzed data, and prepared manuscripts; XC, WY, YL, BH, and JX have done image analysis and immunostaining. XC, LY and LM constructed organoids.

Financial supports

This study was supported by the projects, including the National Key Research and Development Program of China (2021YFA1101302; 2018YFA0108004), the National Natural Science Foundation of China (82071269; 81271259), and the Shanghai Municipal Planning Commission of Science and Research Fund (201840009).

Conflict of Interest

All authors claim that there are no conflicts of interest.

Reference

1. Walker FO. Huntington's disease. *Lancet.* 2007;369(9557):218-228.
2. Kernich CA. Huntington's disease. *Neurologist.* 2002;8(3):207-208.
3. Saudou F, Humbert S. The Biology of Huntingtin. *Neuron.* 2016;89(5):910-926.
4. Vonsattel JP, DiFiglia M. Huntington disease. *J Neuropathol Exp Neurol.* 1998;57(5):369-384.
5. Vonsattel JP, Myers RH, Stevens TJ, Ferrante RJ, Bird ED, Richardson EP, Jr. Neuropathological classification of Huntington's disease. *J Neuropathol Exp Neurol.* 1985;44(6):559-577.
6. Mann DM, Oliver R, Snowden JS. The topographic distribution of brain atrophy in Huntington's disease and progressive supranuclear palsy. *Acta Neuropathol.* 1993;85(5):553-559.
7. Hickman RA, Faust PL, Marder K, Yamamoto A, Vonsattel JP. The distribution and density of Huntingtin inclusions across the Huntington disease neocortex: regional correlations with Huntingtin repeat expansion independent of pathologic grade. *Acta Neuropathol Commun.* 2022;10(1):55.
8. Sharp AH, Loev SJ, Schilling G, et al. Widespread expression of Huntington's disease gene (IT15) protein product. *Neuron.* 1995;14(5):1065-1074.
9. Ferrante RJ, Gutekunst CA, Persichetti F, et al. Heterogeneous topographic and cellular distribution of huntingtin expression in the normal human neostriatum. *J Neurosci.* 1997;17(9):3052-3063.
10. Tousley A, Iuliano M, Weisman E, et al. Huntingtin associates with the actin cytoskeleton and alpha-actinin isoforms to influence stimulus dependent morphology changes. *PLoS One.* 2019;14(2):e0212337.
11. Shen M, Wang F, Li M, et al. Reduced mitochondrial fusion and Huntingtin levels contribute to impaired dendritic maturation and behavioral deficits in Fmr1-mutant mice. *Nat Neurosci.* 2019;22(3):386-400.
12. Barnat M, Capizzi M, Aparicio E, et al. Huntington's disease alters human neurodevelopment. *Science.* 2020;369(6505):787-793.
13. DiFiglia M, Sapp E, Chase KO, et al. Aggregation of huntingtin in neuronal intranuclear inclusions and dystrophic neurites in brain. *Science.* 1997;277(5334):1990-1993.
14. Gutekunst CA, Li SH, Yi H, et al. Nuclear and neuropil aggregates in Huntington's disease: relationship to neuropathology. *J Neurosci.* 1999;19(7):2522-2534.
15. Arrasate M, Mitra S, Schweitzer ES, Segal MR, Finkbeiner S. Inclusion body formation reduces levels of mutant huntingtin and the risk of neuronal death. *Nature.* 2004;431(7010):805-810.
16. Saudou F, Finkbeiner S, Devys D, Greenberg ME. Huntingtin acts in the nucleus to induce apoptosis but death does not correlate with the formation of intranuclear inclusions. *Cell.* 1998;95(1):55-66.
17. Kim M, Lee HS, LaForet G, et al. Mutant huntingtin expression in clonal striatal cells: dissociation of inclusion formation and neuronal survival by caspase inhibition. *J Neurosci.* 1999;19(3):964-973.
18. Poirier MA, Li HL, Macosko J, Cai SW, Amzel M, Ross CA. Huntingtin spheroids and protofibrils as precursors in polyglutamine fibrilization. *Journal of Biological Chemistry.*

2002;277(43):41032-41037.
19. Mukai H, Isagawa T, Goyama E, et al. Formation of morphologically similar globular aggregates from diverse aggregation-prone proteins in mammalian cells. *Proc Natl Acad Sci U S A.* 2005;102(31):10887-10892.
20. Legleiter J, Mitchell E, Lotz GP, et al. Mutant huntingtin fragments form oligomers in a polyglutamine length-dependent manner in vitro and in vivo. *J Biol Chem.* 2010;285(19):14777-14790.
21. Takahashi T, Kikuchi S, Katada S, Nagai Y, Nishizawa M, Onodera O. Soluble polyglutamine oligomers formed prior to inclusion body formation are cytotoxic. *Hum Mol Genet.* 2008;17(3):345-356.
22. Lajoie P, Snapp EL. Formation and toxicity of soluble polyglutamine oligomers in living cells. *PLoS One.* 2010;5(12):e15245.
23. Hatters DM, Hannan AJ, Springer Science+Business Media. *Tandem repeats in genes, proteins, and disease : methods and protocols.* New York: Humana Press; 2013.
24. Jimenez-Sanchez M, Licitra F, Underwood BR, Rubinsztein DC. Huntington's Disease: Mechanisms of Pathogenesis and Therapeutic Strategies. *Cold Spring Harb Perspect Med.* 2017;7(7).
25. Tabrizi SJ, Flower MD, Ross CA, Wild EJ. Huntington disease: new insights into molecular pathogenesis and therapeutic opportunities. *Nat Rev Neurol.* 2020;16(10):529-546.
26. Guo Q, Bin H, Cheng J, et al. The cryo-electron microscopy structure of huntingtin. *Nature.* 2018;555(7694):117-120.
27. Sivaramakrishnan S, Spink BJ, Sim AY, Doniach S, Spudich JA. Dynamic charge interactions create surprising rigidity in the ER/K alpha-helical protein motif. *Proc Natl Acad Sci U S A.* 2008;105(36):13356-13361.
28. Dougan L, Li J, Badilla CL, Berne BJ, Fernandez JM. Single homopolypeptide chains collapse into mechanically rigid conformations. *Proc Natl Acad Sci U S A.* 2009;106(31):12605-12610.
29. Isas JM, Langen A, Isas MC, Pandey NK, Siemer AB. Formation and Structure of Wild Type Huntingtin Exon-1 Fibrils. *Biochemistry-Us.* 2017;56(28):3579-3586.
30. Bauerlein FJB, Saha I, Mishra A, et al. In Situ Architecture and Cellular Interactions of PolyQ Inclusions. *Cell.* 2017;171(1):179-187 e110.
31. Scherzinger E, Sittler A, Schweiger K, et al. Self-assembly of polyglutamine-containing huntingtin fragments into amyloid-like fibrils: implications for Huntington's disease pathology. *Proc Natl Acad Sci U S A.* 1999;96(8):4604-4609.
32. DiFiglia M, Sapp E, Chase K, et al. Huntingtin is a cytoplasmic protein associated with vesicles in human and rat brain neurons. *Neuron.* 1995;14(5):1075-1081.
33. Ko J, Ou S, Patterson PH. New anti-huntingtin monoclonal antibodies: implications for huntingtin conformation and its binding proteins. *Brain Res Bull.* 2001;56(3-4):319-329.
34. Zeitlin S, Liu JP, Chapman DL, Papaioannou VE, Efstratiadis A. Increased apoptosis and early embryonic lethality in mice nullizygous for the Huntington's disease gene homologue. *Nat Genet.* 1995;11(2):155-163.
35. Dragatsis I, Efstratiadis A, Zeitlin S. Mouse mutant embryos lacking huntingtin are

rescued from lethality by wild-type extraembryonic tissues. *Development.* 1998;125(8):1529-1539.
36. Duyao MP, Auerbach AB, Ryan A, et al. Inactivation of the mouse Huntington's disease gene homolog Hdh. *Science.* 1995;269(5222):407-410.
37. Yang H, Yang S, Jing L, et al. Truncation of mutant huntingtin in knock-in mice demonstrates exon1 huntingtin is a key pathogenic form. *Nat Commun.* 2020;11(1):2582.
38. Mehta SR, Tom CM, Wang Y, et al. Human Huntington's Disease iPSC-Derived Cortical Neurons Display Altered Transcriptomics, Morphology, and Maturation. *Cell Rep.* 2018;25(4):1081-1096 e1086.
39. Milnerwood AJ, Cummings DM, Dallerac GM, et al. Early development of aberrant synaptic plasticity in a mouse model of Huntington's disease. *Hum Mol Genet.* 2006;15(10):1690-1703.
40. del Toro D, Alberch J, Lazaro-Dieguez F, et al. Mutant huntingtin impairs post-Golgi trafficking to lysosomes by delocalizing optineurin/Rab8 complex from the Golgi apparatus. *Mol Biol Cell.* 2009;20(5):1478-1492.
41. Kim J, Moody JP, Edgerly CK, et al. Mitochondrial loss, dysfunction and altered dynamics in Huntington's disease. *Hum Mol Genet.* 2010;19(20):3919-3935.
42. Costa V, Giacomello M, Hudec R, et al. Mitochondrial fission and cristae disruption increase the response of cell models of Huntington's disease to apoptotic stimuli. *EMBO Mol Med.* 2010;2(12):490-503.
43. Shirasaki DI, Greiner ER, Al-Ramahi I, et al. Network organization of the huntingtin proteomic interactome in mammalian brain. *Neuron.* 2012;75(1):41-57.
44. Grima JC, Daigle JG, Arbez N, et al. Mutant Huntingtin Disrupts the Nuclear Pore Complex. *Neuron.* 2017;94(1):93-107 e106.
45. Milnerwood AJ, Gladding CM, Pouladi MA, et al. Early increase in extrasynaptic NMDA receptor signaling and expression contributes to phenotype onset in Huntington's disease mice. *Neuron.* 2010;65(2):178-190.
46. Lee H, Fenster RJ, Pineda SS, et al. Cell Type-Specific Transcriptomics Reveals that Mutant Huntingtin Leads to Mitochondrial RNA Release and Neuronal Innate Immune Activation. *Neuron.* 2020;107(5):891-+.
47. Silvestroni A, Faull RL, Strand AD, Moller T. Distinct neuroinflammatory profile in post-mortem human Huntington's disease. *Neuroreport.* 2009;20(12):1098-1103.
48. Machiela E, Southwell AL. Biological Aging and the Cellular Pathogenesis of Huntington's Disease. *J Huntingtons Dis.* 2020;9(2):115-128.
49. Harding RJ, Deme JC, Hevler JF, et al. Huntingtin structure is orchestrated by HAP40 and shows a polyglutamine expansion-specific interaction with exon 1. *Commun Biol.* 2021;4(1):1374.
50. Caviston JP, Zajac AL, Tokito M, Holzbaur EL. Huntingtin coordinates the dynein-mediated dynamic positioning of endosomes and lysosomes. *Mol Biol Cell.* 2011;22(4):478-492.
51. Caviston JP, Ross JL, Antony SM, Tokito M, Holzbaur EL. Huntingtin facilitates dynein/dynactin-mediated vesicle transport. *Proc Natl Acad Sci U S A.* 2007;104(24):10045-10050.

52. Morlot S, Roux A. Mechanics of dynamin-mediated membrane fission. *Annu Rev Biophys.* 2013;42:629-649.
53. Olenick MA, Holzbaur ELF. Dynein activators and adaptors at a glance. *J Cell Sci.* 2019;132(6).
54. Ma L, Hu B, Liu Y, et al. Human embryonic stem cell-derived GABA neurons correct locomotion deficits in quinolinic acid-lesioned mice. *Cell Stem Cell.* 2012;10(4):455-464.
55. Owens GE, New DM, West AP, Bjorkman PJ. Anti-PolyQ Antibodies Recognize a Short PolyQ Stretch in Both Normal and Mutant Huntingtin Exon 1. *Journal of Molecular Biology.* 2015;427(15):2507-2519.
56. Tousley A, Iuliano M, Weisman E, et al. Huntingtin associates with the actin cytoskeleton and alpha-actinin isoforms to influence stimulus dependent morphology changes. *Plos One.* 2019;14(2).
57. Sharma A, Behl T, Sharma L, Aelya L, Bungau S. Mitochondrial Dysfunction in Huntington's disease: Pathogenesis and Therapeutic Opportunities. *Curr Drug Targets.* 2021.
58. Guedes-Dias P, Holzbaur ELF. Huntingtin Fibrils Poke Membranes. *Cell.* 2017;171(1):32-33.
59. del Toro D, Canals JM, Gines S, Kojima M, Egea G, Alberch J. Mutant huntingtin impairs the post-Golgi trafficking of brain-derived neurotrophic factor but not its Val66Met polymorphism. *J Neurosci.* 2006;26(49):12748-12757.
60. Peters PJ, Ning K, Palacios F, et al. Arfaptin 2 regulates the aggregation of mutant huntingtin protein. *Nat Cell Biol.* 2002;4(3):240-245.
61. D'Souza-Schorey C, Chavrier P. ARF proteins: roles in membrane traffic and beyond. *Nat Rev Mol Cell Biol.* 2006;7(5):347-358.
62. Bonifacino JS, Lippincott-Schwartz J. Coat proteins: shaping membrane transport. *Nat Rev Mol Cell Biol.* 2003;4(5):409-414.
63. Klumperman J. Architecture of the mammalian Golgi. *Cold Spring Harb Perspect Biol.* 2011;3(7).
64. Velier J, Kim M, Schwarz C, et al. Wild-type and mutant huntingtins function in vesicle trafficking in the secretory and endocytic pathways. *Exp Neurol.* 1998;152(1):34-40.
65. Corda D, Barretta ML, Cervigni RI, Colanzi A. Golgi complex fragmentation in G2/M transition: An organelle-based cell-cycle checkpoint. *IUBMB Life.* 2012;64(8):661-670.
66. Tomas M, Martinez-Alonso E, Martinez-Martinez N, Cara-Esteban M, Martinez-Menarguez JA. Fragmentation of the Golgi complex of dopaminergic neurons in human substantia nigra: New cytopathological findings in Parkinson's disease. *Histol Histopathol.* 2021;36(1):47-60.
67. Robineau S, Chabre M, Antonny B. Binding site of brefeldin A at the interface between the small G protein ADP-ribosylation factor 1 (ARF1) and the nucleotide-exchange factor Sec7 domain. *Proc Natl Acad Sci U S A.* 2000;97(18):9913-9918.
68. Liu Y, Chen X, Ma Y, et al. Endogenous mutant Huntingtin alters the corticogenesis via lowering Golgi recruiting ARF1 in cortical organoid. *Mol Psychiatry.* 2024.
69. Paulson HL, Bonini NM, Roth KA. Polyglutamine disease and neuronal cell death. *Proc Natl Acad Sci U S A.* 2000;97(24):12957-12958.

70. Brooks SP, Dunnett SB. Mouse Models of Huntington's Disease. *Curr Top Behav Neurosci.* 2015;22:101-133.
71. Pittman M, Iu E, Li K, et al. Membrane Ruffling is a Mechanosensor of Extracellular Fluid Viscosity. *Nat Phys.* 2022;18(9):1112-1121.
72. Mahankali M, Peng HJ, Cox D, Gomez-Cambronero J. The mechanism of cell membrane ruffling relies on a phospholipase D2 (PLD2), Grb2 and Rac2 association. *Cell Signal.* 2011;23(8):1291-1298.
73. Kanazawa I. [Huntington's disease--clinical characteristics and physiopathology]. *Nihon Naika Gakkai Zasshi.* 1998;87(9):1647-1657.
74. Krencik R, Weick JP, Liu Y, Zhang ZJ, Zhang SC. Specification of transplantable astroglial subtypes from human pluripotent stem cells. *Nat Biotechnol.* 2011;29(6):528-534.
75. Chen X, Saiyin H, Liu Y, et al. Human striatal organoids derived from pluripotent stem cells recapitulate striatal development and compartments. *Plos Biol.* 2022;20(11):e3001868.
76. Lanciego JL, Luquin N, Obeso JA. Functional neuroanatomy of the basal ganglia. *Cold Spring Harb Perspect Med.* 2012;2(12):a009621.
77. Heintzmann R, Huser T. Super-Resolution Structured Illumination Microscopy. *Chem Rev.* 2017;117(23):13890-13908.
78. Masnata M, Sciacca G, Maxan A, et al. Demonstration of prion-like properties of mutant huntingtin fibrils in both in vitro and in vivo paradigms. *Acta Neuropathol.* 2019;137(6):981-1001.
79. Pearce MMP, Kopito RR. Prion-Like Characteristics of Polyglutamine-Containing Proteins. *Cold Spring Harb Perspect Med.* 2018;8(2).
80. Wheeler VC, White JK, Gutekunst CA, et al. Long glutamine tracts cause nuclear localization of a novel form of huntingtin in medium spiny striatal neurons in HdhQ92 and HdhQ111 knock-in mice. *Hum Mol Genet.* 2000;9(4):503-513.
81. Liu JY, Huang Y, Li T, Jiang Z, Zeng LW, Hu ZP. The role of the Golgi apparatus in disease (Review). *Int J Mol Med.* 2021;47(4).
82. Ravichandran Y, Goud B, Manneville JB. The Golgi apparatus and cell polarity: Roles of the cytoskeleton, the Golgi matrix, and Golgi membranes. *Curr Opin Cell Biol.* 2020;62:104-113.
83. Wei JH, Seemann J. Mitotic division of the mammalian Golgi apparatus. *Semin Cell Dev Biol.* 2009;20(7):810-816.
84. Machamer CE. The Golgi complex in stress and death. *Front Neurosci.* 2015;9:421.
85. Wu LL, Zhou XF. Huntingtin associated protein 1 and its functions. *Cell Adh Migr.* 2009;3(1):71-76.
86. Yadav S, Linstedt AD. Golgi positioning. *Cold Spring Harb Perspect Biol.* 2011;3(5).
87. Rao S, Kirschen GW, Szczurkowska J, et al. Repositioning of Somatic Golgi Apparatus Is Essential for the Dendritic Establishment of Adult-Born Hippocampal Neurons. *J Neurosci.* 2018;38(3):631-647.
88. Liu C, Mei M, Li Q, et al. Loss of the golgin GM130 causes Golgi disruption, Purkinje neuron loss, and ataxia in mice. *Proc Natl Acad Sci U S A.* 2017;114(2):346-351.

Figure legends

Figure 1. Identification of a family with HD

A. The pedigree of the family with HD.

B. Typical disease symptoms and progression patterns of 3 HD patients recorded for 10 years, including 2 males and 1 female**.**

C. PCR results showed that 8 of 14 are heterogeneous; the upper band is the expanded CAGs (upper panel). The Sanger sequencing data revealed that the heterogeneous segment contain expanded CAGs (the lower panel; 49 repeats; the red arrows, the early and the end of CAGs). (See also Table-S1). M, control band (CAG 35); L, Healthy person from the same region.

D. The correlations of CAG repeat with disease onset age. Spearmen's correlation.

E. 3B5H10 antibody and phalloidin staining showed polyQ distribution patterns in the fibroblasts of healthy (CAG 19) and patient (CAG 59). 3D rendered tomography by IMARIS revealed the spatial relationships of polyQ assemblies with the nuclear surface and F-actin filaments (white arrows, polyQ puncta included in the nucleus; yellow arrows, nuclear twisting/denting; taken by Zeiss 880). The yellow arrows in rendered image of DAPI revealed the deformation of nuclear surface.

F. The size of polyQ assemblies in the fibroblasts of healthy siblings (N=4; cells, n=306) and HD patients (N=4; CAGs: 59, 55, 49, and 4 7; cells, n=783). The size was measured by Fiji ImageJ. Student *t*-test; **, p <0.01. Data, means± s.e.m.

G. Comparing the size of polyQ assembly in an early stage (E) and asymptotes (N) (n=2) with moderate (M) and late (L) stage HD patient fibroblasts (n=2) (CAGs: 59, 55, 49, and 48). The size is measured by Fiji ImageJ. Student *t*-test; **, p<0.01; Data, mean ± SD

Figure 2. PolyQ assemblies include flat Golgi and attach to the small Golgi fragments

A, B. GM130 and 3B5H10 antibodies and phalloidin staining in healthy sibling

and HD fibroblasts showed that polyQ assemblies conjugate with Golgi stack and small Golgi fragments (z-stack intervals, 0.2μm; taken by SIM microscopy with near 64 nm resolution). The rendering tomography of Z-stacked images revealed the spatial relationship of polyQ assemblies with Golgi stack and small Golgi; the Golgi stack resides in the inner space of polyQ assemblies, and Golgi was circled by an arm-like structure of polyQ (yellow arrows, isthmus; blue arrows, the arm of polyQ; the boxed region, the magnified part in the right panel).

C. Comparing the overlapped volume of Golgi with polyQ assemblies with phalloidin-stained F-actin measured by the object-object statistic of IMARIS.

D. The spatial relationships of polyQ assemblies with Golgi stacks. The arm-like structure of polyQ assemblies without mHTT that circle Golgi is more symmetric than that of polyQ assemblies with mHTT (white arrows, asymmetrically circled Golgi). The count of asymmetric segments in HD healthy fibroblasts.

E. ARF1 and 3B5H10 antibodies immunostaining in the HD (CAG 59) and healthy fibroblasts revealed that AFR1 binds to the inner surface of polyQ spindles.

F. The count of polyQ assemblies binding ARF1 in the HD (CAG 59) and healthy fibroblasts. Student *t*-test; **, $p<0.01$.

G. ARF1 and 3B5H10 antibodies staining in the HD (CAG 59) and healthy fibroblasts revealed large Golgi ribbons.

H. The overlapped volume of ARF1+ puncta with GM130+ Golgi. Student t-test; *, $p<0.05$.

I. The representative images of clathrin and 3B5H10 antibodies immunostaining in the fibroblasts of an HD patient (CAG 44) and healthy fibroblasts (Inner inserted panels, the angled views; the upper panel, the lateral view of Z-stacked images).

J. The lateral views of clathrin and 3B5H10 antibodies and phalloidin coimmunostaining images revealed that clathrin vesicle that conjugate to

polyQ present on the opposite side of F-actin (white arrow, clathrin; yellow arrow, F-actin).

K. L. The number of Clathrin^{+} vesicles overlapped with polyQ assemblies with or without mHTT. Data, number of clathrin+ vesicles surrounded within 0.5μm of the polyQ assemblies. Student *t*-test; *, $p<0.05$

Fig. 3. The characteristics of polyQ assemblies of HTTs in mitotic cells and BFA-treated cells.

A. 3B5H10 and GM130 antibodies immunostaining images in the mitotic fibroblasts, including prometaphase, anaphase, and telophase, were obtained by SIM microscopy. The insert images of DAPI (gray) showed the chromatin structure of the nucleus. The right panels are a sectional view of boxed region (anaphase and telophase).

B. GM130 and 3B5H10 antibody immunostaining in BFA-treated fibroblasts revealed that small GM130^{+} vesicles which surrounded a larger polyQ assemblies (CAG 49) and the most fragmented Golgi that circled a larger 3B5H10 assembly lacks 3B5H10 puncta conjugation. The boxed region is the magnified/rendered region in the middle two panels. The right panel is a control cell (CTR).

C. The ratio of polyQ free-Golgi in BFA-treated, CTR and mitotic fibroblasts. The distance of Golgi and polyQ assemblies were measured by IMARIS object-object statistics. One-way ANOVA. **, <0.01.

D. ARF1 and 3B5H10 antibody immunostaining in BFA treated fibroblasts and CTR revealed that most fragmented polyQ puncta bind to ARF1. The boxed region is the magnified region in the middle two panels.

E. The conjugation ratio of ARF1-3B5H10, Golgi-polyQ and polyQ-Golgi in BFA-treated fibroblasts. The distance of two objects were measured by IMARIS object-object statistics. One-way ANOVA. **, <0.01.

F, G. immunostaining of GM130 antibody with 3E10 or EM48 antibody revealed that polyQ assemblies contain great amount of HTTs. The middle and right panel are the sectional view boxed region (G) and the boxed region are a

magnified part or rendering part (H) (white arrows, isthmus).

H. Coimmunostaining of 3B5H10 antibody with HAP40 antibody revealed that polyQ assemblies attached by HAP40. The middle panels are sectional view and the right panel is the rendering image of middle panel by IMARIS surface.

I, J. The count of HAP40 puncta attached to polyQ assemblies with or without mHTT (I) and the ratio of HAP40 and polyQ volume (J). The distances from HAP40 puncta to polyQ assemblies and volume were measured by IMARIS. Student t-test; Data, mean ± s.e.m.

Fig. 4. PolyQ assemblies with mHTT are easier to disassemble under energy deprivation and scaffold fewer Golgi ribbons

A. 3B5H10 stained polyQ assemblies with or without mHTT under glucose starvation in the fibroblasts (CAG 19 and CAG 59) at different time points. The middle panels and inserted image are rendered tomography with IMARIS.

B, C. The size changes of polyQ assemblies with or without mHTT under glucose starvation in the fibroblasts of healthy siblings (n=2; CAG, 19) and HD patients (n=4; CAG: 59, 55, 48, and 49) at different time points. B is the sum of changes and C is the changes of each cell (Red line, HD patients; Green line, healthy). Two-way ANOVA, *<0.05.

D. The images of 3B5H10 and GM130 antibody immunostaining in the fibroblasts after 48 h glucose starvation taken by SIM microscopy. The 3D rendered tomography showed the spatial relationship of polyQ assemblies/puncta with Golgi. The boxed regions are the magnified part or rendered region.

E, F. The changes of Golgi fragments after 48 h glucose starvation in the fibroblasts of healthy siblings (two siblings, CAG 19) and HD patient (CAG 55 and CAG 49). HD/healthy ctr, the fibroblasts cultured in high glucose medium; HD/healthy starvation, the fibroblasts cultured in low glucose medium for 48h. One-way ANOVA; **, p<0.01. Cell count in each group: n>120.

G. The changes of GM130 stained Golgi sizes after 48 h glucose starvation in the fibroblasts of healthy sibling (two, CAG 19) and HD patient (CAG 55 and

CAG 49). HD/healthy ctrl, the fibroblasts cultured in high glucose medium; HD/healthy starvation, the fibroblasts cultured in low glucose medium for 48h. One-way ANOVA; **, <0.01. The number of image in cell line: n>20. Cell count in each group: n>400.

H. Image sequences of Golgi labelled by GOLGI ID Green assay kit in the living fibroblasts of healthy siblings and HD patients (CAG 59, 49 and CAG 49) after glucose starvation (The displays, the inverted channel of original image).

I. The fragmentation ratio of Golgi under glucose starvation at different time points in healthy and HD fibroblasts. Fragmentation ratio = number of Golgi of a cell in each time point/ number of Golgi at 0 min. Two-way ANOVA. *, <0.05; **, <0.01. The number of images in cell line: n>5.

Fig. 5. HTTs present on the ruffling membrane of fibroblasts

A. HTT C-terminal antibody and polyQ antibody immunostaining revealed that C-terminal antibody signals colocalize with cytoplasmic polyQ assemblies. A queue of HTTs labeled by C-terminal antibody and polyQ antibody present on the ruffling membrane. The middle panel is an angled view of 3D images. The two right panels are the enlarged image of the boxed region in the left panel (cytoplasmic polyQ) (white arrows, the ruffling membrane).

B, C. HTT C-terminal antibody and 3B5H10 antibody and phalloidin immunostaining revealed that HTTs uniformly distribute on membrane curvature and endocytic vacuoles. Boxed region, the region of sectional views (i, ii). The image of sectional views or angled view showed the orientation and the spatial relationships.

D. HTT C-terminal antibody and 3B5H10 antibody and phalloidin immunostaining showed that large endocytic vacuoles attached by enriched actin bundle express HTTs. The right panel in i is the sectional view of boxed part. The inner panels in ii are the spliced channel of vacuole indicated by yellow arrow (white arrows, polyQ and F-actin conjugation in the lateral view; yellow arrows, large vacuoles).

E. HTT^+ Large endocytic vacuoles attached by enriched actin bundle

approximate polyQ assemblies and merge with polyQ assemblies (the boxed region indicated the enlarged sectional view in middle panel; white arrows, the vacuole merged with polyQ assemblies).

F. The scheme of the spatial relationships HTT (mHTT) and F-actin on ruffling membrane and vacuole membrane.

G. The count of HTT^+ vacuoles in HD and healthy fibroblasts (CAG 59, 49 vs CAG19 and 19). Figure count: n= 21. Data. Mean ± SD.

Fig. 6. The characteristics of polyQ assembly with or without mHTT in the induced GABAergic neutrons

A. Poly Q assemblies stained by 3B5H10 antibody in iPS -derived striatal neurons at day 40.

B. The characteristics of polyQ assembly in iPS -derived GABAergic neurons at day 90 and 120 (i, the nucleus without nuclear accumulation; ii, the nucleus with nuclear polyQ accumulation). The 3D rendered tomography revealed the spatial relationship of polyQ assemblies with the nucleus.

C. Time-dependent changes of polyQ assemblies in iPSCs-derived GABAergic neurons (HD, CAG: 59, 55, 49 and 47; Healthy, CAG 19, CAG 19 and H9). Data, means± SD.

D. PolyQ assemblies volume in iPS-derived GABAergic neuronal nucleus cultured over 90 days (CAG: 59, 55 and 49; n=134; N, CAG, 19 and H9; n=56). *t*-test; **, $p < 0.01$. Data, means ± s.e.m.

E. PolyQ assemblies stained by 3B5H10 antibody in fresh surgical brain tissues collected from a 4-year-old glioblastoma patient. Three representative appearance of polyQ assemblies in human brain cells. The middle panel is image-i is a sectional view that shows a ring-like structure; the left corner insert in image-ii is a larger view; the rendered tomography shows the nuclear surface.

F. DIC images and 3D rendered tomography showing longer polyQ assemblies form a gorge in the cytoplasm or nuclear surface of induced neurons cultured for 75 days (CAG 59 and CAG 19) (pink arrow [i, ii], the gorges; white arrow,

nuclear surface dents visualized by IMARIS surface). Inner panels, and 3D rendered tomography displayed the spatial relationships.

Fig. 7. PolyQ assemblies with mHTT scaffolded or attached fewer Golgi or clathrin + vesicles than polyQ assemblies without mHTT in neurons

A. The validation of hCO by immunostaining with PAX6/TBR2 /HOPX or TBR1/CTIP2/SATB2 antibodies.

B. The validation of hCO and hStrOs by immunostaining with GSH2/MASH1 or DARPP321/CTIP2 antibodies.

C. The representative images of polyQ assemblies with or without mHTT and Golgi stained by 3B5H10 and GM130 antibodies in hStrO (taken by SIM microscopy; Z-stack interval, 0.2 μm). Middle panels are a sectional view. The lower panels are 3D rendering tomography by Imaris 9.8 surface.

D. Comparing the overlapped volume of Golgi with polyQ assemblies with and without mHTT. The overlapped volume is measured by the object-object statistic function in IMARIS. Student *t*-test; **, $p < 0.01$. N, healthy.

E. The representative images of polyQ assemblies with or without mHTT and Golgi stained by 3B5H10 and GM130 antibodies in hCO (Taken by SIM microscopy; Z-stack interval, 0.2μm). The right two panels (i) are the rendered tomography by IMARIS surface; ii are the rendered tomography that revealed the spatial relationship of Golgi with polyQ assemblies (white arrows, the deformed Golgi with convoluted morphology).

F. The images of polyQ assemblies with mHTT (CAG 59) and polyQ assemblies stained by 3B5H10 and clathrin antibodies in in hCO were taken by SIM microscopy (The upper panel, the lateral view of boxed region; the inner insert in the rendered image, larger view of original image). The renderings are done by Imaris Surface.

G. Counting clathrin$^+$ vesicles conjugated with or close (the distance of clathrin$^+$ vesicles to polyQ assemblies <0.1μm) to polyQ assemblies with or without mHTT in hStrO (i). student *t*-test; *, $p < 0.05$. N, healthy. Comparing clathrin+ vesicle volume overlapped with 3B5H10 stained polyQ assemblies in

the healthy sibling with HD patient (ii). Student *t*-test; *, p <0.05

H. Long polyQ assemblies with mHTT reside in the projections of GABAergic neurons cultured for 98 days and two extended polyQ assemblies with mHTT assemblies paralleled in one projection. GABAergic neurons with longer polyQ assemblies with mHTT have normal nuclear morphology (Boxed images, nucleus; taken by Zeiss 880 microscopy; the estimated resolution is 140 nm).

I. Eminent longer polyQ assemblies stained by 3B5H10 antibody in human surgical brain cortex (a 2-year-old glioblastoma patient; taken by Zeiss 880 microscopy; the estimated resolution is 140 nm).

J. PolyQ assemblies with mHTT in the distal projections of GABAergic neurons are assembled by multiple ring-like structure (white arrows, rings). 3D rendering images showed that polyQ deposited in the nucleus pokes the neuronal membrane (yellow arrow, nuclear poking). The right (lower) and right panels showed that the longer assemblies in the distal parts of neuronal projections stained by 3B5H10 antibody in human brain tissues were assembled by apparent multiple ring-like structure connected at the edge . Images were taken by SIM microscopy with Z-stack. The estimated resolution in x-y is 63 nm.

K. 3B5H10 and GM130 antibodies immunostaining images of eminent long polyQ assemblies and 3D rendered tomography in the neurons of hStrO of HD patients and healthy siblings.

L. Comparing GM130 stained Golgi volume overlapped with eminent long polyQ assemblies with mHTT and without mHTT in hStrO. Object-object statistics in IMARIS measures the overlapped volume. *t*-test, *, p<0.05. HD hStrO: CAG 55 and CAG 47; Healthy hStrO: H9, CAG 19.

M. Comparing the number of GM130 stained small Golgi attach or close to (the distance <0.1μm) eminent long polyQ assemblies with mHTT with that of healthy polyQ assemblies in hStrO. Object-object statistics in IMARIS measured the distances. HD hStrO: CAG 55 and CAG 47; Healthy hStrO: H9, CAG 19. Student *t*-test, *, p<0.05.

N. 3B5H10 and GM130 antibodies immunostaining images and their sectional views in the neurons of hStrO of HD patients and healthy siblings revealed the spatial relationships between polyQ assemblies and Golgi (white arrows, the Golgi in the inner hole of the ring; pink arrows, the scaffolding Golgi; the boxed region, the right or left panel).

O. 3B5H10 and clathrin antibodies staining images of the neurons in hStrO of HD patients and healthy siblings revealed the spatial relationships between polyQ assemblies and clathrin stained vesicles. The left panel is a sectional view between two arrows (hStrO at day 80; two white arrows, the segment in the right panel)

Fig. 8. GABAergic neurons from HD patients reduced Golgi- or vesicle-related activities and intensified nucleus-related activities

A, B. Uniform manifold approximation and projection (UMAP) plot of all cells colored by their sample origin (A) and by cell types (B).

C. Dot plot displaying an expression of example marker genes.

D. Venn diagram summarizing the number of overlapped genes differentially expressed in CAG59 vs. CAG19/H9 GABAergic neurons.

E. GO enrichment analysis of down-regulated (top) and up-regulated (bottom) genes in CAG59 vs. CAG19/H9 GABAergic neurons.

F. The immunostaining results of ARF1, CTIP2, and 3B5H10 antibodies in the neurons of hStrOs (CAG 49 and CAG 19). The middle panels showed ARF1 signals.

G, H. The overlapped volume of ARF1 with polyQ in the HD and healthy neurons of hStrOs (G). The ratio of ARF1 volume/polyQ volume in CTIP2 + regions. The surface function of IMARIS was used to calibrate volume. Object-object statistics in IMARIS measure the overlapped volume. t-test, *, $p<0.05$; **, $p<0.01$..

I. The immunostaining results of ARF1, CTIP2, and GM130 antibodies in the neurons of hStrOs (CAG 49 and CAG 19). The middle panels showed ARF1 signals.

J, K, The overlapped volume of ARF1 with Golgi in the HD and healthy neurons of hStrOs. The ratio of ARF1 volume/Golgi volume in CTIP2 + regions. The surface function of IMARIS were used to calibrate volume. Object-object statistics in IMARIS measures the overlapped volume. t-test, **, $p<0.01$.

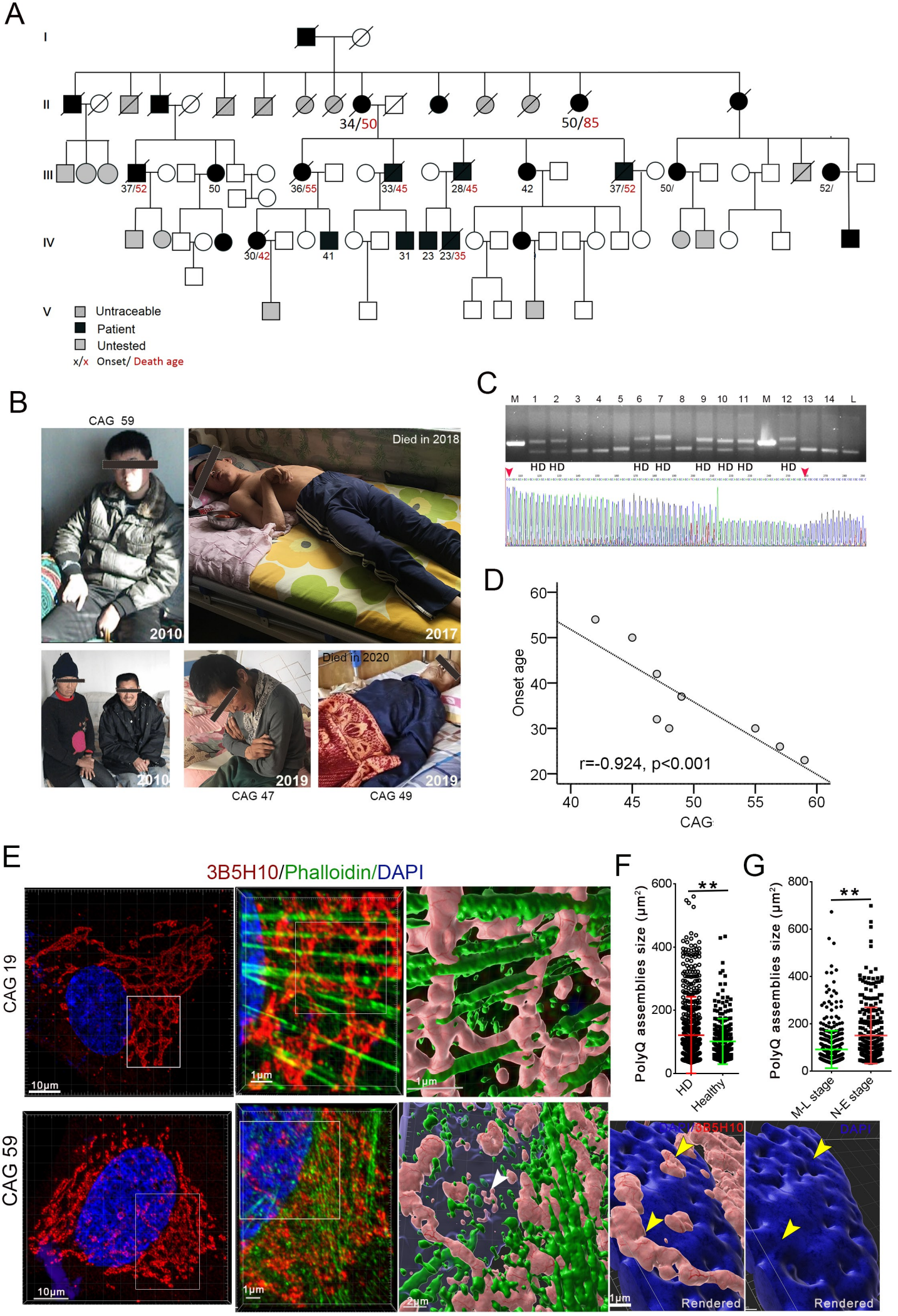
A
I
II
III
IV
V
34/50
50/85
37/52
50
36/55
33/45
28/45
42
37/52
50/
52/
30/42
41
31
23
23/35
Untraceable
Patient
Untested
x/x Onset/ Death age
B
CAG 59
Died in 2018
2010
2017
2010
2019
Died in 2020
2019
CAG 47
CAG 49
C
M 1 2 3 4 5 6 7 8 9 10 11 M 12 13 14 L
HD HD
HD HD
HD HD HD
HD
D
Onset age
CAG
r=-0.924, p<0.001
E
3B5H10/Phalloidin/DAPI
CAG 19
CAG 59
10μm
1μm
2μm
F
PolyQ assemblies size (μm²)
HD
Healthy
G
PolyQ assemblies size (μm²)
M-L stage
N-E stage
3B5H10
DAPI
Rendered

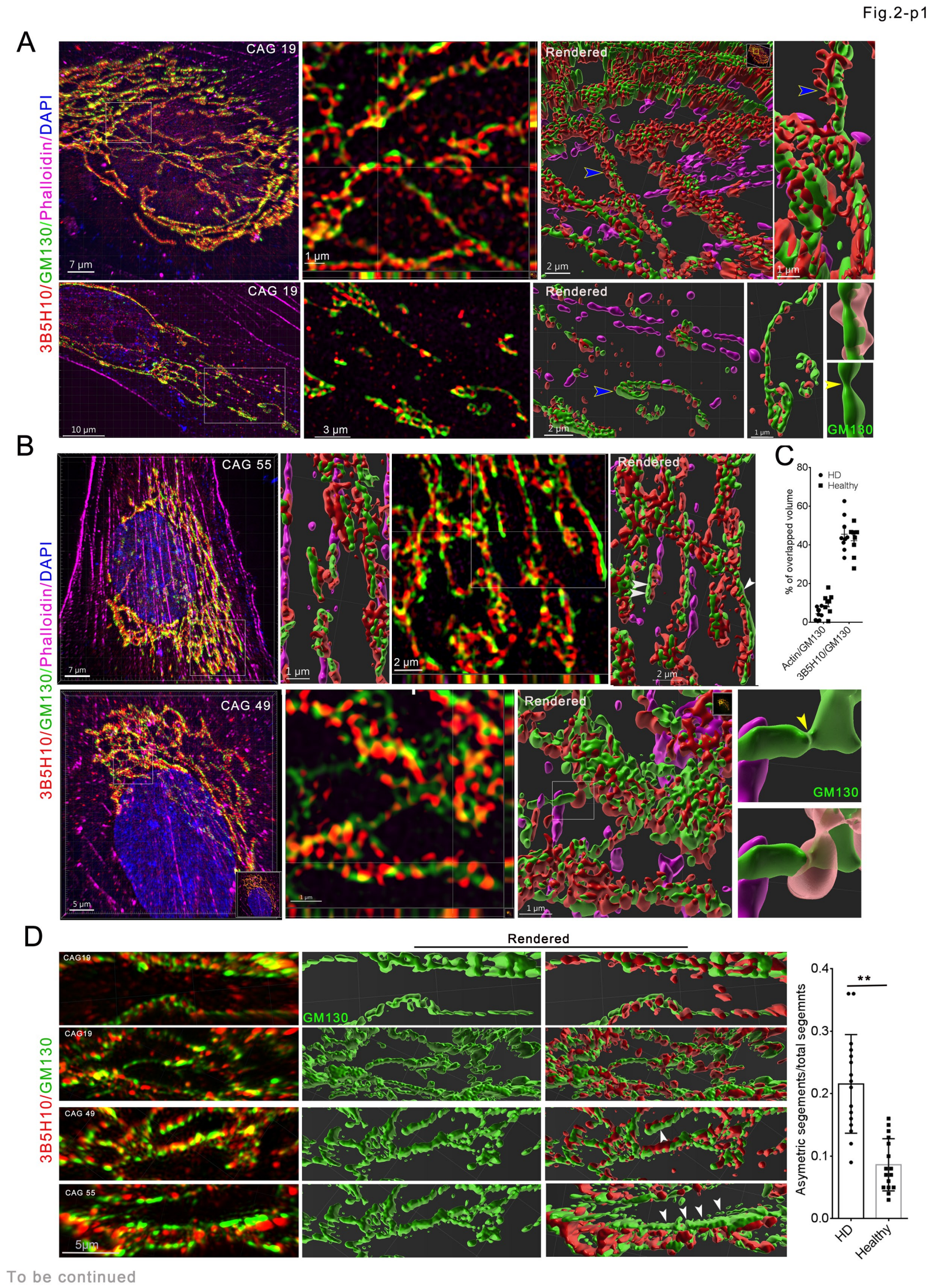

To be continued

E

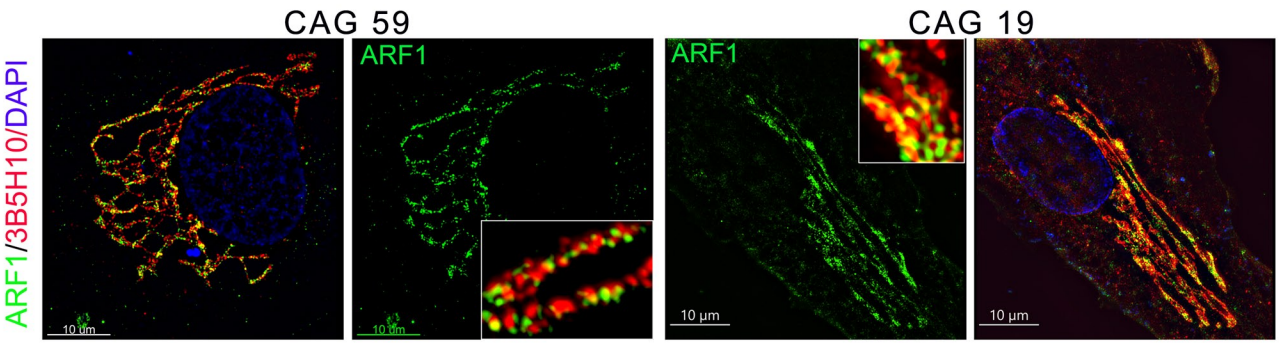
CAG 59
CAG 19
ARF1/3B5H10/DAPI
ARF1
ARF1
10 µm
10 µm
10 µm
10 µm

F

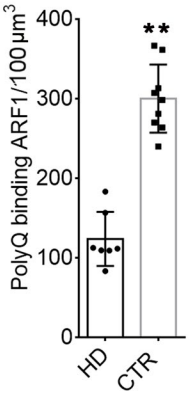
PolyQ binding ARF1/100 µm3
400
300
200
100
0
**
HD
CTR

G

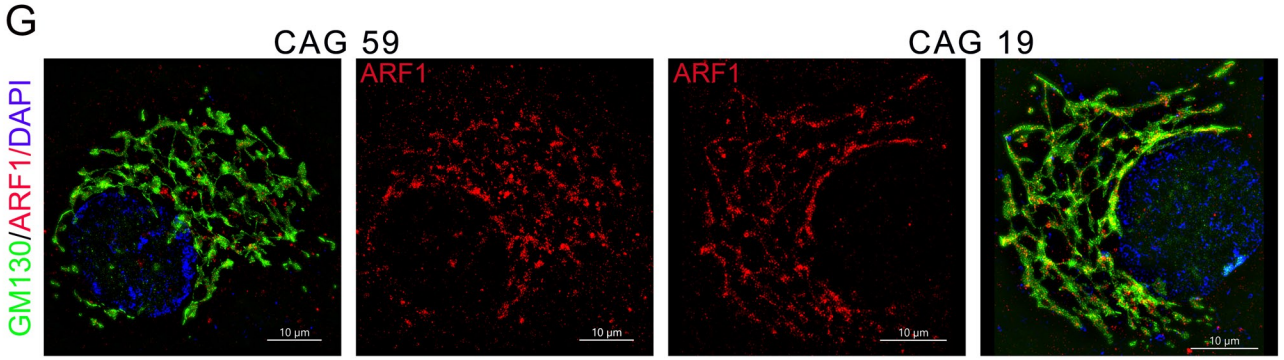
CAG 59
CAG 19
GM130/ARF1/DAPI
ARF1
ARF1
10 µm
10 µm
10 µm
10 µm

H

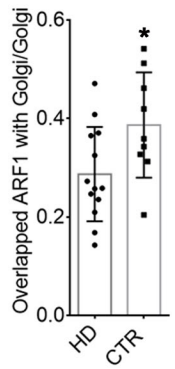
Overlapped ARF1 with Golgi/Golgi
0.6
0.4
0.2
0.0
*
HD
CTR

I

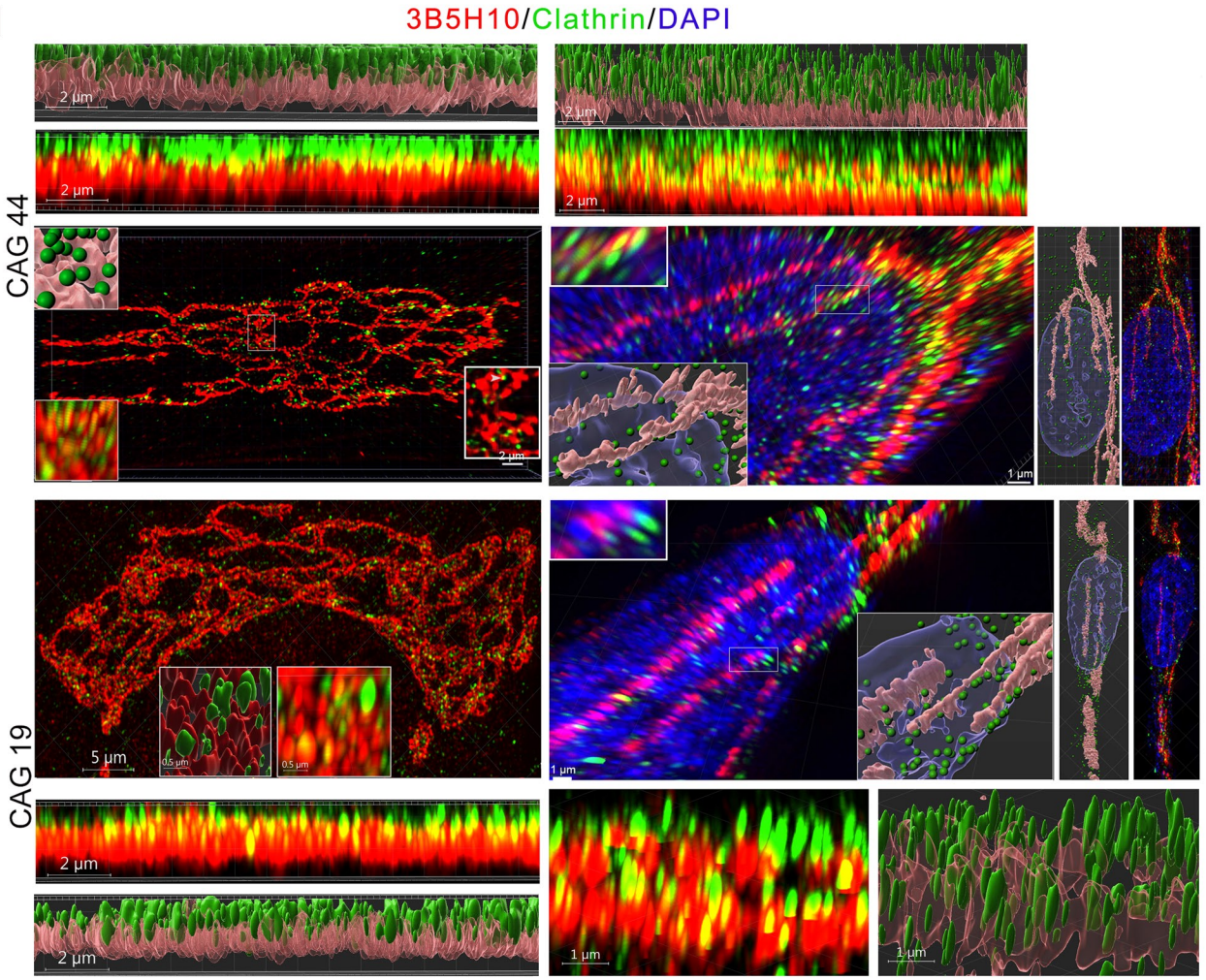
3B5H10/Clathrin/DAPI
CAG 44
CAG 19
2 µm
2 µm
2 µm
2 µm
2 µm
1 µm
5 µm
0.5 µm
0.5 µm
1 µm
2 µm
2 µm
1 µm
1 µm

K

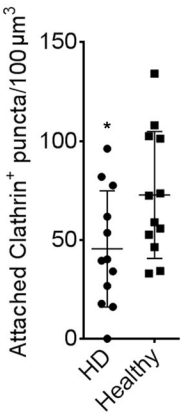
Attached Clathrin+ puncta/100 µm3
150
100
50
0
*
HD
Healthy

L

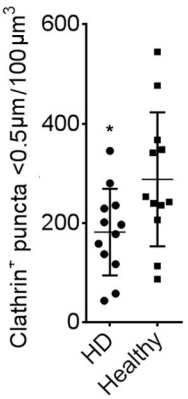
Clathrin+ puncta <0.5µm/100 µm3
600
400
200
0
*
HD
Healthy

J

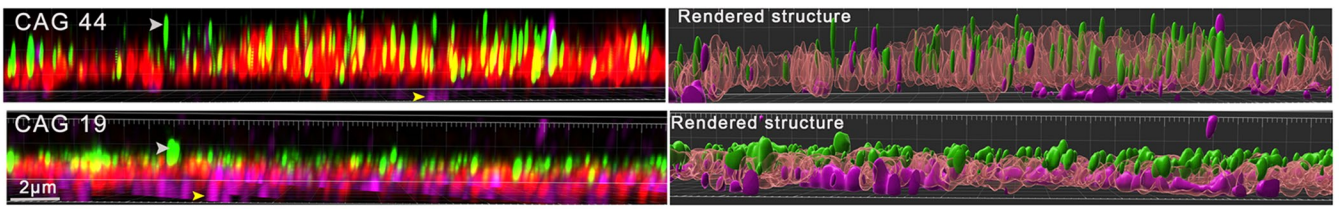
3B5H10/Clathrin/PhalloidinDAPI
CAG 44
Rendered structure
CAG 19
Rendered structure
2µm

Fig. 3

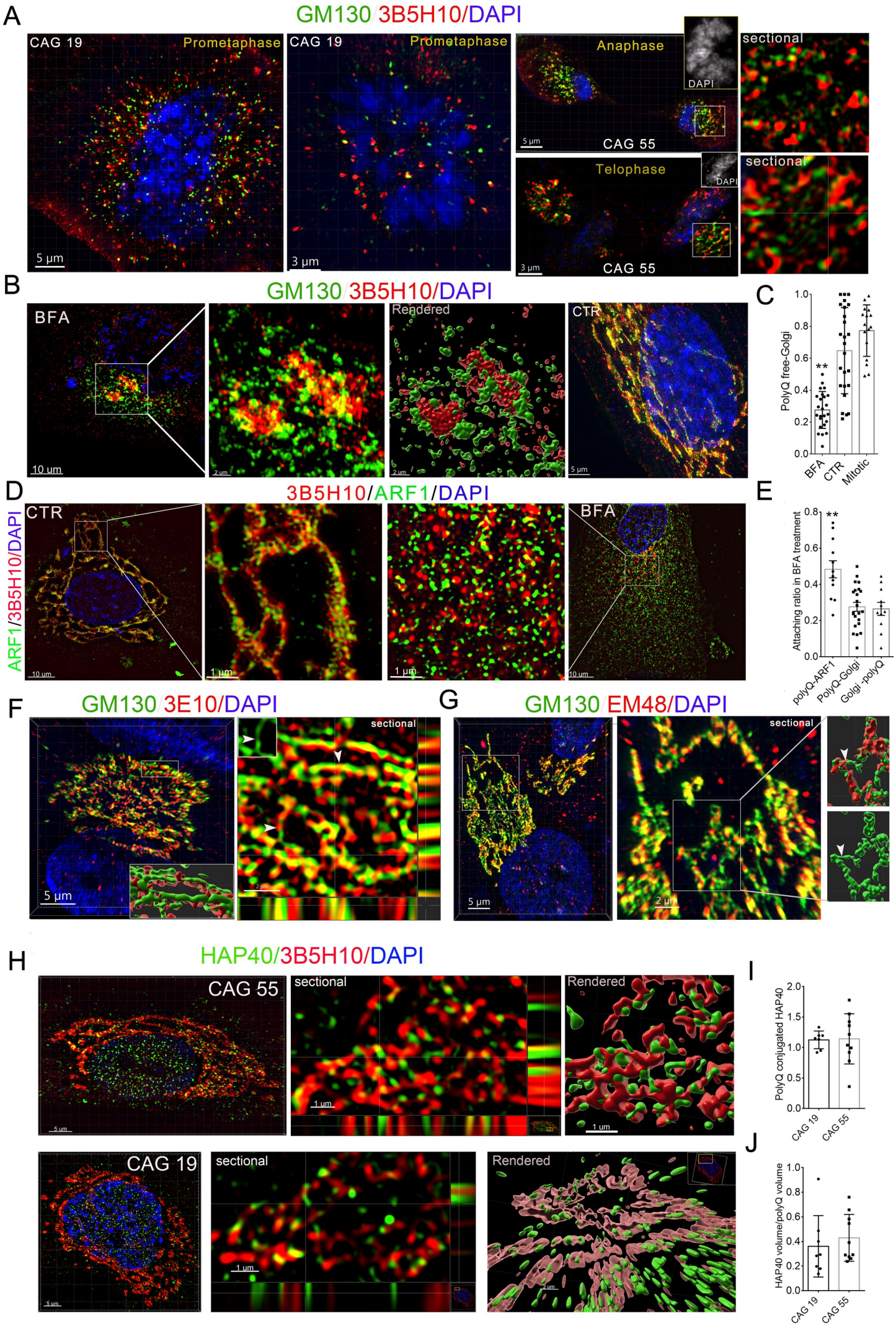
A
GM130 3B5H10/DAPI
CAG 19
Prometaphase
5 µm
CAG 19
Prometaphase
3 µm
Anaphase
DAPI
5 µm
CAG 55
sectional
Telophase
DAPI
3 µm
CAG 55
sectional
B
GM130 3B5H10/DAPI
BFA
10 um
2 um
Rendered
2 um
CTR
5 µm
C
PolyQ free-Golgi
1.0
0.8
0.6
0.4
0.2
0.0
**
BFA
CTR
Mitotic
D
3B5H10/ARF1/DAPI
ARF1/3B5H10/DAPI
CTR
10 um
1 µm
1 µm
BFA
10 um
E
Attaching ratio in BFA treatment
0.8
0.6
0.4
0.2
0.0
**
polyQ-ARF1
PolyQ-Golgi
Golgi -polyQ
F
GM130 3E10/DAPI
5 µm
sectional
2 µm
G
GM130 EM48/DAPI
5 µm
sectional
2 µm
H
HAP40/3B5H10/DAPI
CAG 55
5 um
sectional
1 um
Rendered
1 um
CAG 19
5 um
sectional
1 um
Rendered
2 um
I
PolyQ conjugated HAP40
2.0
1.5
1.0
0.5
0.0
CAG 19
CAG 55
J
HAP40 volume/polyQ volume
1.0
0.8
0.6
0.4
0.2
0.0
CAG 19
CAG 55

Fig. 4

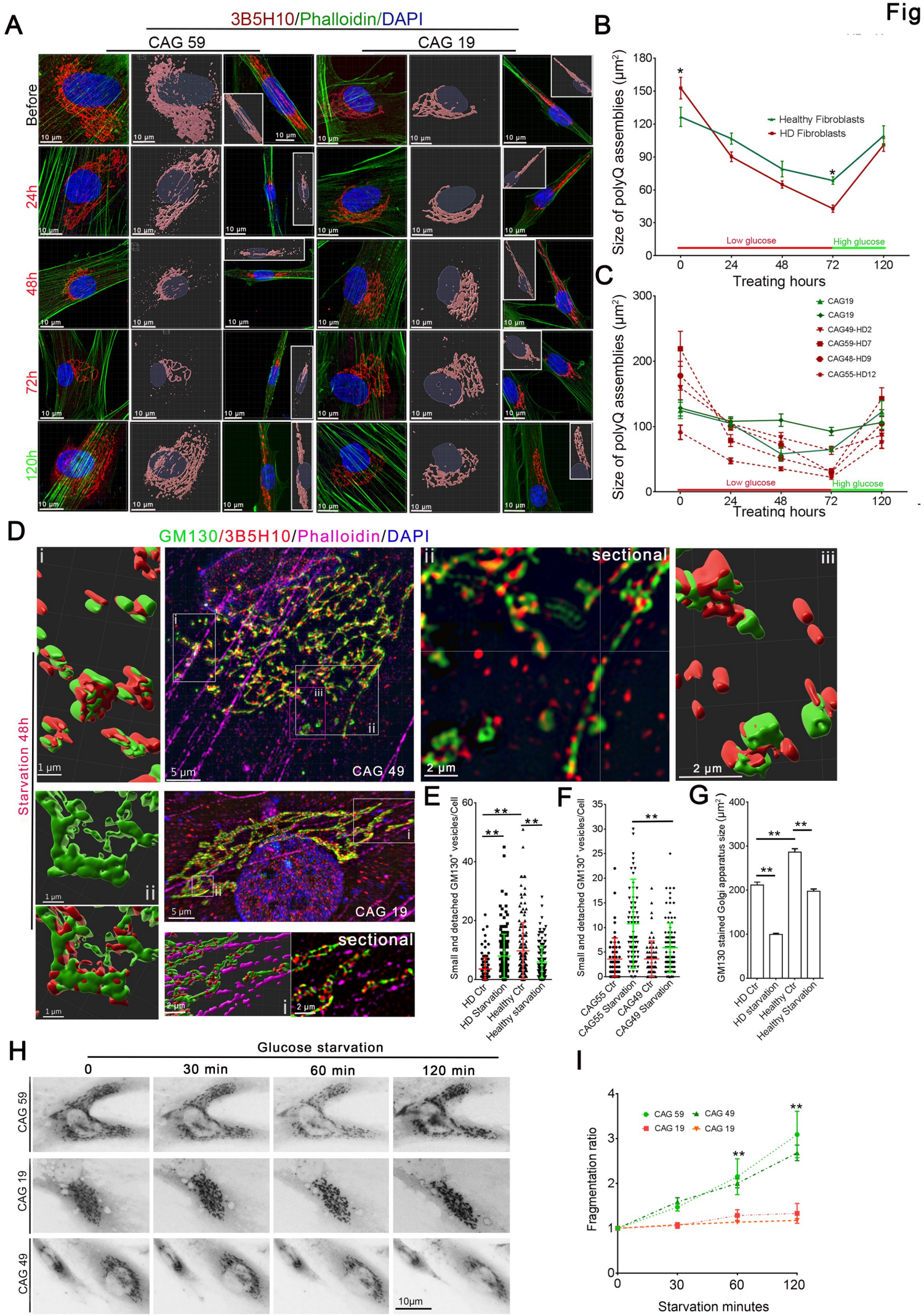
A
3B5H10/Phalloidin/DAPI
CAG 59
CAG 19
Before
24h
48h
72h
120h
10 µm
B
Size of polyQ assemblies (µm²)
Healthy Fibroblasts
HD Fibroblasts
Low glucose
High glucose
Treating hours
C
CAG19
CAG19
CAG49-HD2
CAG59-HD7
CAG48-HD9
CAG55-HD12
D
GM130/3B5H10/Phalloidin/DAPI
Starvation 48h
1 µm
5 µm
CAG 49
CAG 19
sectional
2 µm
E
Small and detached GM130⁺ vesicles/Cell
HD Ctr
HD Starvation
Healthy Ctr
Healthy starvation
F
CAG55 Ctr
CAG55 Starvation
CAG49 Ctr
CAG49 Starvation
G
GM130 stained Golgi apparatus size (µm²)
HD Ctr
HD starvation
Healthy Ctr
Healthy Starvation
H
Glucose starvation
0
30 min
60 min
120 min
CAG 59
CAG 19
CAG 49
10µm
I
CAG 59
CAG 49
CAG 19
CAG 19
Fragmentation ratio
Starvation minutes

Fig.5

A

Phalloidin/3B5H10/LSB11011/DAPI

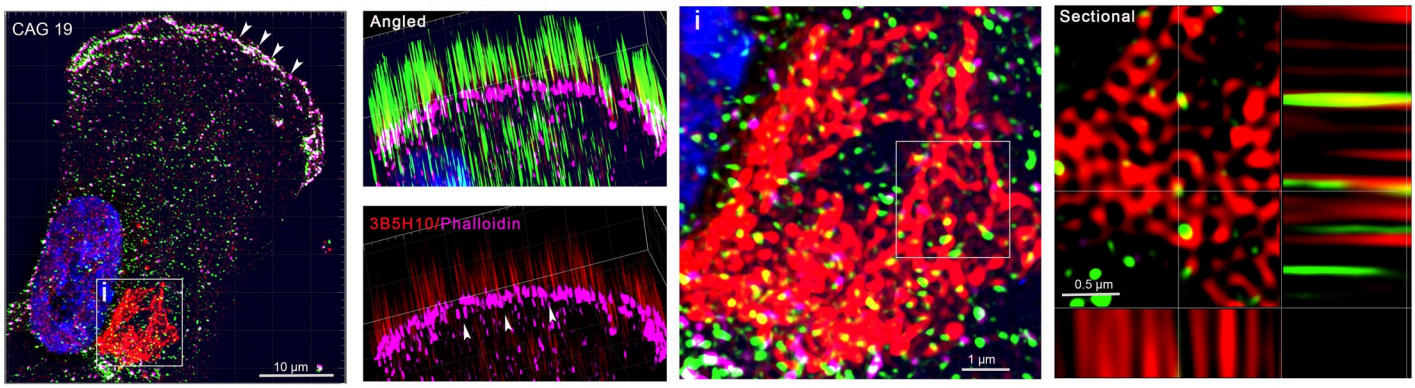

B

Phalloidin/3B5H10/LSB11011/DAPI

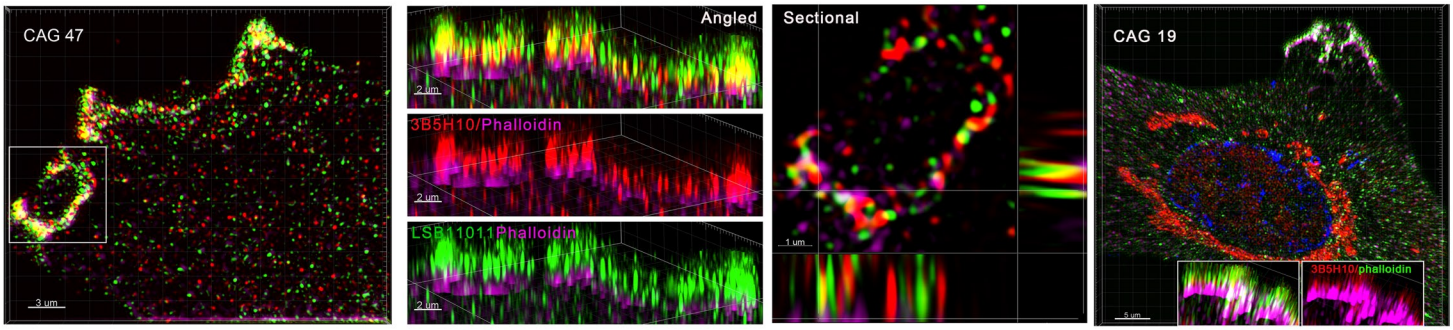

C

Phalloidin/3B5H10/LSB11011/DAPI

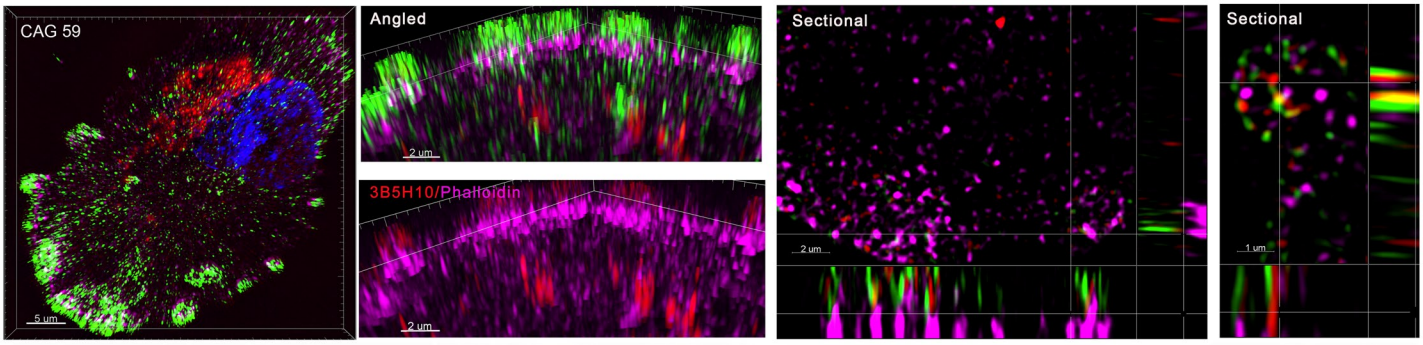

D

Phalloidin/3B5H10/LSB11011/DAPI

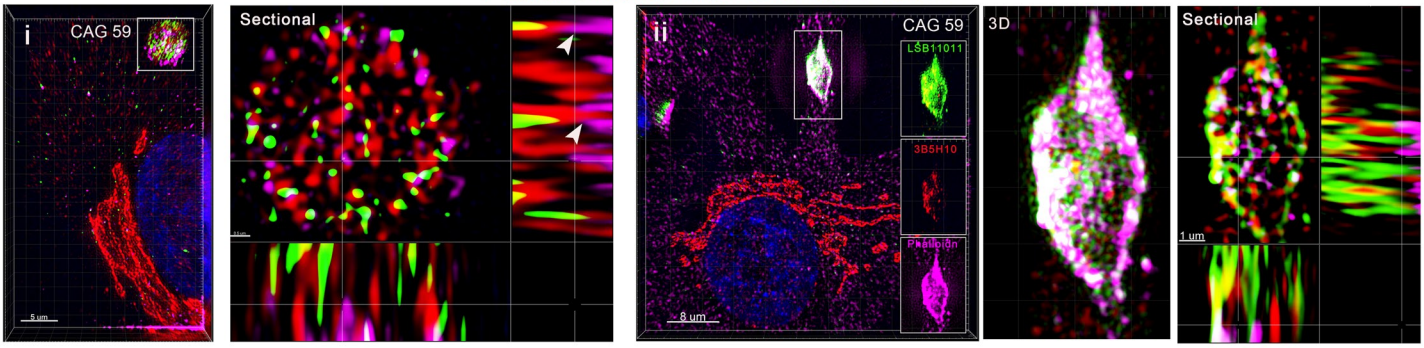

E

Phalloidin/3B5H10/LSB11011/DAPI

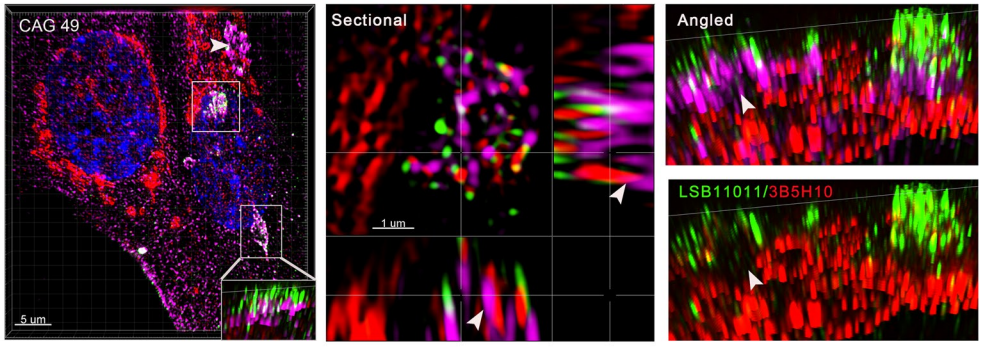

F

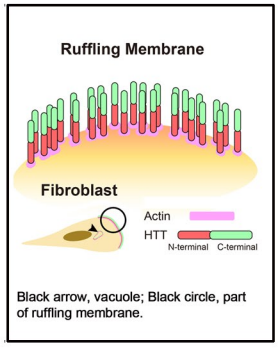

G

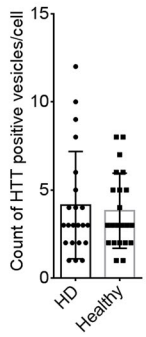

Fig.6

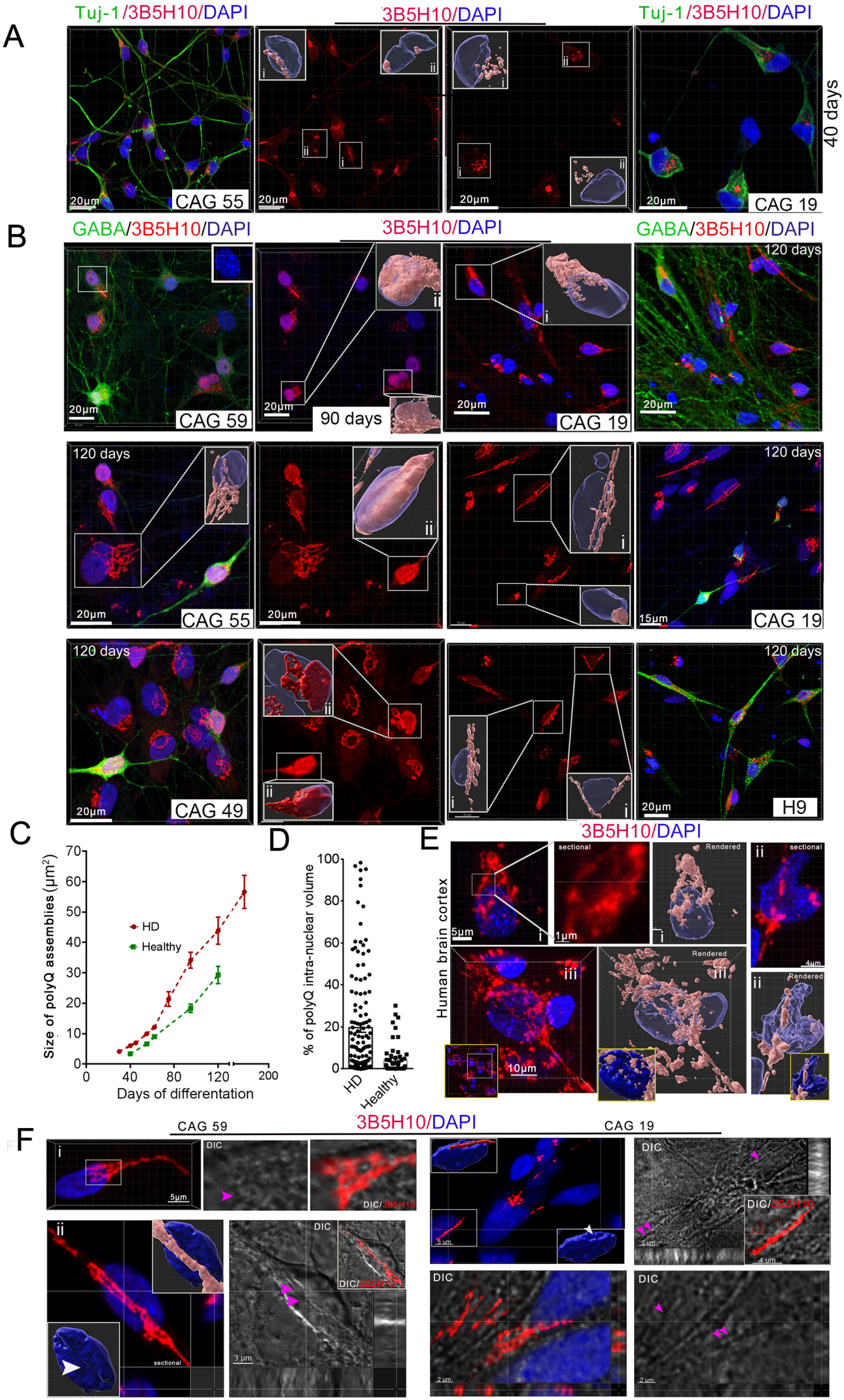
A
Tuj-1/3B5H10/DAPI
3B5H10/DAPI
Tuj-1/3B5H10/DAPI
40 days
20μm
CAG 55
CAG 19
B
GABA/3B5H10/DAPI
3B5H10/DAPI
GABA/3B5H10/DAPI
120 days
CAG 59
90 days
CAG 19
CAG 55
CAG 19
CAG 49
H9
C
Size of polyQ assemblies (μm²)
Days of differentation
HD
Healthy
D
% of polyQ intra-nuclear volume
HD
Healthy
E
3B5H10/DAPI
Human brain cortex
sectional
Rendered
5μm
1μm
10μm
4μm
F
CAG 59
3B5H10/DAPI
CAG 19
DIC
DIC/3B5H10
5μm
3 μm
4 μm
2 μm
sectional

A

human Cortical Organoids

PAX6/TBR2/HOPX/DAPI

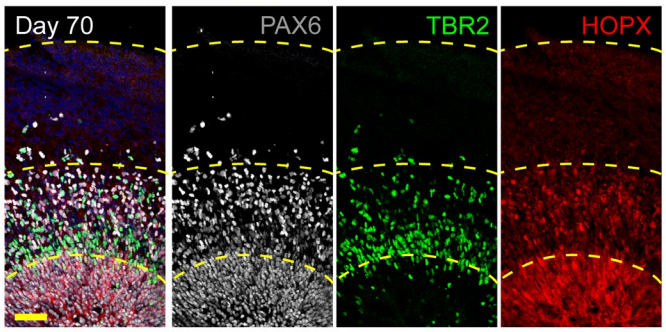

TBR1/CTIP2/SATB2/DAPI

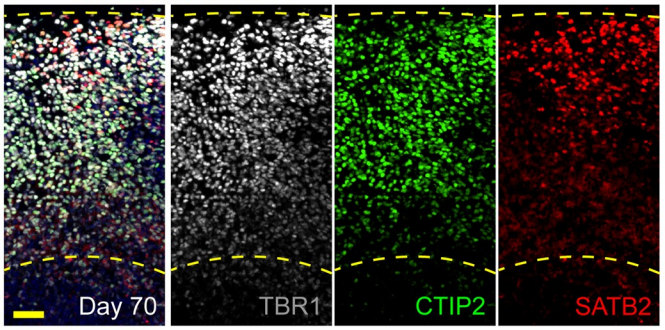

B

human Striatal Organoids

GSH2/MASH1/DAPI

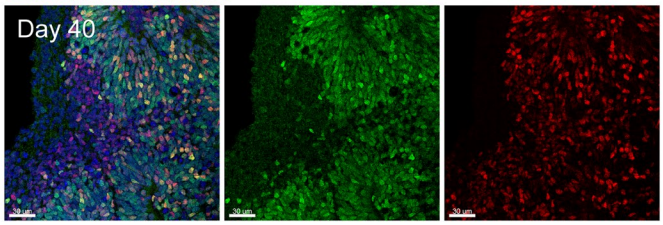

DARPP32/CTIP2/DAPI

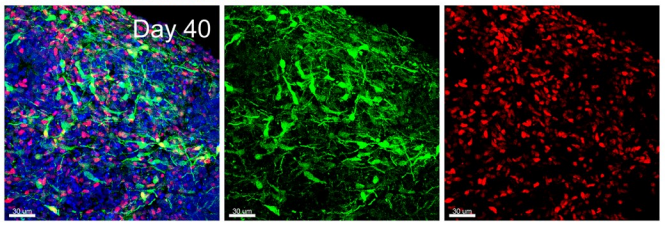

C

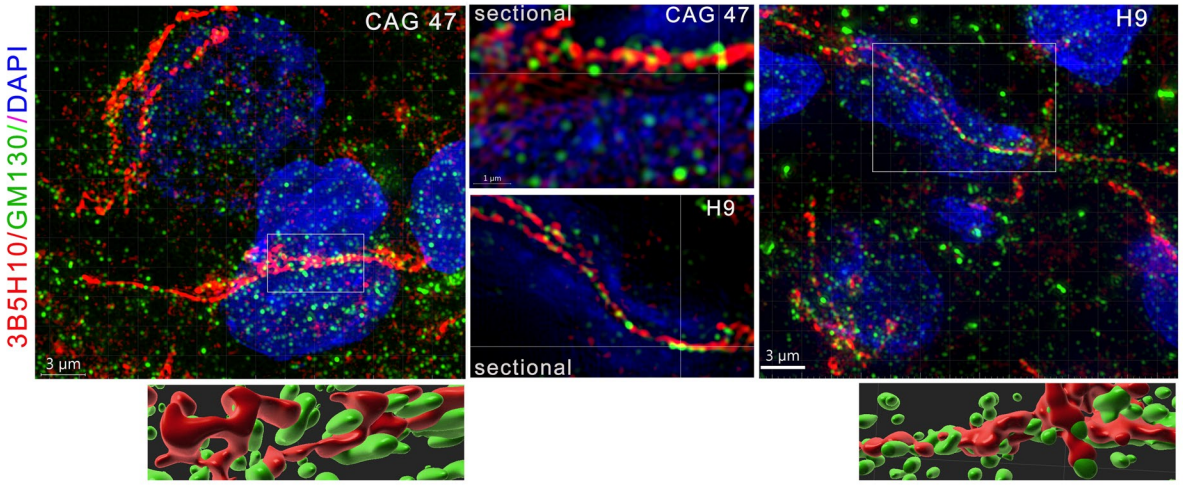

D

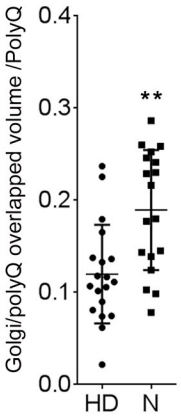

E

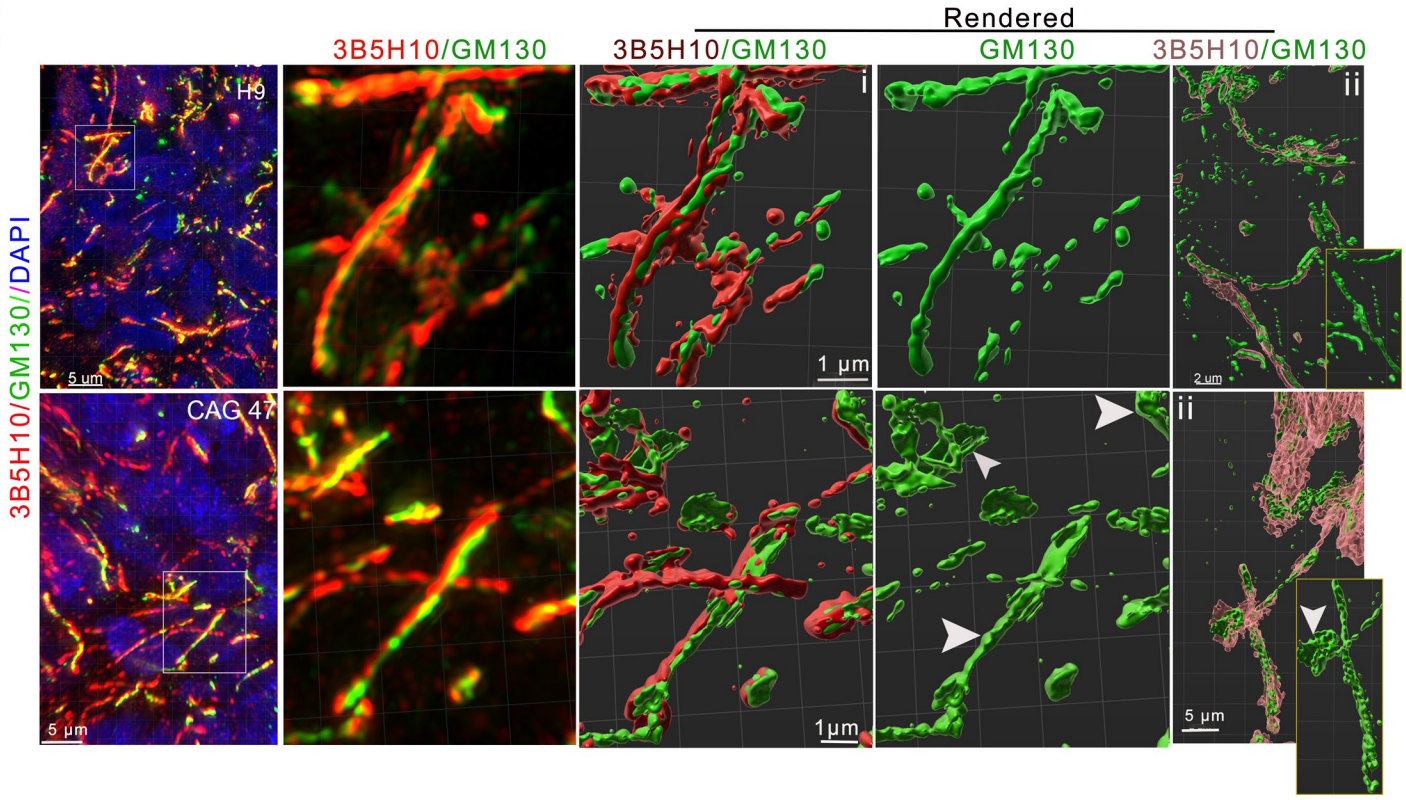

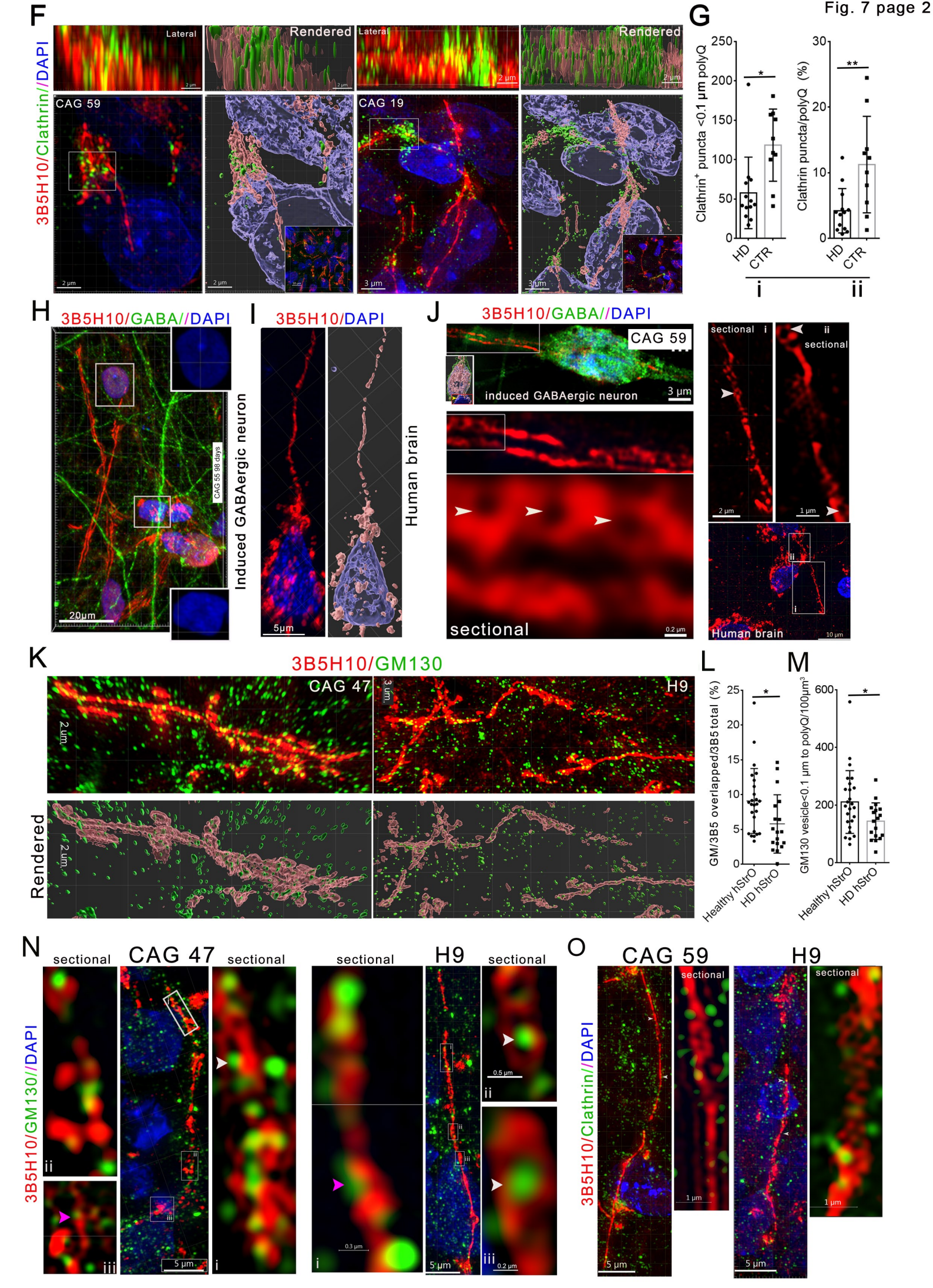
F
Lateral
Rendered
Lateral
Rendered
3B5H10/Clathrin//DAPI
CAG 59
CAG 19
2 µm
3 µm
G
Clathrin+ puncta <0.1 µm polyQ
Clathrin puncta/polyQ (%)
HD
CTR
i
ii
H
3B5H10/GABA//DAPI
Induced GABAergic neuron
CAG 55 98 days
20µm
I
3B5H10/DAPI
Human brain
5µm
J
3B5H10/GABA//DAPI
CAG 59
induced GABAergic neuron
3 µm
sectional
0.2 µm
sectional i
ii sectional
2 µm
1 µm
Human brain
10 µm
K
3B5H10/GM130
CAG 47
H9
Rendered
2 µm
3 µm
L
GM/3B5 overlapped/3B5 total (%)
Healthy hStrO
HD hStrO
M
GM130 vesicle<0.1 µm to polyQ/100µm³
N
sectional
CAG 47
H9
3B5H10/GM130//DAPI
5 µm
0.3 µm
0.5 µm
0.2 µm
O
CAG 59
H9
3B5H10/Clathrin//DAPI
1 µm
5 µm

Fig. 8

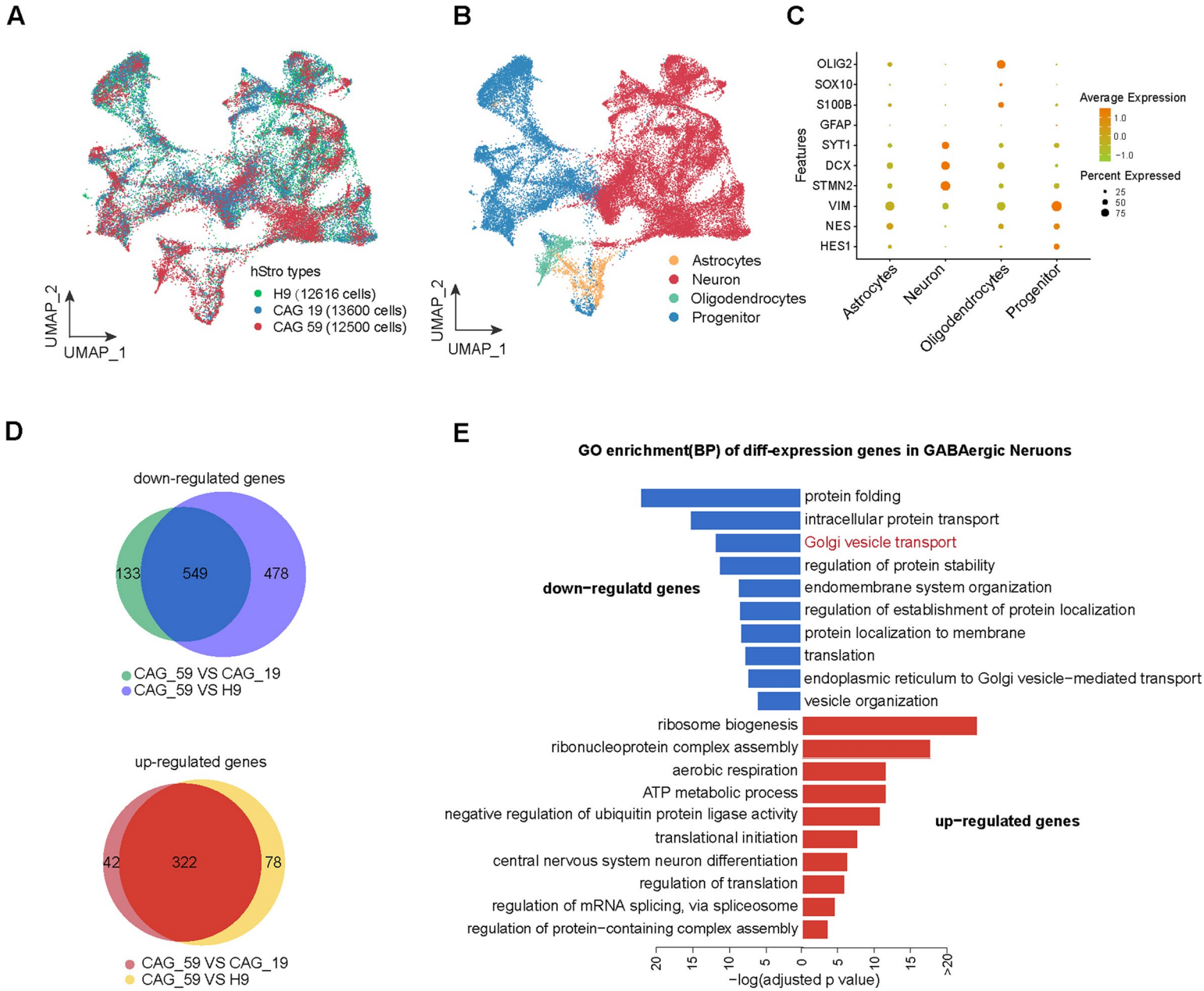
A
hStro types
H9 (12616 cells)
CAG 19 (13600 cells)
CAG 59 (12500 cells)
UMAP_2
UMAP_1
B
Astrocytes
Neuron
Oligodendrocytes
Progenitor
UMAP_2
UMAP_1
C
Features
OLIG2
SOX10
S100B
GFAP
SYT1
DCX
STMN2
VIM
NES
HES1
Astrocytes
Neuron
Oligodendrocytes
Progenitor
Average Expression
Percent Expressed
D
down-regulated genes
133
549
478
CAG_59 VS CAG_19
CAG_59 VS H9
up-regulated genes
42
322
78
CAG_59 VS CAG_19
CAG_59 VS H9
E
GO enrichment(BP) of diff-expression genes in GABAergic Neruons
down−regulatd genes
protein folding
intracellular protein transport
Golgi vesicle transport
regulation of protein stability
endomembrane system organization
regulation of establishment of protein localization
protein localization to membrane
translation
endoplasmic reticulum to Golgi vesicle−mediated transport
vesicle organization
up−regulated genes
ribosome biogenesis
ribonucleoprotein complex assembly
aerobic respiration
ATP metabolic process
negative regulation of ubiquitin protein ligase activity
translational initiation
central nervous system neuron differentiation
regulation of translation
regulation of mRNA splicing, via spliceosome
regulation of protein−containing complex assembly
−log(adjusted p value)
F
CAG 49
3B5H10/ARF1/CTIP2
ARF1
CAG 19
ARF1
3B5H10/ARF1/CTIP2
10 μm
G
Overlapped ARF1 /polyQ volume
HD
CTR
H
ARF1 volume/polyQ volume
HD
CTR
I
CAG 49
ARF1/GM130/CTIP2
ARF1
CAG 19
ARF1
ARF1/GM130/CTIP2
10 μm
J
Overlapped ARF1 /Golgi volume
HD
CTR
K
ARF1 volume/Golgi volume
HD
CTR

S-table-1. The baseline characteritics of HD family members

No	Gender	Age	F	Onset age	CAG (mutant)	CAG (wild)	Syndrome (on sampling age)	Death	Sampling year
1	F	46	F3	42	47	19	moderate		2010
2	M	44	F3	37	49	19	moderate	54	2010
3	M	21	F4			19			2010
4	F	28	F4			19			2010
5	F	26	F4			19			2010
6	M	23	F4	26	57	19	mild		2010
7	M	27	F4	23	59	19	mild	36	2010
8	F	19	F4			19			2010
9	M	28	F4	30	48	19	mild		2010
10	F	26	F4	32	47	19	no syndrome		2010
11	M	5	F5		45	18	no syndrome		2010
12	F	39	F4	30	55	19	critical	42	2010
13	F	42	F4			19			2010
14	F	23	F4			19			2010
15	M	44	F4	41	NA		critical		2010
16	M	17	F5		NA				2010
17	M	33	F4			19			2017
18	F	30	F3		45	19	no syndrome		2017
19	F	52	F4		45	19	moderate		2017
20	F	25	F3			19			2017
21	M	21	F3			19			2017
22	M	52	F2		NA		died without syndrome		2019
23	M	30	F4		44	19	no syndrome		2019
24	F	54	F3		42	19	moderate		2019
25	F	56	F3		NA		critical		2020
26	M	52	F3		NA		healthy		2020
27	F	28	F4		NA		healthy		2020
28	M	32	F4		NA		healthy		2020

F, female; M,male; NA, non-assessed; F1-4 genereation

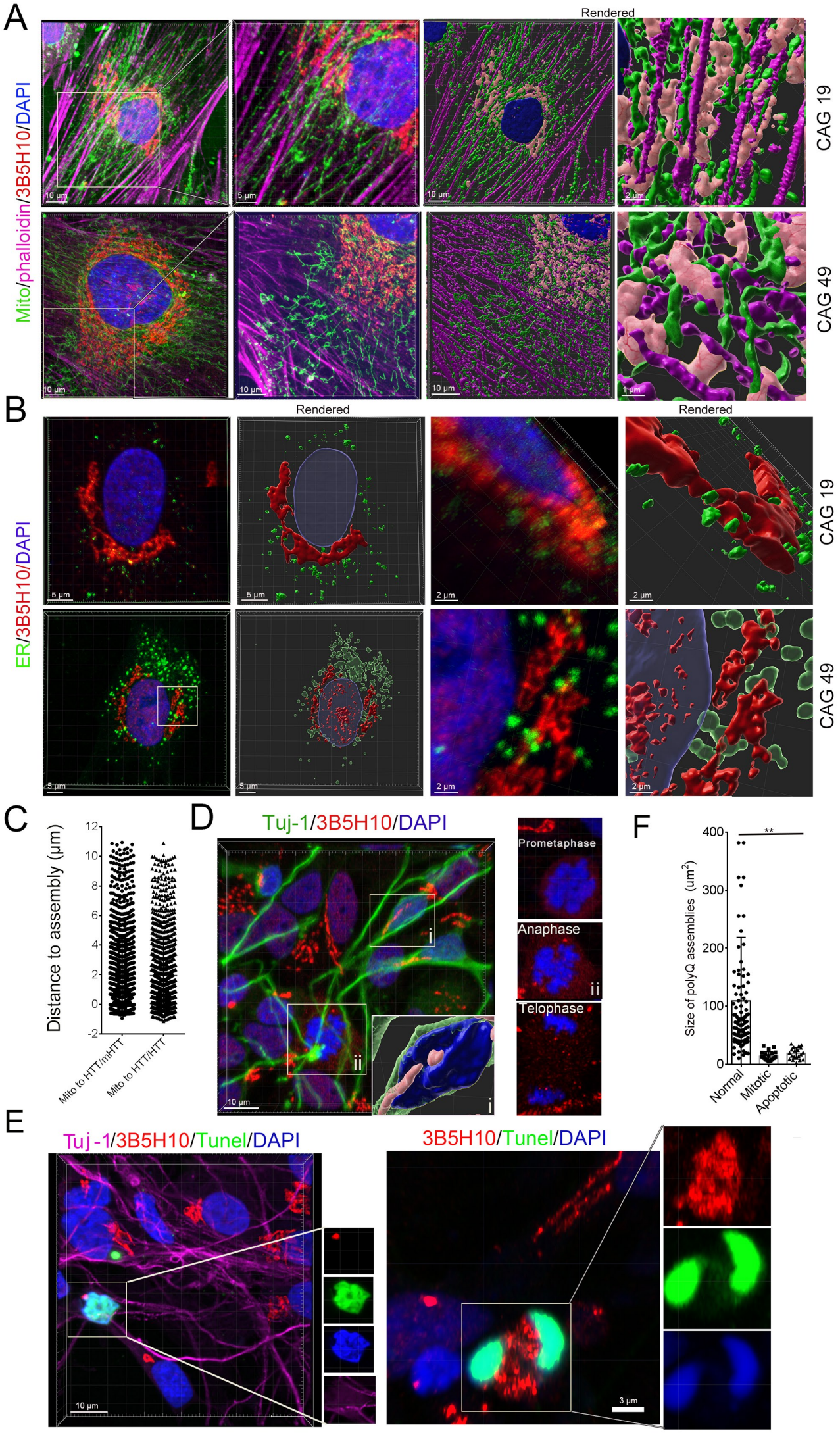
A
Rendered
Mito/phalloidin/3B5H10/DAPI
CAG 19
CAG 49
10 µm
5 µm
2 µm
1 µm
B
Rendered
Rendered
ER/3B5H10/DAPI
CAG 19
CAG 49
5 µm
2 µm
C
Distance to assembly (µm)
Mito to HTT/mHTT
Mito to HTT/HTT
D
Tuj-1/3B5H10/DAPI
Prometaphase
Anaphase
Telophase
i
ii
10 µm
F
Size of polyQ assemblies (um²)
**
Normal
Mitotic
Apoptotic
E
Tuj-1/3B5H10/Tunel/DAPI
3B5H10/Tunel/DAPI
10 µm
3 µm

Fig. S2

A

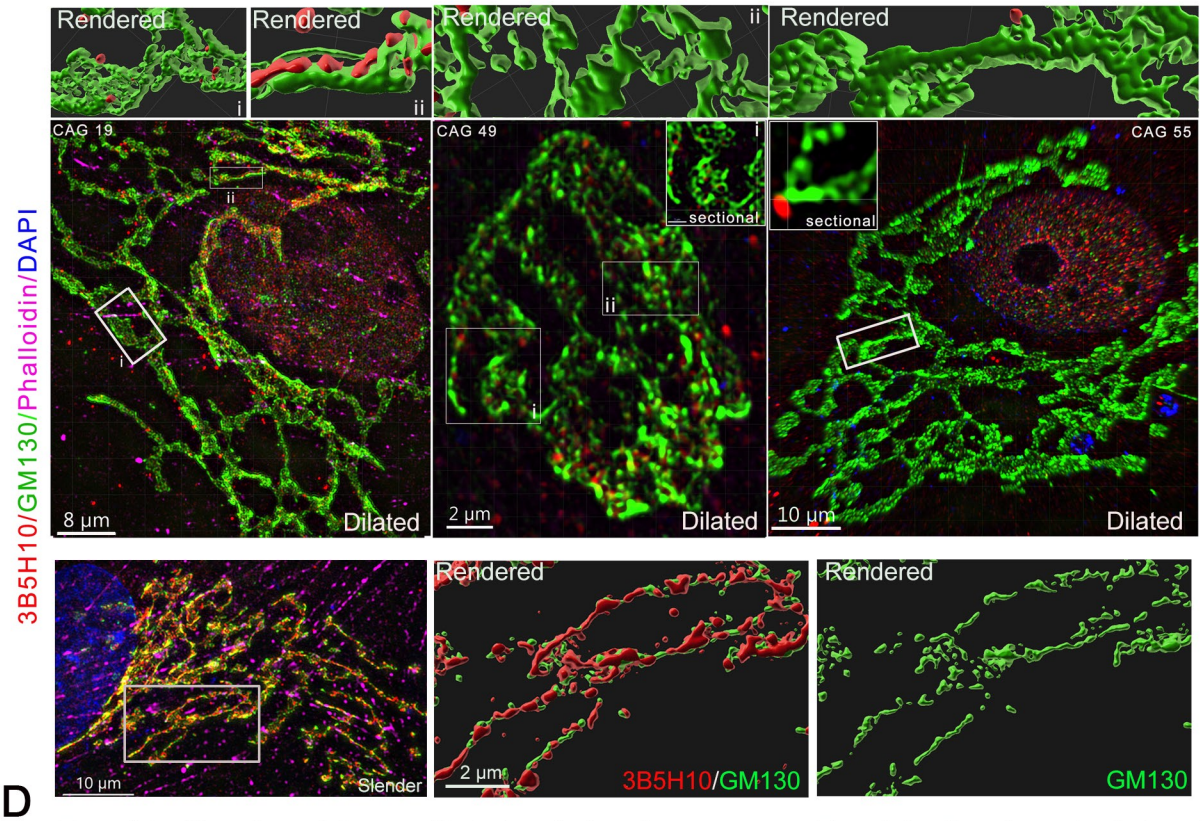

B

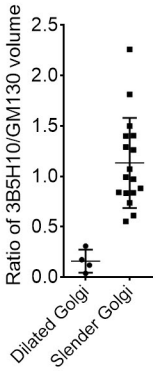

C

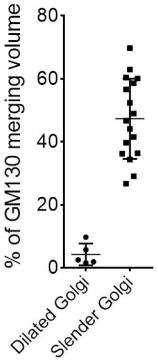

D

Freshly fixed and immediately stained

Freshly fixed and stained after 48h

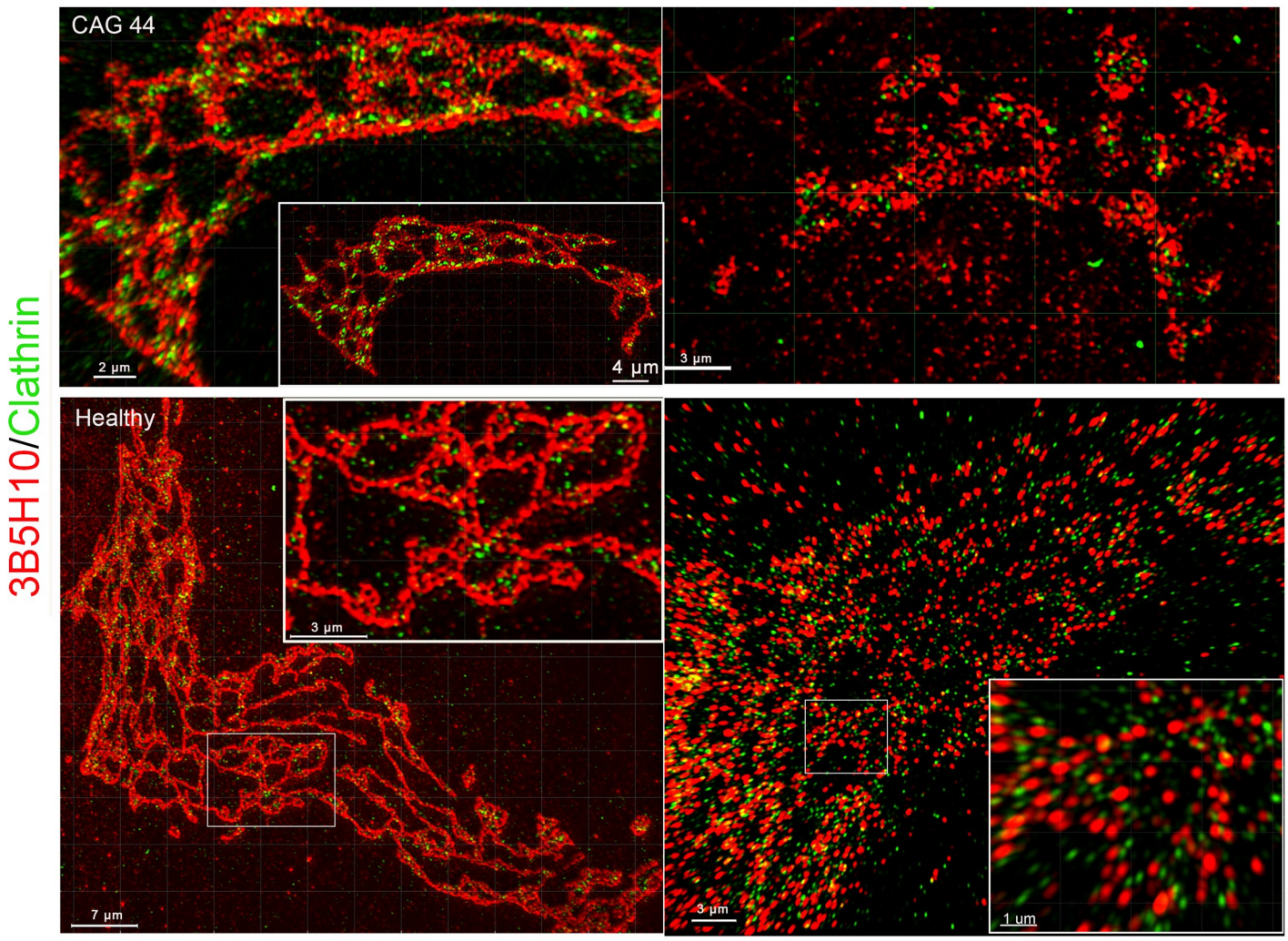

Fig. S3

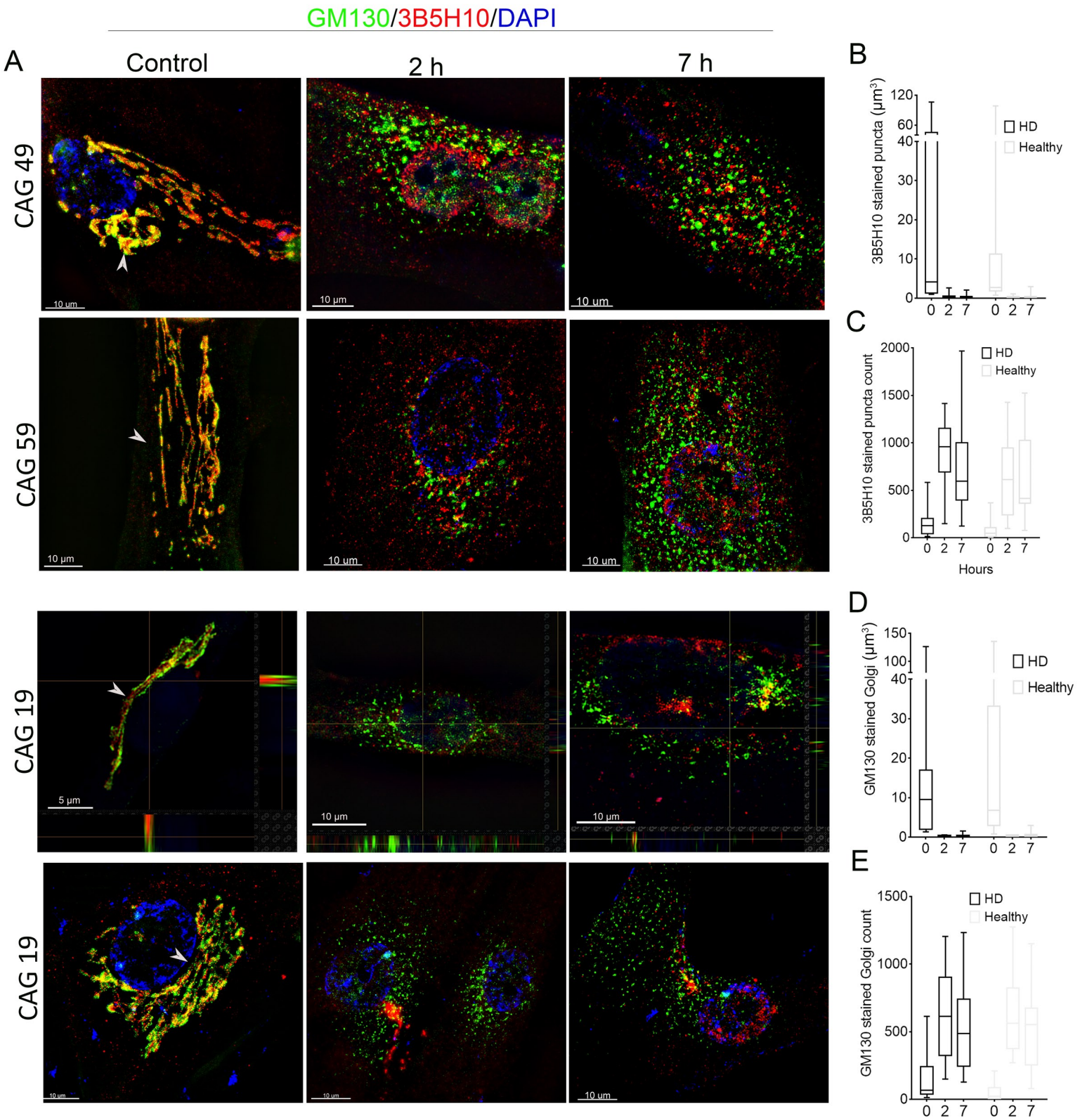
GM130/3B5H10/DAPI
A
Control
2 h
7 h
CAG 49
CAG 59
CAG 19
CAG 19
10 µm
5 µm
B
3B5H10 stained puncta (µm³)
HD
Healthy
C
3B5H10 stained puncta count
Hours
D
GM130 stained Golgi (µm³)
E
GM130 stained Golgi count

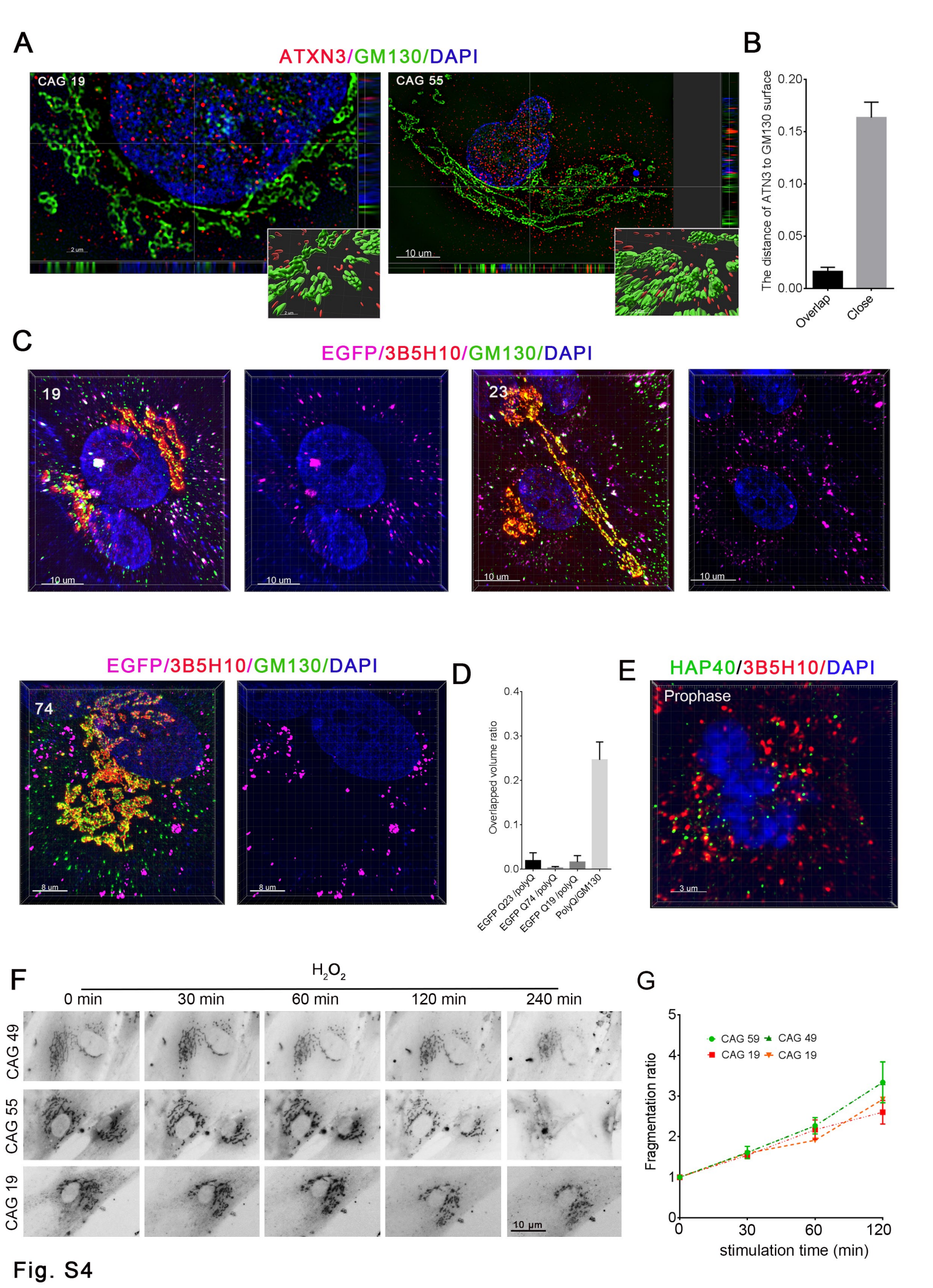
A
ATXN3/GM130/DAPI
CAG 19
CAG 55
10 um
B
The distance of ATN3 to GM130 surface
0.20
0.15
0.10
0.05
0.00
Overlap
Close
C
EGFP/3B5H10/GM130/DAPI
19
23
10 um
EGFP/3B5H10/GM130/DAPI
74
8 um
D
Overlapped volume ratio
0.4
0.3
0.2
0.1
0.0
EGFP Q23 /polyQ
EGFP Q74 /polyQ
EGFP Q19 /polyQ
PolyQ/GM130
E
HAP40/3B5H10/DAPI
Prophase
3 um
F
H2O2
0 min
30 min
60 min
120 min
240 min
CAG 49
CAG 55
CAG 19
10 μm
G
CAG 59
CAG 49
CAG 19
CAG 19
Fragmentation ratio
stimulation time (min)
0
30
60
120

Fig. S4

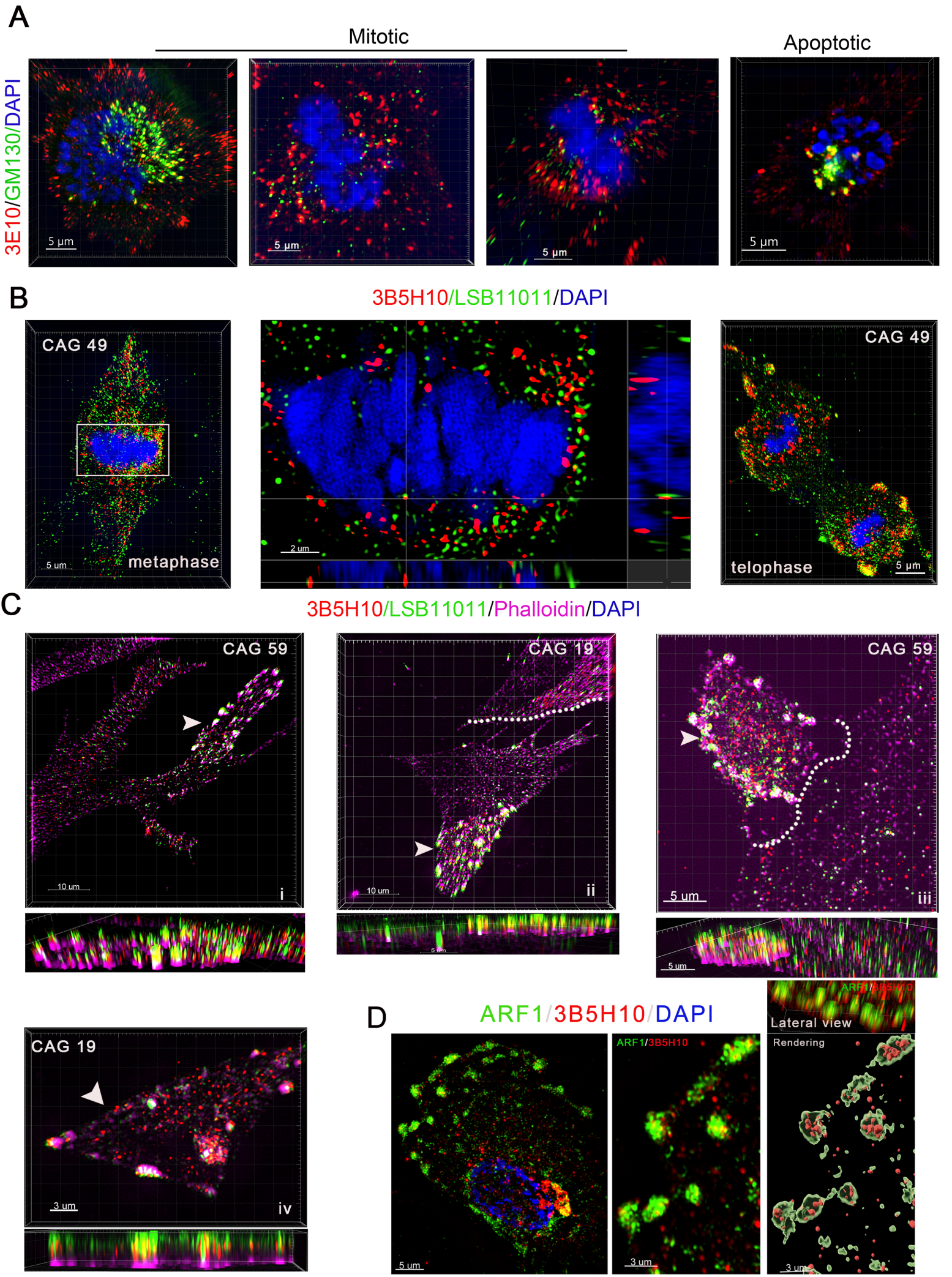
A
Mitotic
Apoptotic
3E10/GM130/DAPI
5 µm
5 µm
5 µm
5 µm
B
3B5H10/LSB11011/DAPI
CAG 49
5 um
metaphase
2 um
CAG 49
telophase
5 µm
C
3B5H10/LSB11011/Phalloidin/DAPI
CAG 59
10 um
i
CAG 19
10 um
ii
CAG 59
5 um
iii
5 um
CAG 19
3 um
iv
D
ARF1/3B5H10/DAPI
5 um
ARF1/3B5H10
3 um
Lateral view
Rendering
3 um

Fig. S5

Fig.S6

A

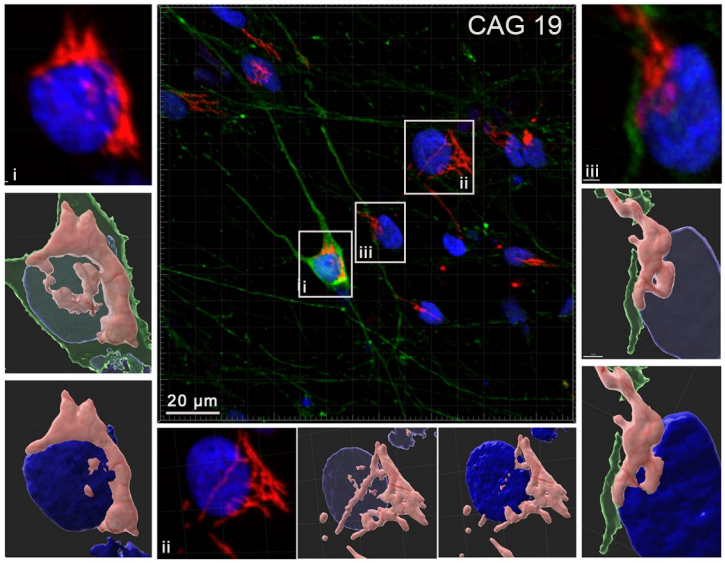

B

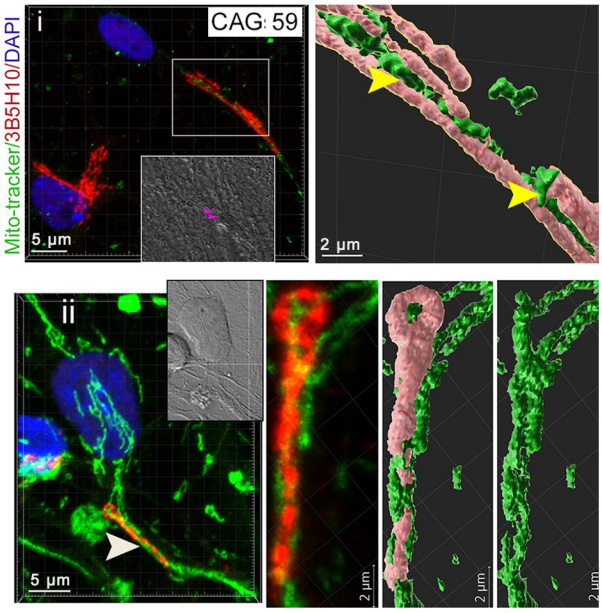

C

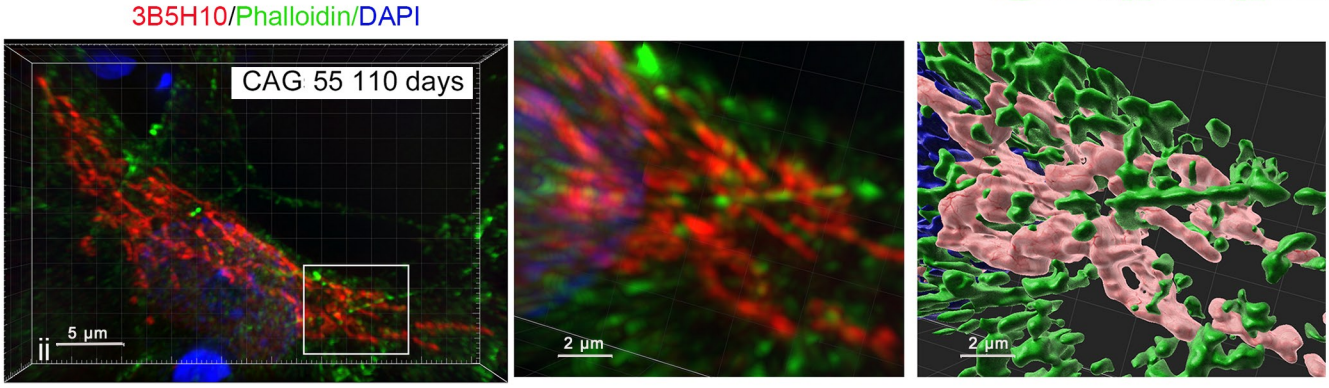

D

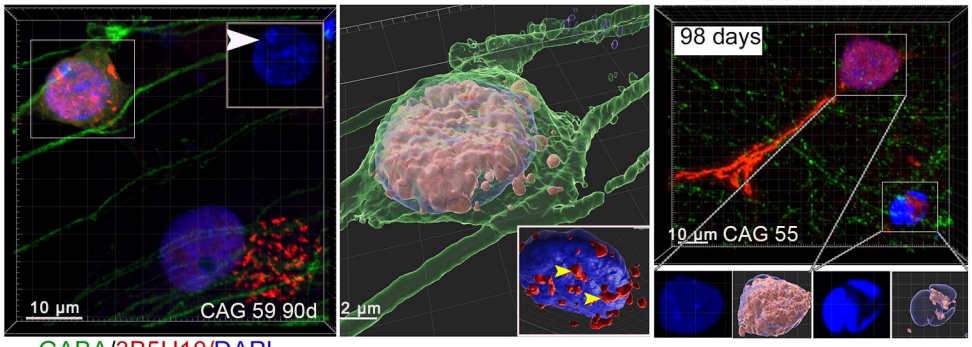

E

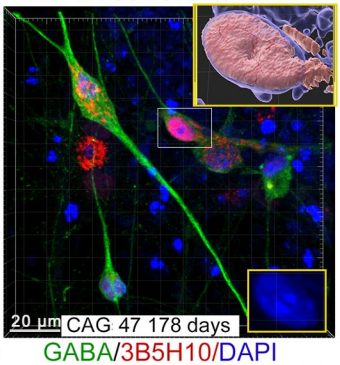

F

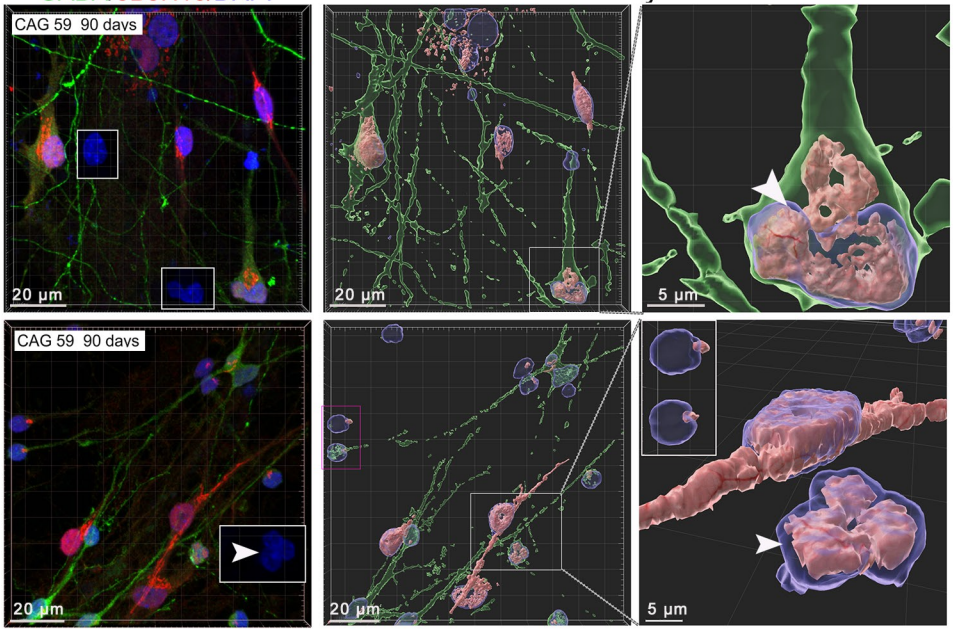

G

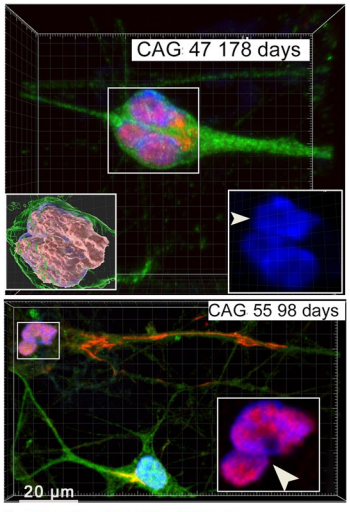

Summary of nuclear slicing in neruons

HD	Nuclear slicing	Total neurons	Image number
CAG 59	6	224	34
CAG 55	4	178	29
CAG 47	8	201	27

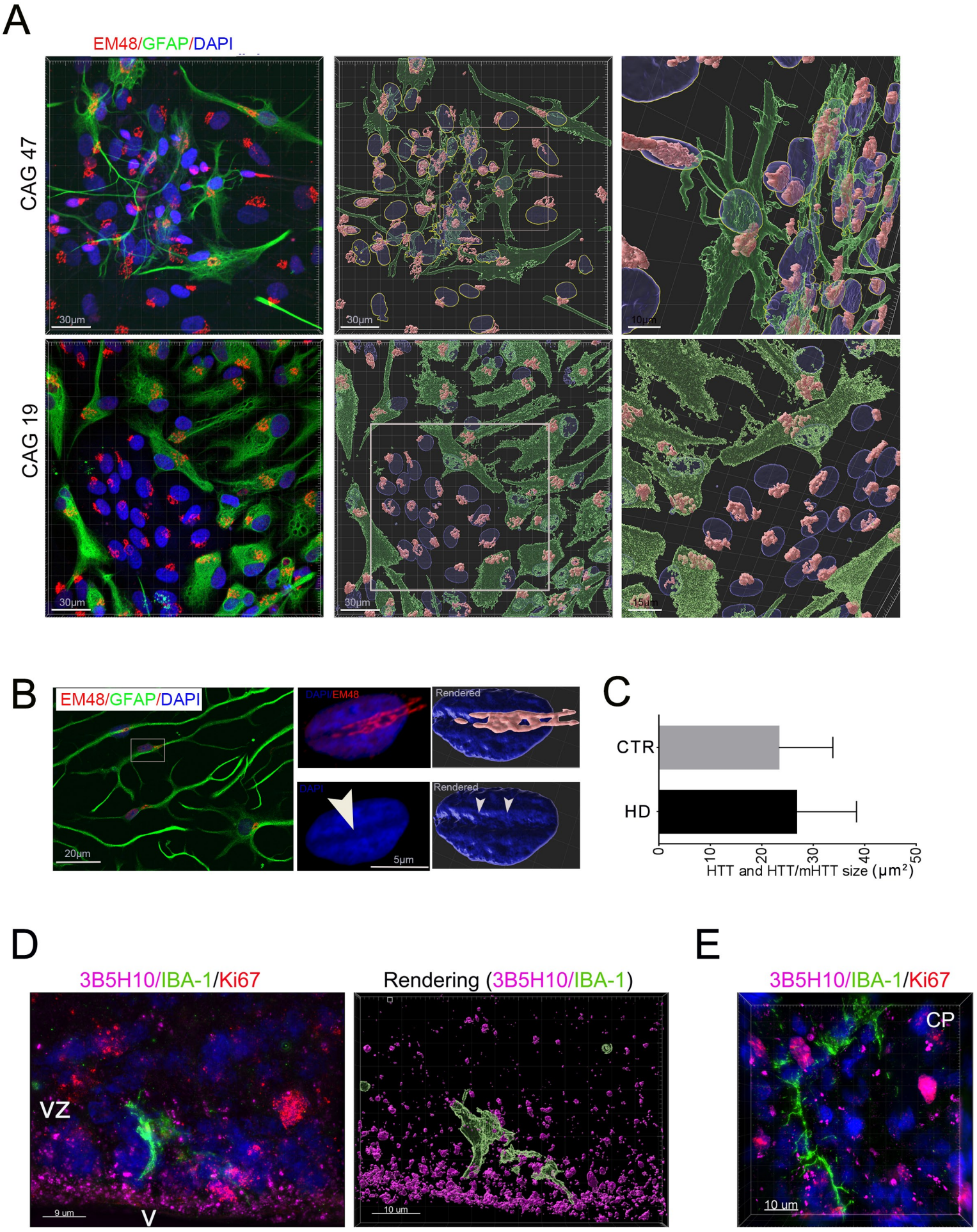
A
EM48/GFAP/DAPI
CAG 47
CAG 19
30μm
30μm
10μm
30μm
30μm
15μm
B
EM48/GFAP/DAPI
20μm
DAPI EM48
Rendered
DAPI
5μm
Rendered
C
CTR
HD
0
10
20
30
40
50
HTT and HTT/mHTT size (μm²)
D
3B5H10/IBA-1/Ki67
VZ
V
9 um
Rendering (3B5H10/IBA-1)
10 um
E
3B5H10/IBA-1/Ki67
CP
10 um

Fig. S7

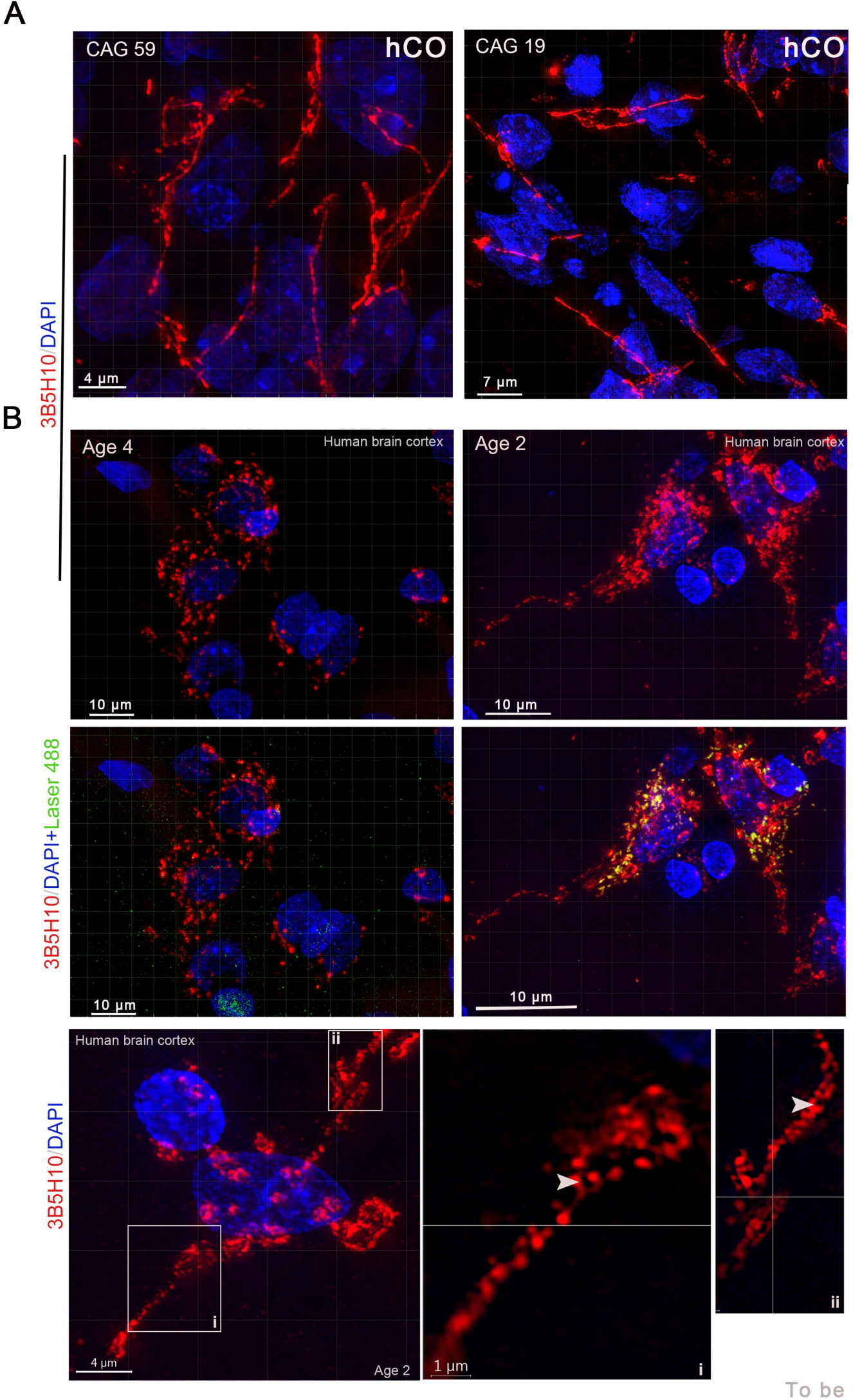

To be continued

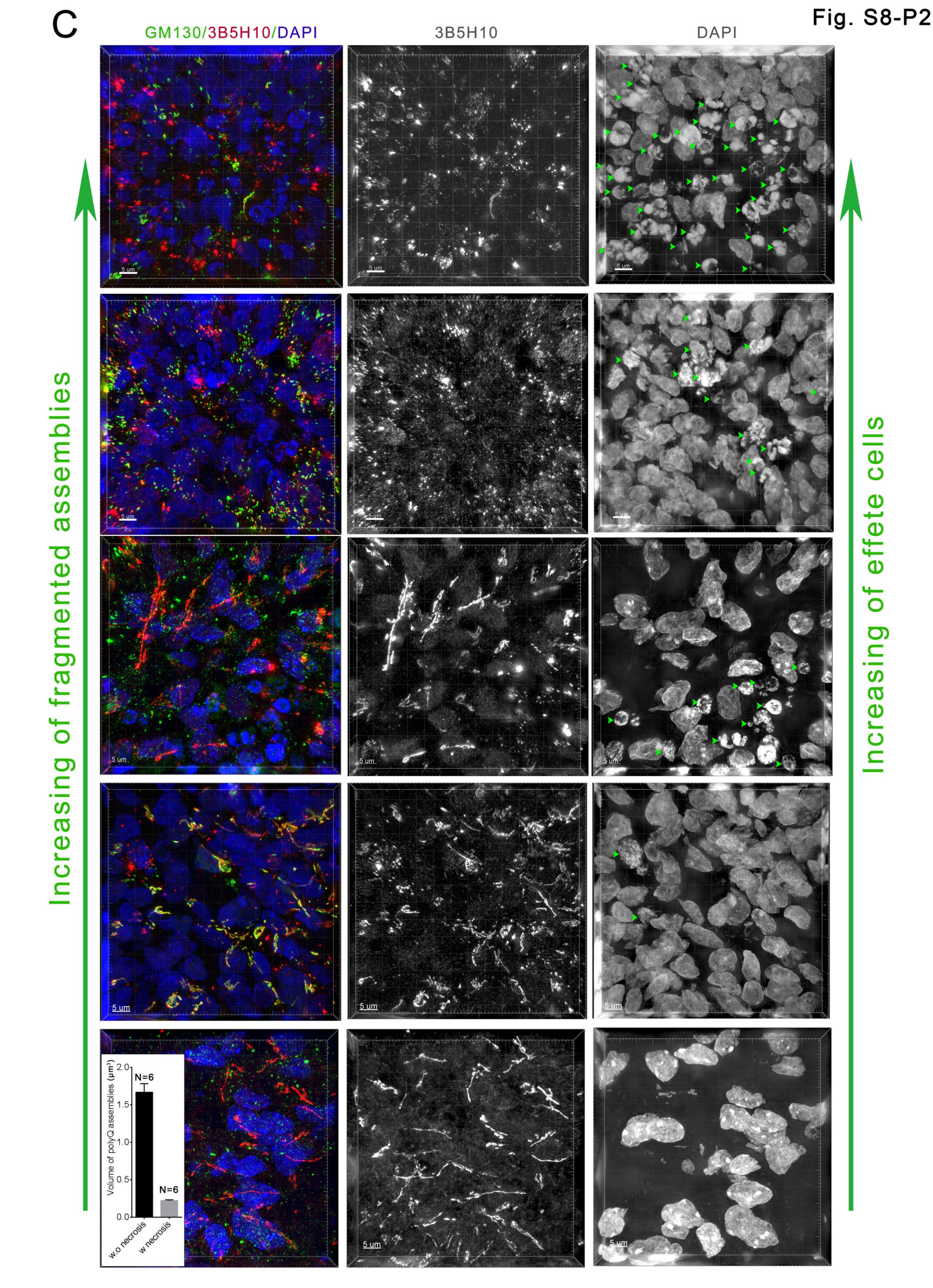
C
Fig. S8-P2
GM130/3B5H10/DAPI
3B5H10
DAPI
Increasing of fragmented assemblies
Increasing of effete cells
5 um
Volume of polyQ assemblies (μm³)
2.0
1.5
1.0
0.5
0.0
N=6
N=6
w.o necrosis
w necrosis

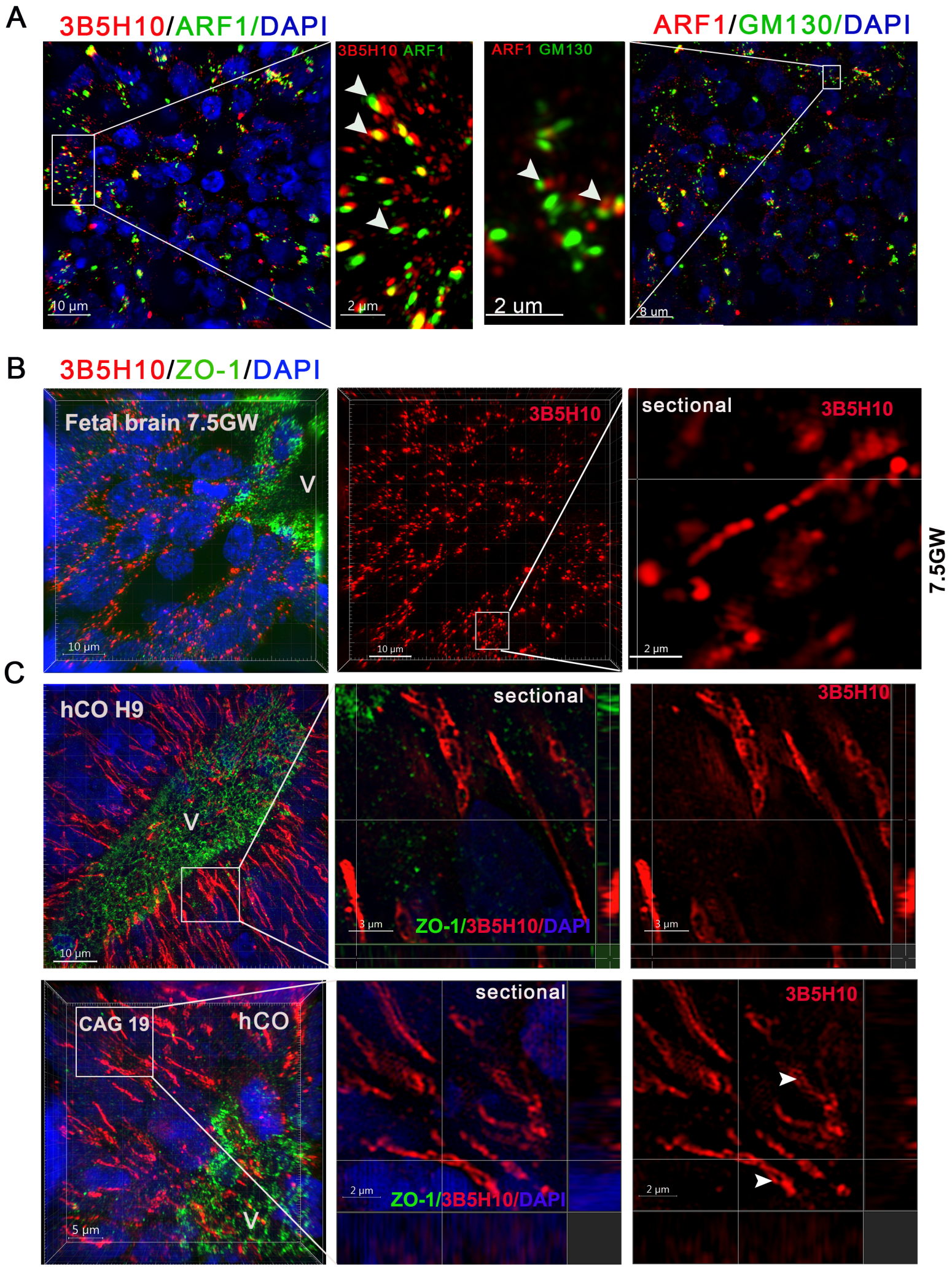
A
3B5H10/ARF1/DAPI
ARF1/GM130/DAPI
3B5H10 ARF1
ARF1 GM130
10 µm
2 µm
2 um
8 um
B
3B5H10/ZO-1/DAPI
Fetal brain 7.5GW
V
3B5H10
sectional
7.5GW
C
hCO H9
ZO-1/3B5H10/DAPI
CAG 19
hCO
5 µm

Fig. S9

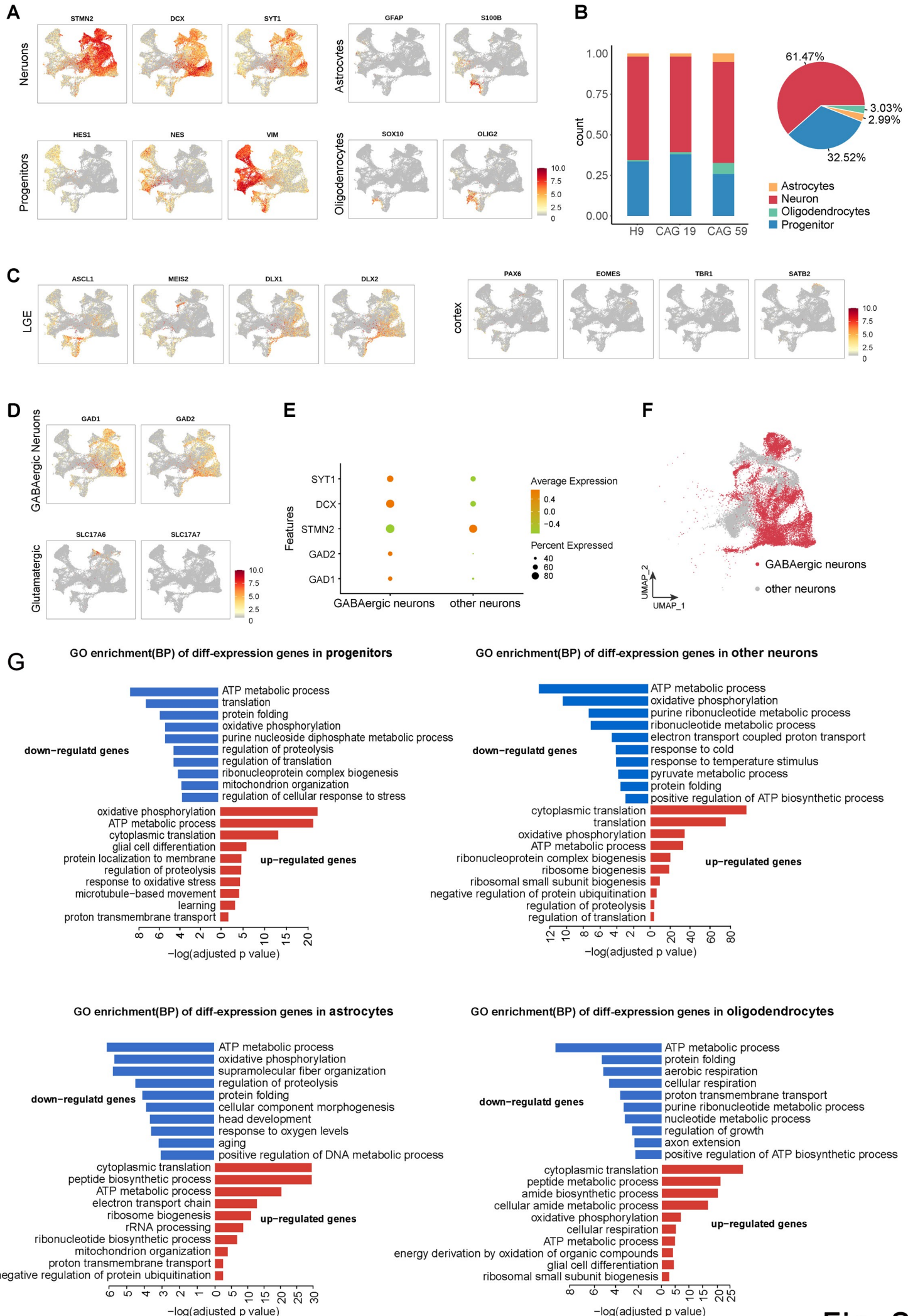
A
STMN2
DCX
SYT1
GFAP
S100B
Neruons
Astrocytes
HES1
NES
VIM
SOX10
OLIG2
Progenitors
Oligodenrocytes
10.0
7.5
5.0
2.5
0
B
count
1.00
0.75
0.50
0.25
0.00
H9
CAG 19
CAG 59
61.47%
3.03%
2.99%
32.52%
Astrocytes
Neuron
Oligodendrocytes
Progenitor
C
ASCL1
MEIS2
DLX1
DLX2
LGE
PAX6
EOMES
TBR1
SATB2
cortex
D
GAD1
GAD2
GABAergic Neruons
SLC17A6
SLC17A7
Glutamatergic
E
Features
SYT1
DCX
STMN2
GAD2
GAD1
GABAergic neurons
other neurons
Average Expression
0.4
0.0
−0.4
Percent Expressed
40
60
80
F
UMAP_2
UMAP_1
GABAergic neurons
other neurons
G
GO enrichment(BP) of diff-expression genes in progenitors
ATP metabolic process
translation
protein folding
oxidative phosphorylation
purine nucleoside diphosphate metabolic process
down−regulatd genes
regulation of proteolysis
regulation of translation
ribonucleoprotein complex biogenesis
mitochondrion organization
regulation of cellular response to stress
oxidative phosphorylation
ATP metabolic process
cytoplasmic translation
glial cell differentiation
protein localization to membrane
up−regulated genes
regulation of proteolysis
response to oxidative stress
microtubule−based movement
learning
proton transmembrane transport
−log(adjusted p value)
GO enrichment(BP) of diff-expression genes in other neurons
ATP metabolic process
oxidative phosphorylation
purine ribonucleotide metabolic process
ribonucleotide metabolic process
electron transport coupled proton transport
down−regulatd genes
response to cold
response to temperature stimulus
pyruvate metabolic process
protein folding
positive regulation of ATP biosynthetic process
cytoplasmic translation
translation
oxidative phosphorylation
ATP metabolic process
ribonucleoprotein complex biogenesis
up−regulated genes
ribosome biogenesis
ribosomal small subunit biogenesis
negative regulation of protein ubiquitination
regulation of proteolysis
regulation of translation
−log(adjusted p value)
GO enrichment(BP) of diff-expression genes in astrocytes
ATP metabolic process
oxidative phosphorylation
supramolecular fiber organization
regulation of proteolysis
down−regulatd genes
protein folding
cellular component morphogenesis
head development
response to oxygen levels
aging
positive regulation of DNA metabolic process
cytoplasmic translation
peptide biosynthetic process
ATP metabolic process
electron transport chain
ribosome biogenesis
up−regulated genes
rRNA processing
ribonucleotide biosynthetic process
mitochondrion organization
proton transmembrane transport
negative regulation of protein ubiquitination
−log(adjusted p value)
GO enrichment(BP) of diff-expression genes in oligodendrocytes
ATP metabolic process
protein folding
aerobic respiration
cellular respiration
down−regulatd genes
proton transmembrane transport
purine ribonucleotide metabolic process
nucleotide metabolic process
regulation of growth
axon extension
positive regulation of ATP biosynthetic process
cytoplasmic translation
peptide metabolic process
amide biosynthetic process
cellular amide metabolic process
oxidative phosphorylation
up−regulated genes
cellular respiration
ATP metabolic process
energy derivation by oxidation of organic compounds
glial cell differentiation
ribosomal small subunit biogenesis
−log(adjusted p value)

Fig. S10

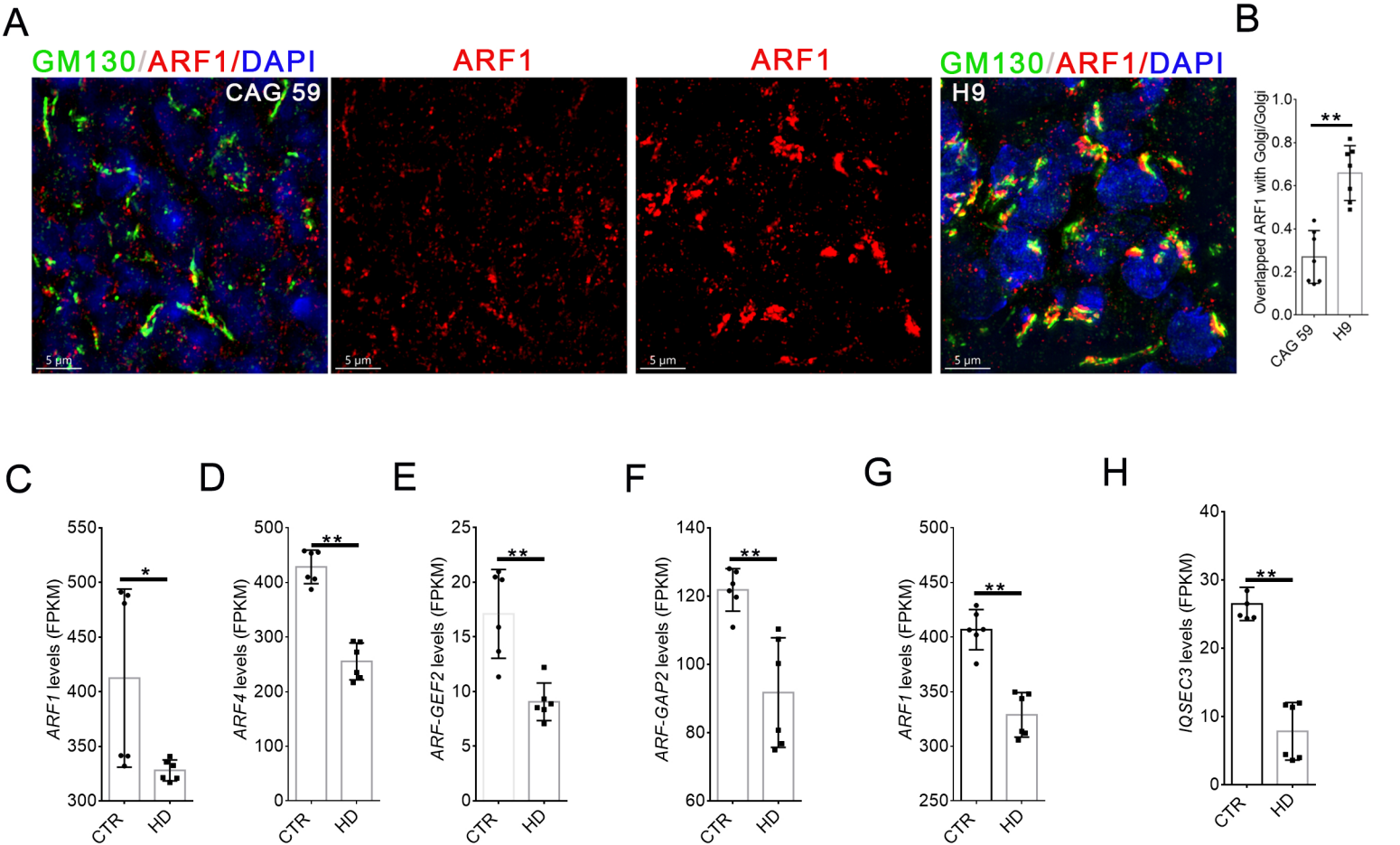
A
GM130/ARF1/DAPI
CAG 59
ARF1
ARF1
GM130/ARF1/DAPI
H9
5 µm
B
Overlapped ARF1 with Golgi/Golgi
CAG 59
H9
C
ARF1 levels (FPKM)
D
ARF4 levels (FPKM)
E
ARF-GEF2 levels (FPKM)
F
ARF-GAP2 levels (FPKM)
G
ARF1 levels (FPKM)
H
IQSEC3 levels (FPKM)
CTR
HD

Fig. S11

Extended Data

Figure legends

Supplementary Fig. 1. PolyQ assemblies rarely and randomly colocalize with mitochondria and rER, and fragment in mitotic and apoptotic cells.

A. Mito-tracker, phalloidin and 3B5H10 antibody immunostaining in the fibroblasts of HD patients (CAG 49) and healthy siblings. 3D rendering revealed the spatial relationships of polyQ assemblies with mitochondria.

B. rER-tracker and 3B5H10 antibody staining in the fibroblasts of HD patients (CAGs, 49) and healthy siblings. 3D rendering revealed the spatial relationships of polyQ assemblies with rER.

C. The distance of mitochondria to polyQ assemblies with or without mHTT. Distances were measured by object-object statistics in Imaris 9.8

D, E. 3B5H10 stained polyQ puncta/patch in the mitotic (D) and apoptotic cells (E) (Tuj-1 and 3B5H10 antibodies immunostaining and TUNEL staining).

F. Comparing the size of polyQ region in healthy cells with mitotic/apoptotic cells. Mitotic cells, n=20; Apoptotic cells, n=19. All data, means ± s.e.m.s. *, $p < 0.05$, **, $p < 0.01$, ns, no significant difference.

Supplementary Fig. 2. PolyQ assemblies in fibroblasts are fragile in post-fixation

A. GM130 and 3B5H10 antibodies and phalloidin staining in the fibroblasts revealed that the dilated Golgi absent polyQ assemblies. The upper panels rendered tomography visualize the spatial relationship of Golgi with polyQ puncta. The lower panels are a typical cell with slender Golgi.

B. The overlapped volume of polyQ assemblies/patches with dilated Golgi and flat/slender Golgi. Student *t*-test; **, $p<0.01$.

C. The representative image of clathrin and 3B5H10 antibodies immunostaining in HD patient (CAG 44) and healthy sibling fibroblasts by two different protocols. Left panels are freshly fixed and immediately stained groups (within 1h after fixation), the right panels are freshly fixed and lately

stained (stored over 48h after fixation in PBS buffer). Images were taken by SIM microscopy with Z-stacks.

Supplementary Fig. 3. BFA treatments fragmented polyQ assemblies and Golgi stack/ribbon

A. The representative SIM images of the fibroblasts from 4 members of HD family (CAG 59, CAG 49, CAG 19 and CAG 19) treated by BFA for 2 h and 7 h and immunostained with GM130 and 3B5H10 antibodies revealed that the exposure to BFA uniformly fragmented polyQ assemblies and Golgi stacks\ribbons and caused the detachment of polyQ assemblies from Golgi (white arrows, the large assemblies).

B. The volume of 3B5H10 stained assemblies/puncta in fibroblasts. The measuring was done by IMARIS software. Images, n: 7-12. Sample size: n=2 in each group.

C. The count of 3B5H10 stained assemblies/puncta in the fibroblasts. Images, n: 7-11. Sample size: n=2 in each group

D. The volume of GM130 stained Golgi in the fibroblasts. Images, n: 7-11. Sample size: n=2 in each group

E. The count of GM130 stained Golgi in the fibroblasts. Images, n: 7-11. Sample size: n=2 in each group

Supplementary Fig. 4. PolyQ assemblies rarely overlapped with ATXN3 and transfected exogenous first exon fragment of HTTs

A, B. The sectional view of ATXN3 and 3B5H10 antibodies coimmunostaining reveal that polyQ assemblies barely include ATXN3 protein (A) (Inner panel, rendered 3D image by IMARIS). The percentage of ATXN3 puncta overlapped or contacted with polyQ assemblies (B). Data, mean ± SD. Close: the distance to Golgi<0.5 μm; Overlapped: the distance to Golgi<0.1 μm. The distance was measured by object-object statistic of IMARIS after rendering the signals.

C. The 3D view images of the fibroblasts transfected by the vector of *HTT* first exon (Q19, Q23 and Q74) were immunostained by 3B5H10 and GM130 antibodies.

D. The overlapped volume of the first exon fragments of HTT (Q19, Q23 and Q74) with 3B5H10 stained polyQ assemblies. The overlapped volumes were measured by object-object statistic of IMARIS after rendering each channel. Data, mean±SD.

E. Coimmunostaining of 3B5H10 antibody with HAP40 antibody revealed that polyQ puncta are attached by HAP40 puncta in mitotic cells (white arrows, typical attached pattern).

F. Image sequences of Golgi in the fibroblasts of HD family under oxidative stress at indicated time points.

G. The fragmentation ratio of Golgi under H_2O_2 stimulation at different time points. Fragmentation ratio = number of Golgi of one cell in each time point/ number of Golgi at 0 min. Two-way ANOVA. *, $p<0.05$; **, $P<0.01$.

Supplementary Fig. 5 The status of HTTs in mitotic/apoptotic cells and cellular fragments

A, B. 3E10/LSB11011 and GM130 antibodies immunostaining revealed that HTTs /mHTTs distribution pattern in the fibroblasts is identical polyQ staining patterns in mitotic and apoptotic cells (A). A mitotic cell in telophase contain multiple HTT^+ vacuoles (CAG 49) (B).

C. The protruded ruffling membrane and detached cellular fragments enriched HTTs. i, a finger-like projection enriched with HTT; ii and iii, a projection enriched with HTTs partially detached from cytoplasm; iv, two finger-like projections and a small fragment enriched with HTTs and F-action in fibroblasts; v and vi, a completely detached cellular fragment enriched with HTTs (white arrows, HTTs enriched structure; dashed line, detached border).

D. ARF1 and 3B5H10 antibody immunostaining in a fibroblast with membrane ruffling. The right panel is the rending of middle panel. The upper panel in the right showed a lateral view which showed the relationship of ARF1 with polyQ.

Supplementary Fig. 6. Characteristics of polyQ assemblies of HTT with/without mHTT in neurons

A. EM48 and GABA antibodies immunostaining of HD GABAergic neurons

cultured over 100 days.

B. Mito-tracker and 3B5H10 antibody staining in HD neurons showed a few mitochondria stand between the spindles of polyQ assemblies with mHTT (i) (yellow arrows mitochondria; inner panel, DIC image of projections revealing a gorge; pink arrows, deep gorge) or twist with polyQ assemblies. 3D rendered tomography showed the strangled (i) and twisted mitochondria (ii) (white arrow, mitochondria twisting with polyQ assemblies, and the rendered region in the right panels).

C. Phalloidin and 3B5H10 staining of HD GABAergic neurons differentiated for 110 days showed that actin filaments did not tangle or parallel poly assemblies with mHTT in GABAergic neurons.

D. PolyQ puncta deposit into the nucleus and poke the nuclear membrane of GABAergic neurons (white arrow, the morphology of nucleus; yellow arrows, nucleus poked by polyQ assemblies). An apoptotic cell in the slide contains fragmented 3B5H10 stained fragments in the nucleus (CAG 55).

E. PolyQ puncta with mHTT precipitates completely occupied the nucleus of GABAergic neurons cultured for 178 days (CAG 47), showing a typical apoptotic morphology with condensed chromatin (white arrows, an apoptotic nucleus with condensed chromatin; inner insert, a rendered tomography).

F, G. HD patient GABAergic neurons derived from iPSCs cultured for 90 days (CAG 59) and 98 days (CAG 55) and 110 days (CAG 47) have spliced nucleus (white arrows, spliced nucleus; 3 of over 200 neurons).

Supplementary Fig. 7. HTT/mHTT assembly in astrocyte derived HD patient and healthy sibling iPSCs

A. GFAP and EM48 antibodies staining of the astrocytes derived from HD patient and healthy sibling iPSCs showed HTT/mHTT and HTT/HTT assembly in astrocytes. No HTT/mHTT deposition into the nucleus of astrocytes was observed.

B. The spindle of HTT/mHTT and HTT/HTT assembly formed a dent on the nuclear surface of astrocytes. Scale bar, 20 μm. Data, means±s.e.m.

C. Comparing the size of HTT/mHTT assemblies with HTT/HTT assemblies in astrocytes.

D, E. The immunostaining with 3B5H10/IBA-1/Ki67 antibodies in fresh fetus brain with 14 GW revealed that the microglia contain a limited amount of polyQ compared to the neuroepithelial in VZ region and the processes of microglia did not have polyQ of HTT. CP, cortical plate; VZ, ventricle zone.

Supplementary Fig. 8. PolyQ assemblies mostly fragmented in human brain surgical samples and human brain organoids with necrotic cells or regions

A. Intact and continuous polyQ assemblies with/without mHTT in the neurons of hStrO without necrosis.

B. Fragmented/discontinuous polyQ assemblies in freshly surged human brain samples (tissues from 4-year-old and 2-year-old glioblastoma patients). The 488-laser excited autofluorescent signals in brains used to identify the autofluorescent signal. Merged yellow fragments are autofluorescent (mostly from lipofuscin).

C. The fragmentation of polyQ assemblies is depended on the ratio of necrotic cells in the surrounding regions (green arrows, necrotic cells).

D. The volume of polyQ assemblies in region with (w) necrosis and the region without (w.o) necrosis. The volume is measured Imaris. n,1867 (w.o); n, 1473 (w).

Supplementary Fig. 9. The characteristics of polyQ assemblies in the neuroepithelial cells of VZ/SVZ region in fetus brain and hCO neural tubes.

A. The immunostaining with ARF1 and 3B5H10 or GM130 antibodies in the necrotic regions of hCOs showed that most fragmented polyQ and Golgi in necrotic sites conjugated with ARF1 (white arrows, ARF1 conjugated polyQ).

B, C. ZO-1 and 3B5H10 antibodies immunostained the pseudostratified neuroepithelium of neural tube in human fetal brain at 7.5 GW and hCOs from HD patients, H9 and healthy sibling showed that the polyQ assemblies, which

were formed by small ring-like unit and paralleled the apical-basal axis of cells, are heavily fragmented in human fetal brain samples stored in -80℃ for 6 years after sectioning (A) and intact in hCOs from HD patients, H9 and healthy (B). V, ventricle; white arrows, the ring-like structure.

Supplementary Fig. 10. Characterizing and sorting the cellular types from scRNA-seq data of hStrOs and GO analyses of different cellular clusters in scRNA-seq data of hStrOs

A. Expression of known markers of progenitor, neuron, astrocyte and oligodendrocyte.

B. Stacked bar plots and pie chart representing the proportion of cell types.

C, D. Expression of known markers of LGE progenitors and cortical progenitors(C), GABAergic neurons and glutamatergic neurons (D).

E. Dot plot displaying expression of GABAergic neurons marker genes.

F. UMAP plot of neurons colored by GABAergic neurons (red) and other neurons (grey).

G. GO enrichment analysis of down-regulated (top) and up-regulated (bottom) genes in CAG59 VS CAG19/H9 progenitor, other neuron, astrocyte and oligodendrocyte.

Supplementary Fig. 11. ARF related activities were reduced in brain organoids

A. ARF1 and GM130 antibody immunostaining in hCOs revealed that the cortical neurons of HD hCOs bind fewer ARF1 than that of healthy hCOs.

B. The overlapped volume of ARF1 with Golgi in HD hCOs and healthy hCOs. The volumes are measured by IMARIS. Student t-test; **, $p<0.01$.

C-F. Bulk RNAseq data of HD hStrOs (CAG 55 and 59) and healthy hStrOs (CAG 19 and H9) at 60 days revealed *ARF1, ARF4, ARF-GEF2, ARF-GAP2* transcription levels. *Student t-test; *, $p<0.05$; **, $p<0.01$.*

***G*, H.** The bulk RNAseq data of HD hStrOs (CAG 55 and 59) and healthy hStrOs (CAG 19 and H9) at 80 days revealed *ARF1, IQSEC* transcription

levels. Student t-test; ***, $p<0.01$.* CTR, healthy.

Supplementary Materials and Methods

Primer and sequencing

A nurse collected blood from the vein of the upper arm, and a Blood DNA isolation Kit extracted blood DNA. After PCR amplification, the mutant band splits from the wild type band with a 4% Agarose gel, and then the band was cut and extracted by DNA Gel Extraction Kit (GenElute™, Sigma Aldrich). The extract was sequenced by the Sanger method.

The sequencing primers:

A1: 5'-CAGAGCCCCATTCATTGCC-3'

B1: 5'-TGAGGAAGCTGAGGAGGC-3'

Glucose starvation assays for polyQ assemblies and Golgi

Cultured the fibroblasts in 24-well plate with cover glasses (Φ20mm). After two days, the medium was replaced by low-glucose medium without FBS. The cells in low glucose medium were fixed at 24 h, 48 h, and 72 h and stained by 3B5H10 antibody and phalloidin. At 72 h, the medium was replaced by high glucose medium without FBS and cultured for another 48 h and then fixed and stained by 3B5H10 antibody and phalloidin. ImageJ software were used to measure the polyQ assemblies. Imaris were used to render the image.

A group of fibroblasts were stained by GM130 antibodies at 48 h after supplying low-glucose medium for Golgi changes.

Golgi apparatus-selective staining and imaging in the live cells

Replated fibroblasts in glass-bottomed 35mm dishes (biosharp, BS-20-GJM). Golgi apparatus in live cells were labeled using the GOLGI ID Green assay kit (ENZO, ENZ-51028-K100), a Golgi apparatus-selective dye. Prepared the Assay Solution and the Detection Reagent by following the guidelines of manufacturer. After preparation, these agents were fully mixed. After washing the cells with Assay Solution, dispensed sufficient volume of Detection Reagent to cover the monolayer cells, incubated for 30 minutes at 37°C. Before imaging, washed the cells 3 times and incubated the cells in medium at 37°C for another 30 minutes. For imaging, sequential images were captured

from multiple ROIs (region of interest) in dishes. The time intervals were 30 min, 60 min, 120 min and 240 min.

Neural differentiation

The cells were differentiated according to the neural differentiation protocol described [1]. Briefly, dissociated WT-iPS and HD-iPS were plated on Matrigel (BD) at a density of 3.5×10^4 cells/cm^2 and maintained in E8 medium (Thermo fisher scientific) for 4-5 days until they reached 90% confluence. After digested by EDTA, 9000 cells were plated in each well of U-shaped 96 wells（SUNILON）. On the first day, we maintained these cells in E8 and hNM (1:1 mixture). On the second day, the medium was replaced with hNM. From the day of start to day 6, the medium with two μMol/L SB431542 (Tocris) and 0.3μMol/L LDN193189 (BMP inhibitor, Tocris) was used for culture. These cells were plated on a well on day 7, and 200ng/ml SHH or 0.65 μMol/L Purmorphamine were supplied at day 10 for the differentiation of GABAergic neurons. The cells were maintained in the same medium for 2 weeks. The medium without SHH or Purmorphamine is used for differentiating glutamate neurons. At 15 days of differentiation, the rosettes were collected and cultured in a suspension condition for 25 days. On day 25, these cells were plated on a cover glass double-coated by polyonithin and laminin after digesting with accutase and then supplemented by a neural induction medium (composed of Neurobasal, N2 100×, B27 50×) (Invitrogen), supplemented with 10 ng/ml BDNF (Peprotech), 10 ng/ml GDNF (Peprotech) and 10 ng/ml IGF (Peprotech).

Human brain organoid construction

Brain organoids were constructed by following our protocol[2]. Briefly, ES/iPS colonies were dissociated into a single-cell with Accutase (Gibco, A1110501). 9,000 dissociated cells were plated into each well of a V-bottom ultra-low-attachment 96-well plate (Sumitomo Bakelite, MS-9096VZ). Induction media contained Human Neural differentiation Medium and E8 media (1:1), supplemented with the two SMAD inhibitors 0.3μM LDN-193189 (STEMGENT,

040074), 2μM SB431542 (Ametek Scientific, DM-0970), and 10 μm Y-27632 (APE.BIO, A3008). On the sixth day in suspension, hCOs were transferred to neural differentiation media containing 1:1 mixture of DMEM-F12 media and Neurobasal media supplemented with 1% (v/v) MEM-NEAA (Gibco, 11140-050), 1% (v/v) GlutaMAX(Gibco, 35050-061), 1% (v/v) N2 supplement (Gibco, 17502-048), 2% (v/v) B27 supplement (Gibco,), 1% (v/v) Penicillin/Streptomycin (Gibco, 2051357). Growth factors 10ng/ml EGF (R&D Systems, 236-EG) and 20 ng/ml bFGF (R&D Systems, 233FB/CF) were used from day6 to day23. Growth factors the 20 ng/ml BDNF (Peprotech, AF450002) and 10 ng/ml GDNF (Peprotech, AF450010) were used from day 24 to day 45.

Preparation and data analysis of Single-cell RNA-sequencing library

110 days differentiated hStrOs of a HD patient (CAG 59) and a healthy sibling and H9 in suspension culture are prepared for analysis. A sterile dish with 10 ml 1x Dulbecco's Phosphate-Buffered Saline (DPBS; Thermo Fisher, 14190144) on ice is used to transport samples after removing the residual solution. Neurosphere Dissociation Kit (Miltenyi, 130-095-943) used to create single-cell suspensions. Dissociated cells were rinsed 1x DPBS containing 2% FBS. 0.4% Trypan blue staining (Thermo Fisher, 14190144) is to check the viability on Countess® II Automated Cell Counter (Thermo Fisher).

10x library preparation and sequencing

Beads with unique molecular identifier (UMI) and cell barcodes were loaded close to saturation, so that each cell was paired with a bead in a Gel Beads-in-emulsion (GEM). After exposure to cell lysis buffer, polyadenylated RNA molecules hybridized to the beads. Beads were retrieved into a single tube for reverse transcription. On cDNA synthesis, each cDNA molecule was tagged on the 5’end (that is, the 3’end of a messenger RNA transcript) with UMI and cell label indicating its cell of origin. Briefly, 10× beads that were then subject to second-strand cDNA synthesis, adaptor ligation, and universal amplification. Sequencing libraries were prepared using randomly interrupted whole-transcriptome amplification products to enrich the 3’ end of the

transcripts linked with the cell barcode and UMI. All the remaining procedures including the library construction were performed according to the standard manufacturer's protocol (Chromium Single Cell 3' v3). A High Sensitivity DNA Chip (Agilent) on a Bioanalyzer 2100 and the Qubit High Sensitivity DNA Assay (Thermo Fisher Scientific) quantified sequencing libraries NovaSeq6000 (Illumina) using 2x150 chemistry sequenced the libraries.

Single cell RNA-seq data processing and analysis

Cell Ranger 4.0 pipeline with default and recommended parameters processed Reads, Gene-Barcode matrices were generated for each sample by counting UMIs and filtering non-cell associated barcodes, and a gene-barcode matrix that contains the barcoded cells and gene expression counts were generated. After obtaining the single-cell expression matrix, we used the Seurat (v4.0.5)[3] R toolkit to perform normalization, clustering, dimensionality reduction, and visualization. Cells that had the number of detected genes less than 200 and the percentage of mitochondrial genes lower than 10% were removed. Gene counts were then log transformed and scaled, and 3000 shared highly variable genes were identified using the FindVariableFeature function. We applied the Runharmony function with the Seurat-based principal component analysis (PCA) reduction method in the Harmony (v0.1.0)[4] package to correct the batch effects for generating low-dimensional matrices. A nearest neighbor graph was calculated using FindNeighbors and clustered using FindClusters, followed by the visualization of cell clusters with uniform manifold approximation and projection(UMAP). We used the well-known marker genes to assign these clusters to corresponding cell types. Differentially expressed genes(|log2FC|>0.25 and adjusted p value<0.01) among GABAergic neurons (CAG 59 vs CAG 19, CAG 59 vs H9) were identified by the Seurat function FindMarkers.

Functional enrichment

Enrichment GO categories for significantly differentially expressed genes were

identified by Metascape(https://metascape.org/gp/)[5], which utilizes hypergeometric test and Benjamini-Hochberg p-value correction algorithm to identify acceptable ontology terms. Adjusted p value of GO biological processes <0.01 was considered to be significant enrichment terms. The gene set enrichment score of Golgi vesicle transport (GO:0048193) was calculated by AUCell(v.1.14.0)[6]. AUCell_buildRankings and AUCell_calcAUC algorithm was used for ranking model building and the "Area Under the Curve" (AUC) scores calculation.

Data availability

The sequencing datasets generated and/or analyzed during this study are available in the Sequence Read Archive (SRA) and Gene Expression Omnibus (GEO) with the following accession numbers for anyone: Day 60 and day 80 MSN in hStrO for bulk RNA-seq (PRJNA760260), Day 110 MSN culture in hStrO for scRNA-seq (GSE184255). The proteomic data are available to anyone for reasonable requests.

Reference

1 Ma, L. *et al.* Human embryonic stem cell-derived GABA neurons correct locomotion deficits in quinolinic acid-lesioned mice. *Cell Stem Cell* **10**, 455-464, doi:10.1016/j.stem.2012.01.021 (2012).

2 Chen, X. *et al.* Human striatal organoids derived from pluripotent stem cells recapitulate striatal development and compartments. *Plos Biol* **20**, e3001868, doi:10.1371/journal.pbio.3001868 (2022).

3 Butler, A., Hoffman, P., Smibert, P., Papalexi, E. & Satija, R. Integrating single-cell transcriptomic data across different conditions, technologies, and species. *Nature Biotechnology* **36**, 411-+, doi:10.1038/nbt.4096 (2018).

4 Korsunsky, I. *et al.* Fast, sensitive and accurate integration of single-cell data with Harmony. *Nature Methods* **16**, 1289-+, doi:10.1038/s41592-019-0619-0 (2019).

5 Zhou, Y. Y. *et al.* Metascape provides a biologist-oriented resource for the analysis of systems-level datasets. *Nat Commun* **10**, doi:ARTN 1523 10.1038/s41467-019-09234-6 (2019).

6 van de Sande, B. *et al.* A scalable SCENIC workflow for single-cell gene regulatory network analysis. *Nature Protocols* **15**, 2247-2276, doi:10.1038/s41596-020-0336-2 (2020).